DTU Physics
Department of Physics

TiO_2 protected III-V Multi-junction Solar Cell for Photoelectrochemical Water-splitting :towards a practical solar hydrogen production

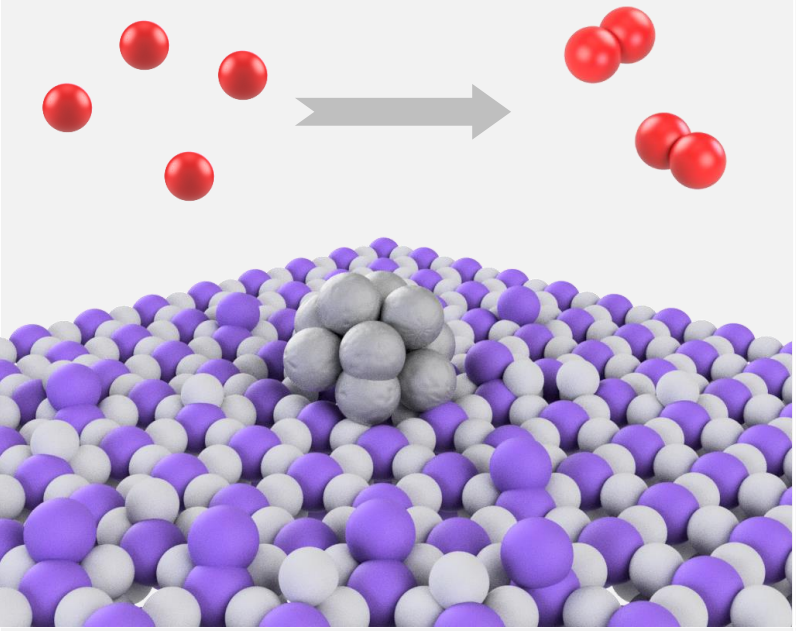

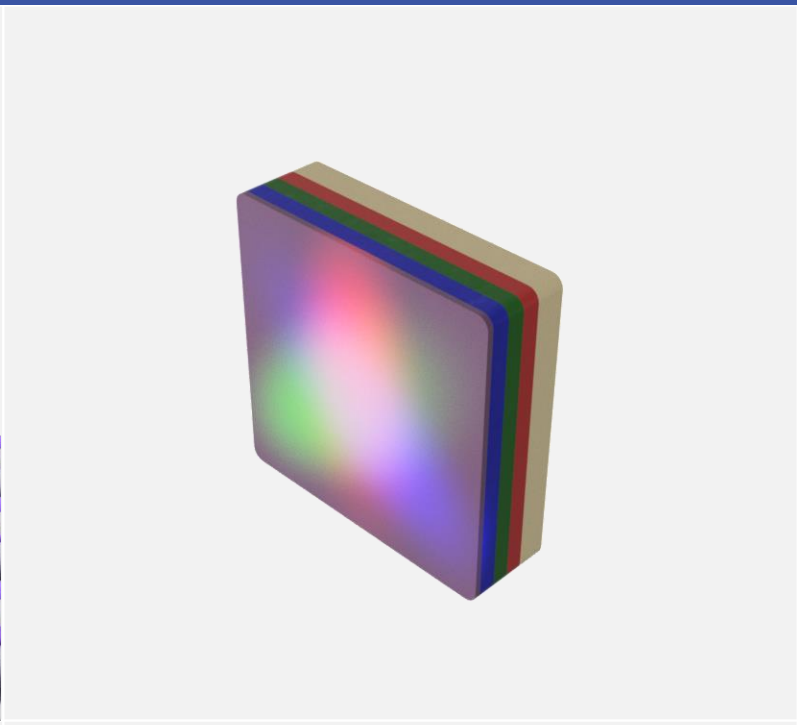

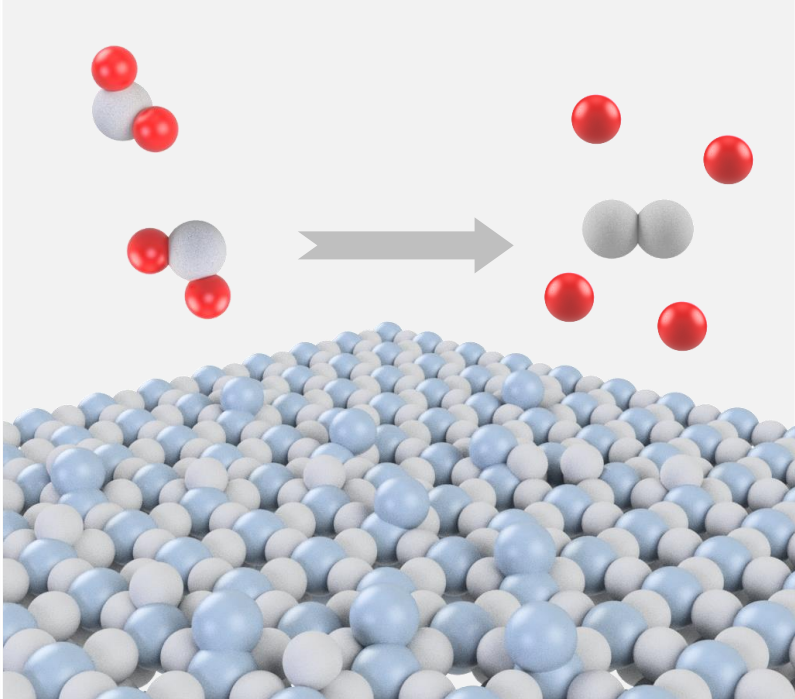

Ph.D. Thesis

Choongman Moon
November 2020

TiO_2 protected III-V Multi-junction Solar Cell for Photoelectrochemical Water-splitting

:towards a practical solar hydrogen production

Choongman Moon

Supervisor: Prof. Ib Chorkendorff
Co-supervisor: Assoc. Prof. Jakob Kibsgaard

Section for Surface Physics and Catalysis (Surfcat)
Department of Physics
Technical University of Denmark

November, 2020

TiO_2 protected III-V Multi-junction Solar Cell for Photoelectrochemical Water-splitting
:towards a practical solar hydrogen production

Ph.D. Thesis
November, 2020

Cover photo: The structure and surfaces of the wireless PEC device based on the triple-junction solar cell investigated in this study. Color codings for atoms are Red: hydrogen, White: oxygen, Purple: titanium, Grey: platinum, Light blue: iridium.

Department of Physics, Fysikvej, Building 311, 2800 Kgs. Lyngby

Preface

The work for this thesis was carried out at the Technical University of Denmark, Department of Physics, Section of Surface Physics and Catalysis (SurfCat) in the period between August 2017 and November 2020. This project at SurfCat was funded by the Villum Foundation V-SUSTAIN grant 9455 to the Villum Center for the Science of Sustainable Fuels and Chemicals.

This work has been carried out under the supervisions from Prof. Ib Chorkendorff, Prof. Peter C. K. Vesborg, Assoc. Prof. Brian Seger and Assoc. Prof. Jakob Kibsgaard, and I would like to express my deepest gratitude for giving me the opportunity to work on this project and all guidances.

I also greatly appreciate Prof. Emeritus Ole Hansen from DTU Nanolab for his many great comments and helping my first quantum efficiency measurement. The measurement managed to enlighten a lost Ph.D. student about the mysterious problem in his experiment and made everything in this thesis possible.

During my Ph.D. study, I received a lot of help from all the great people at Surfcat. I would like to thank Dowon, Shiyu and Claudie for teaching me experimental (Photo-)electrochemistry. I am also very thankful to Scott for instructing me how to use EC-MS and leading RuO_2 project. I also wish to thank Hoà and Andrea for giving useful tips and helps in and outside of the cleanroom. I appreciate Tomas Youngman for great discussions and helping Danish translation many times. Peder and Dan from workshop should be acknowledged for making the compression cell which required a series of revision. I am also grateful to Ya-Rong, Jens-Peter and Degenhart for proof-reading and improving this thesis. Thanksfully, I owe cups of coffee to my office-mate Mattia.

Last but not least, I appreciate my families for their continuous support. Especially, I thank my wife for making my life sustainable, Danu for making me smile.

Choongman Moon

November 2020

Abstract

Despite a growing international awareness of environmental problems from carbon-rich energy carriers, the rising trend in global fossil fuel consumption has increased consistently since its inception. In an effort to reverse the situation, technological advances have been made to implement carbon-free energy carriers. One of the most promising candidates for the future energy carrier is hydrogen, and vibrant research on replacing fossil fuels with hydrogen is ongoing. However, the most cost-effective process to produce (in other words, convert energy into) hydrogen is steam methane reforming and gasification, which are already releasing more than 2 % of global CO_2 emission to meet industrial uses of hydrogen. Therefore, extended use of hydrogen as an energy carrier would not be possible unless an emission-free way for producing hydrogen is developed.

Water electrolysis would be an attractive way to produce hydrogen without emission, especially when the electricity is supplied from renewable energy sources. In this regard, solar hydrogen production by combining a solar cell and water electrolyzer has been under investigation. A technically viable way to combine them at this moment would be electrically wiring a separate solar cell and water electrolyzer. Another interesting but immature approach is photoelectrochemical (PEC) water splitting, which is immersing a solar cell into an electrolyte without any wiring to derive the same electrochemical reaction. Because PEC carries out the reaction directly over a large solar cell surface with a low current density, it can reduce efficiency losses from activation energy and ohmic drop. Furthermore, a monolithic device structure can save the system cost.

However, PEC water splitting faces critical challenges to be employed for practical hydrogen production. Because semiconductors are usually unstable in an electrolyte, PEC devices cannot operate sufficiently long time until it finds economic feasibility. In addition, the optical properties of PEC devices are not optimized yet, and it results in a lower activity compared to a dry solar cell.

This thesis focuses on the major bottlenecks of PEC water splitting and it, I believe, has taken a small but important new step toward making it feasible for hydrogen production. The optical properties of the PEC devices depending on its structure are systematically investigated and suggests a way forward to minimize optical losses. Furthermore, the PEC devices in this study reach record-high stability by improving its protection layer.

Resume

På trods af en voksende international bevidsthed om miljøproblemer fra kulstofrige energibærere er den stigende tendens i det globale fossile brændstofforbrug steget konsekvent siden dens begyndelse. I et forsøg på at vende situationen er der gjort teknologiske fremskridt med at implementere kulstoffrie energibærere. En af de mest lovende af disse kandidater er brint, og forskning inden for erstatning af fossile brændstoffer med brint er fortsat i gang. Den mest omkostningseffektive proces til at producere brint er imidlertid dampreformering og forgasning, som allerede frigiver mere end 2% af den globale CO2-emission for at imødekomme industriel anvendelse af brint. Derfor vil udvidet anvendelse af brint som energibærer ikke være mulig, medmindre der udvikles en emissionsfri måde at producere brinten på.

Vandelektrolyse ville være en attraktiv måde at producere brint uden CO2 emission, især når elektriciteten leveres fra vedvarende energikilder. I denne henseende er brintproduktion ved brug af fotoelektrolyse, hvorved en solcelle og en elektrolysecelle kombineres, blevet undersøgt. En mulig måde at kombinere dem på er ved direkte elektrisk kontakt af en separat solcelle- og elektrolysecelle. En anden interessant men umoden tilgang er fotoelektrokemisk (PEC) vandsplitning, hvorved en solcelle nedsænkes i en elektrolyt uden ledninger til at udføre den samme elektrokemiske reaktion. Da PEC udfører reaktionen direkte over en stor solcelleoverflade med lav strømtæthed, kan den reducere effektivitetstab forårsaget af aktiveringsenergien og ohmske tab. Desuden kan en monolitisk enhedsstruktur reducere systemomkostningerne.

Imidlertid står PEC-vandsplitning over for kritiske udfordringer, hvis det skal kunne anvendes til praktisk brintproduktion. Fordi halvledere normalt er ustabile i en elektrolyt, kan PEC-enheder ikke fungere i tilstrækkelig lang tid, før de finder økonomisk gennemførlighed. Derudover er de optiske egenskaber for PEC-enheder endnu ikke optimeret, og det resulterer i en lavere aktivitet sammenlignet med en tør solcelle.

Denne afhandling fokuserer på de store flaskehalse ved PEC vandsplitning og har taget et lille, men vigtigt nyt skridt i retning af at gøre det muligt for brintproduktion. De optiske egenskaber for PEC-enheder afhængigt af dets struktur undersøges systematisk og antyder en vej fremad for at minimere optiske tab. Desuden når PEC-enhederne i denne undersøgelse rekordhøj stabilitet ved at forbedre dets beskyttelseslag.

List of publications

Paper I

Wireless photoelectrochemical water splitting using triple junction solar cell protected by TiO_2

Choongman Moon, Brian Seger, Peter C. K. Vesborg, Ole Hansen and Ib Chorkendorff

Cell Reports Physical Science, accepted

Paper II

Mechanistic and kinetic study of oxygen evolution on Ruthenium Dioxide down to 60 mV overpotential

Søren Scott*, Reshma Rao*, Choongman Moon, Jakob Ejler Sørensen, Jakob Kibsgaard, Yang Shao-Horn and Ib Chorkendorff

In preparation

*These authors contributed equally

Contents

CHAPTER 1

Introduction: Hydrogen production and consumption in the future

This thesis investigates a photoelectrochemical(PEC) water-splitting device in a simple and monolithic architecture as a potential pathway for ”green” hydrogen production. The motivation of this study is that, in an effort to reduce greenhouse gas emission, demands on hydrogen would increase as a clean energy carrier because hydrogen does not release any greenhouse gas during its consumption. However, contrary to hydrogen consumption, the current hydrogen production technology heavily relies on fossil fuels and releases a significant amount of greenhouse gas. The heavy reliance on fossil fuel would limit the extended use of hydrogen and greenhouse gas reduction. Therefore, there is an urgent need for novel technology for sustainable hydrogen production. One way to produce hydrogen without greenhouse gas emission is to carry out electrochemical water-splitting using energy supplied from photovoltaics. This Ph.D. project carried out studies on oxygen evolution catalysts for water-splitting reaction and the PEC device integrating the water-splitting catalysts and photovoltaics. This thesis mainly presents the later subject to cover the broader context in solar hydrogen production.

This chapter will start by presenting demands on hydrogen in the future. There are emerging technologies that could replace fossil fuels with hydrogen as a clean energy carrier. These emerging technologies will create new demands on hydrogen and accelerate hydrogen consumption. Besides, there is already a significant amount of existing demands on hydrogen from industries. This chapter will also introduce the current hydrogen production technologies and their advantages and disadvantages. While most hydrogen is produced from fossil fuels, electrochemical water splitting could be a new way to produce hydrogen without emission. Lastly, the opportunities and challenges in solar hydrogen production will be discussed in this context.

1.1 Hydrogen as a clean energy carrier

The primary agenda in the Paris agreement and following discussions is reducing the global greenhouse gas emissions from 196 countries by stocktaking emission, raising

funds and introducing the carbon market.[1] Those strong regulations on greenhouse gas draw massive attention to the transition to the carbon-neutral energy landscape. Specific action plans on how to realize the carbon-neutral society should have a very close connection with how much CO_2 is released from each sector in our society. Figure 1.1 shows the global emission of carbon dioxide by sector over time.[2] While the global carbon dioxide emission is increasing, a significant portion of the emission comes from electricity & heating (41 %) and transportation (24 %). Therefore, reducing the amount of fossil fuel consumption in those sectors would be the most crucial part of the plan, and hydrogen-relevant technologies could find opportunities in these sectors.

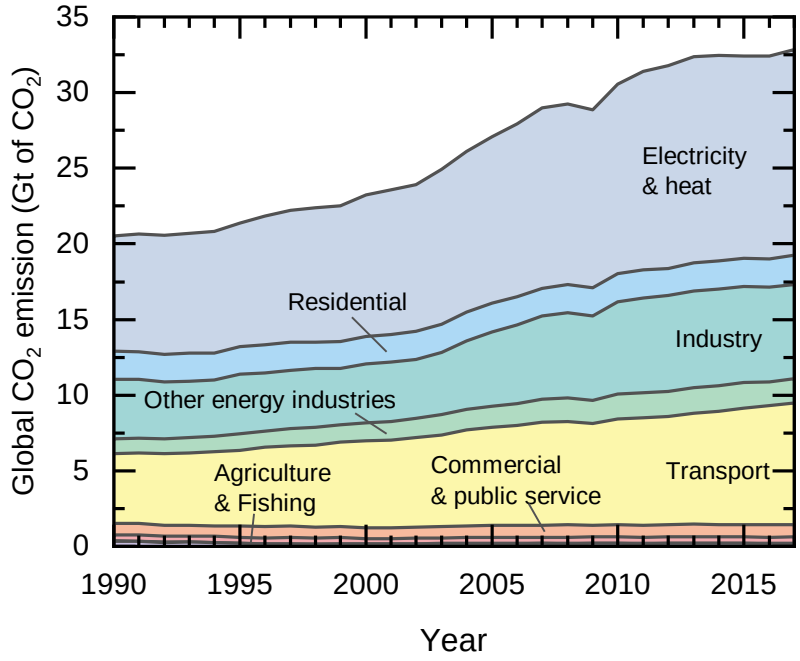

Figure 1.1: Carbon dioxide emission by sector. The image is reproduced from the IEA report (2019)[2]

Looking further into the electricity, they take a large portion of carbon dioxide emission because they live off coal-fired or gas-fired power plants (Figure 1.2A)[3] Because of their cost-efficiency compared to other power plants, the fossil fuel consumption for electricity generation has been increasing over time (2.9 % every year since 1990). There have been substitutes for fossil fuels such as nuclear energy, but it has been a controversial issue because of its safety and long-term cost-benefit. Hydro-power also can generate electricity without fossil fuels, but it also has a limitation because of its environmental effect and difficulties in finding a suitable location. Electricity generation from other renewable resources such as solar power or wind power could replace fossil fuels by harvesting energy from the sunlight or wind. As renewable resources are finding economic feasibility recently, these are proliferating and take a larger portion in the electricity generation, however, they could cause problems from its intermittent nature, which will be discussed

later.

Furthermore, the transportation sector is dominantly fueled by petroleum, which releases a significant amount of CO_2 in the air (Figure 1.2B)[4] because petroleum has high energy density and reasonable price. However, the composition of energy sources in the transportation sector needs to be changed to cope with the greenhouse gas emission issue. Overall, the direction of technological developments should be replacing fossil fuels with low-carbon energy sources or carriers in every aspect of the current energy landscape.

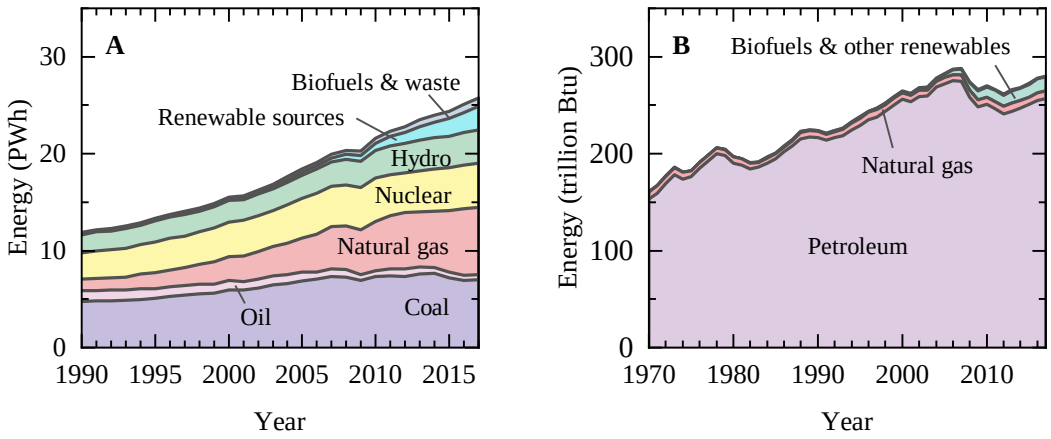

Figure 1.2: Electricity generation and energy consumption transportation by source. The images are reproduced from the reports [3, 4]

As a low-carbon energy carrier, hydrogen is considered to be an ideal material because it is made up of only two hydrogen atoms without carbon atoms. Therefore, hydrogen will release water as a by-product during its consumption instead of greenhouse gas. Furthermore, the high specific energy density (142 MJ/kg)[5] of hydrogen also makes it attractive as an energy carrier. In this regard, technological advancements for using hydrogen have been made over the decades. The chemical energy stored in hydrogen can be converted into a useful form of energy by oxidizing the hydrogen. A fuel cell is an efficient way for hydrogen oxidation reaction, which is a stack of materials that can combine hydrogen and oxygen to produce electricity and water. Other ways for hydrogen oxidation, such as hydrogen boiler or hydrogen gas turbine, are also possible depending on an application. It is expected that those techniques are applicable to the following fields: 1) Transport, 2) Building heating and 3) Long-term energy storage.[6] In the following sections, technological attempts to replace fossil fuels with hydrogen in each field will be introduced.

1.1.1 Transport

As shown in Figure 1.2B, fossil fuel is taking over the absolute portion of the energy sources in the transportation sector. Therefore, replacing fossil fuels in this sector with hydrogen would reduce a significant amount of greenhouse gas emissions. In this regard,

major automobile companies and governments are trying to commercialize fuel cell electric vehicles (FC-EV), which is fueled by hydrogen and releases only water during operation. Although there is an on-going debate on the economic benefit of FC-EV compared to other types of low-emission vehicles such as the electric vehicle, a general consensus is that, based on the current level of technology, FC-EV is more competitive for heavy-duty vehicles running over a long distance (> 400 km) because of the high specific energy density of hydrogen compared to batteries.[6] Depending on technological development in the future, FC-EV could become a more attractive option than now. Governments are suggesting ambitious targets for FC-EV and hydrogen recharging stations (HRS), as shown in Figure 1.3.[7, 8] As FC-EV and HRS popularize, it will provoke significant demand for hydrogen.

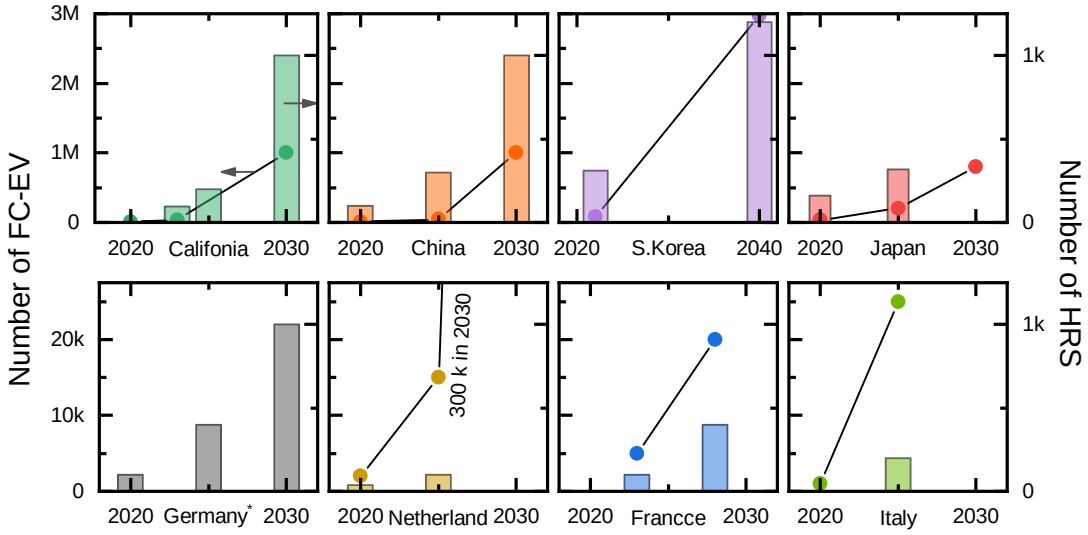

* German government does not suggest a specific goal for # of FC-EV

Figure 1.3: The future targets for deployment of FC-EV and RHS declared from selected governments.[7, 8]

The advantage of hydrogen for heavy-duty vehicles becomes even more apparent when it comes to aviation or shipping, which are responsible for 2 $\sim$ 3 % of global carbon dioxide emission, respectively.[6] Excluding fossil fuels, either pure hydrogen itself or hydrogen-based fuels such as ammonia (produced from hydrogen and nitrogen) and synthetic hydrocarbons (produced from carbon dioxide and hydrogen) would be the only available options to fuel airplane or vessel due to their high energy density.[6] Please note that synthetic hydrocarbons are still carbon-neutral when it is produced from carbon dioxide captured from the air. These fuels can be co-fired with the conventional fossil fuels in an internal combustion engine in the near future or consumed in the fuel cell.[6]

According to an estimation in the report[9], the global demand for passengers and freight transportation will triple between 2015 and 2050, which implies that there will be a significant challenge in reducing greenhouse gas emissions in this sector. As discussed in this subsection, hydrogen is the only attractive (or the only in the case of aviation or

shipping) replacement for fossil fuels. Therefore, significant demand for hydrogen would be created in the transportation sector.

1.1.2 Building heating

The energy consumption for heating buildings accounts for a large portion of carbon dioxide emission derived from fossil fuel. Therefore several technologies, including fuel cells or hydrogen boilers, are under investigation for replacing fossil fuel in this sector. The most technically feasible approach in the near future is blending hydrogen with natural gas and supply through existing pipelines. France and Netherlands launched pioneering projects and showed that blending 20 $\sim$ 30 % of hydrogen to the natural gas did not cause a serious problem in the existing heat supply system.[10] Therefore, communities with an infrastructure to supply natural gas for heating has an opportunity for a significant reduction in greenhouse gas emission.[11] Figure 1.4 shows energy sources used for heating in selected countries.[3] The countries with more extensive infrastructure for supplying the natural gas have a bigger chance to reduce emission by blending or replacing the natural gas with hydrogen.[11] Depending on the needs for reducing CO_2 emission, hydrogen price and technological development, a larger portion of hydrogen could be deployed to replace the natural gas in the future, and it would raise a massive demand for hydrogen.

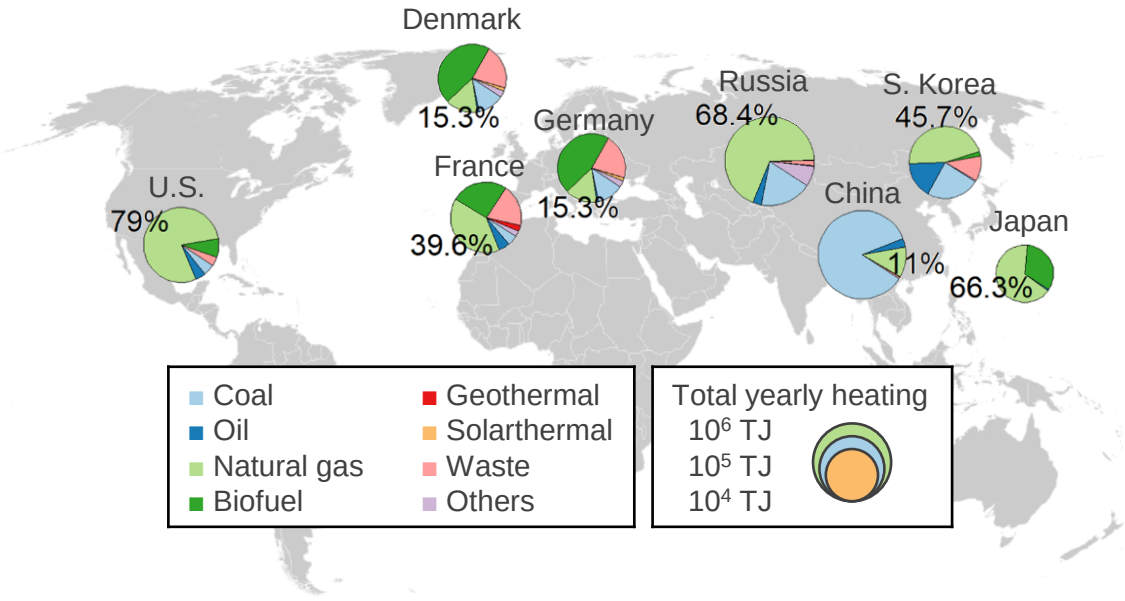

Figure 1.4: Heat generation by source from selected countries in 2017.[3] The numbers indicate the portion of natural gas in heating. The countries with a higher portion of natural gas would be able to supply heat from hydrogen.

1.1.3 Long-term energy storage

With the growth of renewable energy sources, an efficient and stable energy storage solution (ESS) will be an essential part of the future energy landscape. The power generation by solar and wind energy sources has been grown 19 % every year since 2009, and it accounts for around 10 % of total power generation now.[3] The higher portion of the solar

and wind power in energy production will pose a problem caused by their intermittent nature. Because energy production by renewable energy resources is affected by weather, it is highly possible that there would be a daily or seasonal variance in the power generation. For efficient usage of energy, the surplus amount of electricity should be stored in ESS for later use. Among several different types of ESS, the most dominant one is pumped hydropower storage (PHS) nowadays.[12] However, its huge water reservoir demands specific geological requirements and devastates the surrounding environment and ecological system. Therefore, alternative technologies, including compressed hydrogen for ESS, is under investigation. Compared to other technologies, the compressed hydrogen or hydrogen-based fuel (ammonia) has the lowest cost when energy is stored more than 100 hours before discharging, as shown in Figure 1.5A.[6] This is because the compressed hydrogen storage in a tank or salt cavern has a much longer lifetime and lower capital cost at a larger scale. Therefore, the compressed hydrogen is generally perceived as ESS for storing 1 GW-scale energy over seasons (Figure 1.5B)[11], and it might be the most economical option for ESS in the commercial or industrial sector in the future.[13] Therefore, storing the overproduced electrical energy in the form of hydrogen would be a promising way to cope with the seasonal variance in renewable energy production.

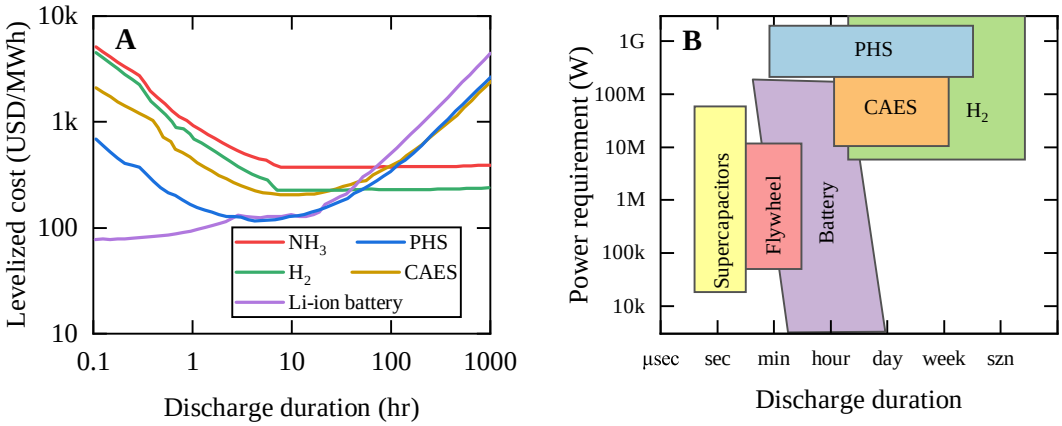

Figure 1.5: (A) Levelized cost of ESS technologies depending on discharging duration. It is assumed that hydrogen is stored in salt cavern and ammonia is stored in a tank. The electricity cost for operation is assumed to be 50 USD/MWh. PHS: pumped hydropower storage, CAES: compressed air energy storage.[6] (B) Comparison of various ESS technologies in terms of discharge duration and power.[11] The images are reproduced from the reports.[6, 11]

1.1.4 Estimated demand on hydrogen in the future

The previous sections are introducing the emerging technologies on hydrogen, which could be arisen in the future by the need for reducing greenhouse gas emissions. In addition, there are also existing technologies on hydrogen for the oil refinery, fertilizer and other chemical production, which have been increasing annually.[6] Because the value chain for the technologies is complicated, it would be very difficult to forecast the future of hydrogen. Nevertheless, there are several analyses on how much hydrogen would be

consumed by the emerging technologies for reducing greenhouse gas emission, which is presented in Figure 1.6.[14–16] The data points show 8 different scenarios from 3 independent reports on the hydrogen consumption by emerging technologies, and the solid black line and the grey area shows a simple averaging of the data points and the standard deviation. Even though the large standard deviation implies that there is considerable uncertainty in the prediction, the average of the scenarios shows that hydrogen consumption for the new emerging technologies increases $\sim$ 23 % annually, which is extremely fast, to reach 30 $\pm$ 26 Mt/yr in 2040. In the case of existing technologies, 70 Mt/yr of existing demand for pure hydrogen comes from oil refinery and ammonia production (the horizontal line in Figure 1.6), which has been increased $\sim$ 1.9 % over the last two decades[6]. Thus, it is expected that the demands on hydrogen would increase in the future.

However, the new emerging technologies are pursued in efforts to reduce greenhouse gas emissions. Thus hydrogen involved in these technologies should be produced with a low level of greenhouse gas emission. When considering that hydrogen production for the current demand already accounts for more than 2 % of global CO_2 emission, such a rapid increase in hydrogen demand expected from the reports may not be possible unless an emission-free way to produce hydrogen is developed. The next section will review the current hydrogen production technologies and discuss their environmental effect.

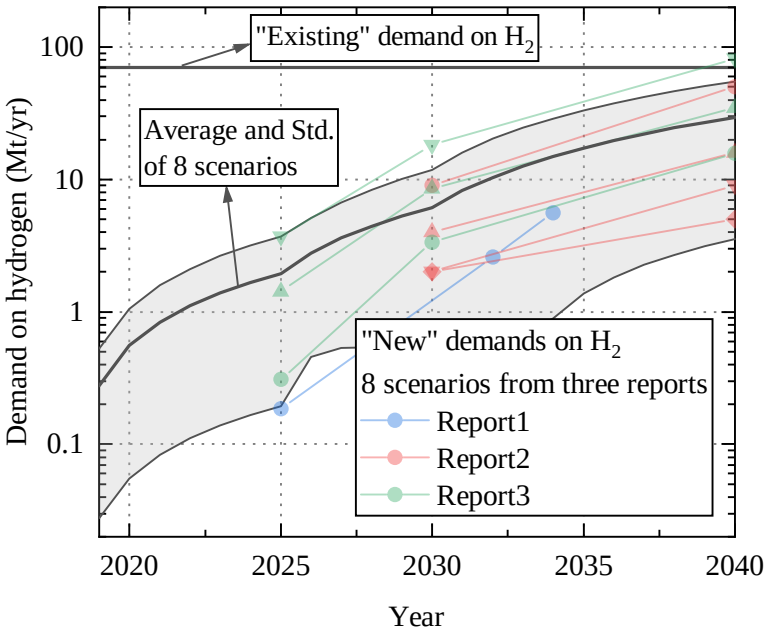

Figure 1.6: The 8 different scenarios from 3 reports estimating the demand for hydrogen in the future.[6, 14–16] The solid line and the grey area represent the simple average and standard deviation between the scenarios. The solid horizontal line shows the current demand on hydrogen (in 2018).

1.2 The current hydrogen production technologies

As discussed in the previous sections, the demand for hydrogen as an energy carrier is expected to increase[6, 14–16], thus hydrogen production supporting the increasing demand would be necessary for the future. However, the current hydrogen production is not free from greenhouse gas emissions yet. Figure 1.7 shows the current hydrogen production (including both pure hydrogen and mixed gas) by sources.[6] Hydrogen production plants dedicated to producing hydrogen (Steam reforming and gasification) rely on fossil fuels. Some of the oil refinery and chemical industries produce hydrogen as a by-product which is also based on fossil fuels. This section will introduce these technologies for hydrogen production and discuss renewable pathways for producing emission-free hydrogen.

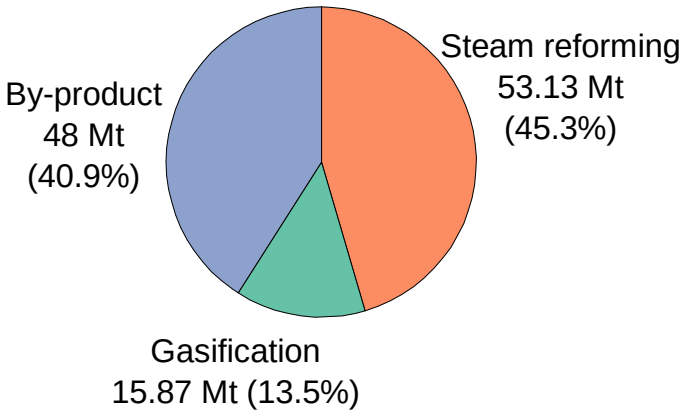

Figure 1.7: Hydrogen production by sources in 2018.[6] Most hydrogen is produced from fossil fuels (58.8 %) or as by-products from the industrial process (40.9 %), and only a small amount of hydrogen (< 1 %, not shown in the figure) is produced from renewable energy sources.

1.2.1 Steam methane reforming and gasification

Liquid or gaseous form of fossil fuel can react with water molecules to produce hydrogen and carbon monoxide as shown in the following reaction.[17, 18]

$$C_nH_m + H_2O \rightarrow nCO + \left(n + \frac{1}{2}m\right) H_2 \quad (\triangle H = 206kJ/mol) \tag{1.1}$$

In this reaction, a fossil fuel with a larger hydrogen-to-carbon ratio is beneficial to reduce CO emission at the same amount of hydrogen production. Because natural gas is abundant and mostly composed of methane (88 %), which is having a high hydrogen-to-carbon ratio ($n = 1$, $m = 4$), it is mainly used for the steam reforming reaction. The reaction with methane is called steam methane reforming (SMR). The product of the SMR is a mixture of carbon monoxide and hydrogen. In order to increase the amount and purity of the hydrogen product, the carbon monoxide from SMR is further oxidized by a water-gas shift

reaction (WGSR).

$$CO + H_2O \rightarrow CO_2 + H_2 \quad (\triangle H = -41kJ/mol) \tag{1.2}$$

The SMR is a highly endothermic reaction that requires very high temperature (700 $\sim$ 1100°C)[17, 18], and WGSR is an exothermic reaction and usually operates at relatively lower temperature (200 $\sim$ 400°C)[19]. To maximize the energy efficiency of the entire processes, including both exothermic and endothermic reactions, steam reforming plants require a careful design of heat and mass transfer inside of the plant. Larger and more centralized plant designs are preferred to maximize efficiency and reduce the cost of hydrogen production. It is known that the cost is around 1 $\sim$ 2 USD.[6]

The gasification process is the reaction for converting solid-state fuels (coal or biomass) into synthesis gas, which can be also used for producing hydrogen.[20]

$$C + H_2O \rightarrow CO + H_2 \quad (\triangle H = 131kJ/mol) \tag{1.3}$$
$$C + O_2 \rightarrow CO_2 \quad (\triangle H = -394kJ/mol) \tag{1.4}$$
$$C + \frac{1}{2}O_2 \rightarrow CO \quad (\triangle H = -111kJ/mol) \tag{1.5}$$
$$CO + CO_2 \rightarrow 2CO \quad (\triangle H = 172kJ/mol) \tag{1.6}$$

The gasification reaction can be followed by WGSR, like SMR, to produce more hydrogen from carbon monoxide and water. For similar reasons, gasification plants are also large and centralized, and the cost of hydrogen production from those plants is relatively cheaper than the steam reforming plants($\sim$ 1 USD).

As shown by the reaction equations (equation 1.1$\sim$ 1.6), both SMR and gasification releases a large amount of carbon dioxide during hydrogen production. In terms of carbon dioxide emission per a tonne of hydrogen production, SMR releases 10 tCO_2/tH_2 whereas gasification releases 19 tCO_2/tH_2.[6] Total emission from SMR and gasification is around 830 $MtCO_2$/year, which corresponds to $\sim$ 2 % of global CO_2 emission in 2018.[6] To reduce the emission, SMR and gasification process can combine with carbon capture, use and storage (CCUS) at the expense of an increase in the production cost. By adding CCUS to the plants, the production cost of hydrogen from SMR and gasification increases by $\sim$ 0.5 USD.[6]

1.2.2 By-product hydrogen

Around one-third of hydrogen is produced as a by-product in a variety of industrial sectors, and a major portion of by-product hydrogen is originated from a petroleum refinery. Steam cracking is a chemical process to break down heavy hydrocarbon into high-value chemicals, often by dehydrogenation. For example, propane molecule (C_3H_8) is cracked into propylene (C_3H_6) and hydrogen. These kinds of steam cracking process produces 18 MtH_2/year of by-product hydrogen in 2018.[6] As-produced by-product hydrogen is often used on-site for other processes in chemical engineering sectors.

The iron and steel industry is also both a major by-product hydrogen producer and hydrogen consumer. Blast furnace gas is generated from a metallurgical process in a blast furnace, and it contains nitrogen, carbon dioxide, carbon monoxide and hydrogen. The amount of hydrogen contained in the blast furnace gas is 14 MtH_2/year globally[6], and most of them are directly used on-site for reducing iron ore or producing power.[6]

14 MtH_2/year of by-product hydrogen is produced from chlor-alkali process[6], which is electrolysis of brine (highly concentrated saltwater) into chlorine, sodium hydroxide and hydrogen as below[21]

$$2NaCl + 2H_2O \rightarrow Cl_2 + H_2 + 2NaOH \tag{1.7}$$

The products of this reaction are chlorine and sodium hydroxide, and these are major building blocks for a myriad of industries, including plastic, textiles, paper and cleaning.[22] This process does not produce greenhouse gas during its reaction. However, the mass production of hydrogen-based on this method would be harrowing because it has low energy efficiency by consuming 351 GJ for producing a tonne of hydrogen. Assuming hydrogen can generate 120 GJ/t, energy efficiency is only 34 %. The value of the co-products could make it find economic feasibility, but the supply chain of chlorine and sodium hydroxide makes mass-production complicated.

1.2.3 Water electrolysis

Most of the hydrogen atoms found on the earth are combined with oxygen or carbon to form water molecules or hydrocarbons, respectively. Thus, molecular hydrogen can be produced by separating the hydrogen atoms from either water or hydrocarbons. Because of the cost-efficiency, hydrogen has been mostly produced by using the hydrocarbons by the processes introduced in the previous sections (SMR or gasification), although it releases the greenhouse gas. However, hydrogen can also be produced from water, which would be one of the most abundant resources on the earth. Water molecules can be splitted into hydrogen and oxygen by the following reaction.[23]

$$2H_2O \rightarrow 2H_2 + O_2 \tag{1.8}$$

The reaction is endothermic and requires external energy, which is mainly electricity. Water electrolysis is considered the cleanest way to produce hydrogen, especially when the external energy is supplied from renewable energy sources. Besides, the only by-product of the water-splitting reaction is oxygen, which is not harmful to the environment. The cost for hydrogen production by water electrolysis is around 2 $\sim$ 3 USD/kg[24] and getting closer to SMR (1 $\sim$ 2 USD/kg). Although the current level of production accounts for less than 1 % of the global hydrogen production[6], governmental policies support the installation of MW or tens of MW scale plants every year, and it is expected to increase further in the future.[25] However, water electrolysis still relies on electricity produced from fossil fuels. A combination with renewable energy sources in a cost-efficient way would

be necessary for clean hydrogen production.

Depending on conducting ions and the external energy, there are three different types of technologies: Alkaline electrolysis cell (AEC), Proton exchange membrane (PEM) and solid oxide electrolysis cell (SOEC). The schematic diagrams are depicted in Figure 1.8.

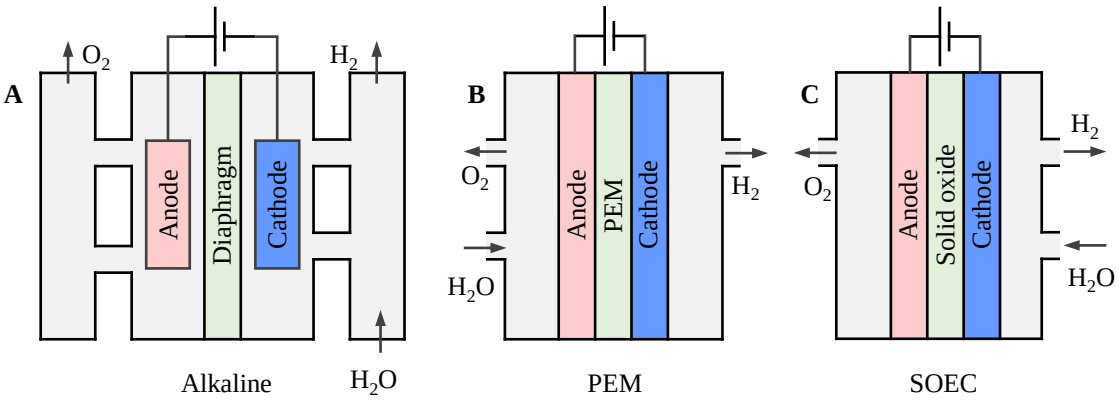

Figure 1.8: Three different types of water electrolyzers. (A) AEC, (B) PEM and (C) SOEC

AEC has long been used for many chemical processes such as chlor-alkali process.[6] Water electrolysis in AEC is also carried out using alkaline water electrolyzer in the first place and now it takes dominant portion of the current electrochemical hydrogen production.[23, 26] As shown in Figure 1.8A, cathode and anode are immersed in an alkaline electrolyte (KOH or NaOH) and separated by diaphragm to separate gaseous product from each electrode. External electrical energy is supplied to the electrodes to drive the following half-reactions:

$$2H_2O + 2e^- \rightarrow H_2 + 2OH^- \quad (cathode) \tag{1.9}$$

$$4OH^- \rightarrow O_2 + 2H_2O + 4e^- \quad (anode) \tag{1.10}$$

Water electrolysis by AEC does not require noble metal catalysts and has a relatively lower installation cost.[6, 23, 26] But the cross-over of hydrogen and oxygen products could take place, and it has large ohmic loss due to the low conductivity of OH^- ions hindering operation at a large current density. The purity of hydrogen product from AEM is around $99.5 \sim 99.9$, which is relatively lower than other methods because of the crossover between hydrogen and oxygen through the diaphragm.[23, 26, 27]

Proton exchange membrane (PEM) water electrolysis is in the early stage of commercialization by overcoming the disadvantages of alkaline water electrolysis using PEM. PEM water electrolyzer operates in an acidic environment:

$$2H^+ + 2e^- \rightarrow H_2 \quad (cathode) \tag{1.11}$$

$$2H_2O \rightarrow O_2 + 4H^+ + 4e^- \quad (anode) \tag{1.12}$$

PEM membrane transports H^+, which is having higher conductivity than OH^- and it enables the PEM water electrolyzer to operate at higher current density. Moreover, PEM has less crossover of gaseous products than the diaphragm and yield hydrogen product with more than 99.99 % purity.[23, 27] However, PEM water electrolysis requires expensive noble metals as catalysts for stable and efficient operation.

In some cases where abundant thermal energy is available at a low cost, such as high-temperature steam from nuclear power plants, it can be exploited as a useful energy source. SOEC is an emerging technology that can utilize superfluous thermal energy to assist water electrolysis. SOEC adopts zirconium oxide (ZrO_2) doped with yttrium oxide (Y_2O_3) as an electrolyte.

$$H_2O + 2e^- \rightarrow H_2 + O^{2-} \quad (cathode) \tag{1.13}$$

$$2O^{2-} \rightarrow O_2 + 4e^- \quad (anode) \tag{1.14}$$

The advantage of SOEC is that it requires less amount of electrical energy by having thermal assistance. Furthermore, the kinetics of the reaction is more favorable in high temperature that it enhances efficiency and does not require expensive noble metals. However, SOEC requires further research effort for stable operation at high temperature.

1.2.4 Solar hydrogen production

As introduced in the previous sections, the current hydrogen mostly relies on fossil fuels and it results in a significant amount of greenhouse gas emission. To avoid the emission, water electrolysis is promoted under support policies, however water electrolysis is not entirely free from emission as long as the source of electrical energy is fossil-fuels. It would be possible to say that hydrogen production is immaculate when the electrical power is supplied by renewable sources, and this would be an essential part of the carbon-neutral scenario. In this regard, there have been efforts to convert solar energy into hydrogen by combining water electrolyzer and photovoltaics. Electrically wiring separate solar cells and water electrolyzer (PV+EC) would be the most straightforward method because both photovoltaics and water electrolyzers are matured technology.[28] PV+EC is demonstrated in a laboratory-scale with 30 % of STH efficiency[29], and also demonstrated in a pilot plant scale.[30] Moreover, it is suggested that PV+EC could be improved by the PEC approach, which is immersing a solar cell into an electrolyte. In principle, immersing a solar cell could provide a sufficient photovoltage and photocurrent when the surface of the solar cell forms a proper solid-liquid junction.

1.3 The outline of the thesis

This thesis aims to fully utilize the advantage of PEC and also resolve its most critical problems. Chapter 2 will present several important concepts for understanding PEC and point out the major advantages and challenges in PEC study. In chapter 3, the experimental methods for sample preparation and characterization will be introduced. Chapter 4 will show a detailed characterization of the activity of the PEC device. The investigation

using the PEC device with two light sources will show how the protection layer affects subcells in PEC devices' performance. Chapter 5 presents the stability of PEC devices. A proper procedure for testing the stability test on PEC devices will be discussed and record-high results in the stability test will be presented. Chapter 6 will draw the main conclusion of the thesis based on the challenges addressed in Chapter 2 and discuss the future outlook.

CHAPTER 2

PEC water splitting system

PEC devices are a combination of a water electrolyzer and a solar cell into a single device. Therefore, understanding both of them is an essential part of this thesis. This chapter will elaborate on essential backgrounds on them concerning the experiments done in this thesis. This chapter will start by introducing electrocatalysts for water splitting. Afterward, the photocurrent generation by solar cells will be introduced.

2.1 Catalysts for water splitting

Under the ambient temperature and pressure, enthalpy required for water-splitting reaction is 286 kJ/mol, and 163.09 kJ/mol/K of entropy change assists the reaction. Therefore, Gibbs free energy required for driving water splitting reaction is:

$$\begin{aligned} \triangle G &= \triangle H - T\triangle S \\ &= 286kJ/mol - 163J/mol/K \times 298K \\ &= 237kJ/mol \end{aligned} \tag{2.1}$$

Here, G, H, T and S represents Gibbs free energy, enthalpy, temperature and entropy, respectively. Because two electrons are participating in the reaction of one water molecule, electrical potential required for the electrochemical reaction is:

$$\begin{aligned} \triangle V_{th} &= \frac{\triangle G}{2 \times F} \\ &= \frac{237kJ/mol}{2 \times 96485C/mol} \\ &= 1.23V \end{aligned} \tag{2.2}$$

Here, F is the Faraday constant. The equation 2.2 shows that at least 1.23 V of potential difference has to be applied on a cathode and an anode. However, actual water splitting needs a higher voltage due to ohmic loss and the activation energy of the reaction. The excess amount voltage required to drive the reaction is called ”overpotential”. The energy spent on the overpotential is dissipated as heat and usually cannot be recovered. Therefore, the ohmic loss and activation energy have to be decreased for achieving higher

energy efficiency. The ohmic loss can be alleviated by reducing the total resistance in a system with a careful design. The activation energy of the reaction depends on the intermediate steps in the reaction taking place on the surface of the electrode. The adsorption energy of the intermediate steps on the surface should be neither too strong nor too weak to minimize the activation energy. A catalyst with the proper adsorption energy deposited on the surface can reduce the loss from the activation energy, and the choice of catalyst is influenced by the type of reaction and pH of the electrolyte. In this study, water-splitting reaction occurs in acidic electrolytes, because good gas separation membranes are available and ionic conductivity is high in acid. The water splitting is made up of two half-cell reactions: 1) Hydrogen evolution reaction (HER) taking place on the cathode, whereas 2) Oxygen evolution reaction (OER) taking place on the anode. HER is a less complicated two-electron process (equation 1.11) while OER is more complicated 4 electron process (equation 1.12), and it makes HER is relatively easier. In the following sections, further details about HER and OER catalysts will be discussed.

2.1.1 Hydrogen evolution catalysts

A series of materials have been investigated for HER catalyst, and the activation energy required for HER is well understood by the previous studies based on Sabatier's principle.[31–33] A major parameter affecting the activation energy turns out to be the adsorption energy between the surface of catalyst and reaction intermediates, which is a proton adsorbed on the surface (H*) in the case of HER. The adsorption energy of protons on the surface should not be too weak to adsorb protons and should not be too strong to promote the reaction following after the adsorption. Figure 2.1A shows a computational study on catalytic activity depending on the adsorption energy of proton on the surface of different materials.[31] It shows that platinum has almost ideal adsorption energy for HER, and it makes even small loading of platinum catalyst would be enough for a practical application. Therefore, this study uses platinum as an HER catalyst.

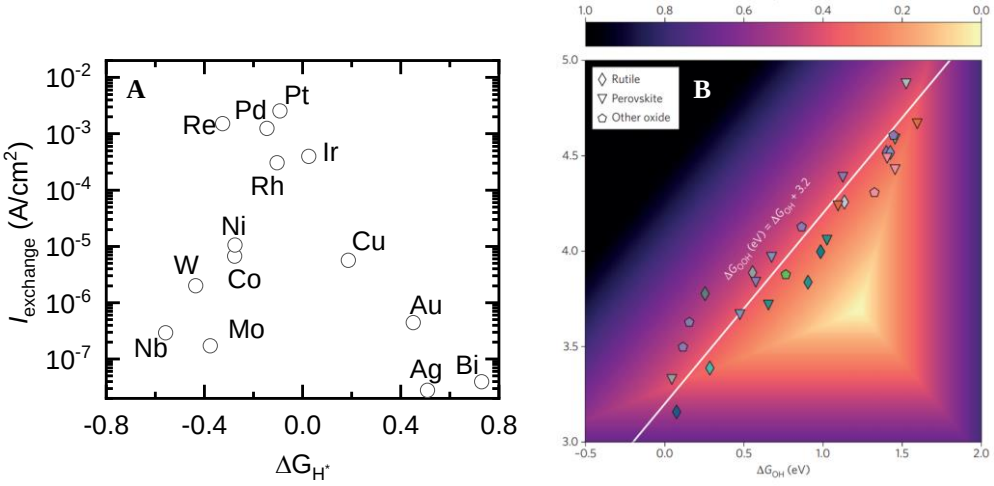

Figure 2.1: Catalytic activities of (A) HER and (B) OER depending on the adsorption energies of reaction intermediates. Figure (A) is reproduced from [31], and (B) is taken from [33]

2.1.2 Oxygen evolution catalysts

OER is rather complicated than HER because three intermediates (OH^*, O^* and OOH^*) are appearing during the reaction. To minimize the activation energy for OER, the adsorption energy of these intermediate species should not be too weak or too strong. The adsorption energies of the intermediates on the surface of many different catalysts have been investigated[31, 32], and it is found that there is a universal scaling relation between the adsorption energies as shown in Figure 2.1B. The difference between the adsorption energy of OH and OOH is always around $\sim$ 3.2 eV regardless of materials. (The white line in Figure 2.1B) Because it is difficult to control the adsorption energies of the intermediate species independently, there is a significant challenge in developing an ideal OER catalyst. Furthermore, in the case of the acidic environment, such as the PEM water electrolyzer, most materials are unstable in the anodic potential, narrowing the choice of materials. Due to the difficulties in finding an ideal OER catalyst, there is a significant efficiency loss in the OER side in a water-splitting reaction. While iridium oxide and ruthenium oxides are well known for having a relatively good OER performance in terms of activity and stability, iridium oxide is chosen as an OER catalyst in this project.

2.1.3 Remarks on the study on RuO_2 for OER catalyst in this project:Importance of collecting products

This Ph.D. project also encompasses the investigation on RuO_2 as an OER catalyst. The experiments are carried out with Søren Scott, Reshma Rao and Jakob Ejler. Although there are many important significances in the RuO_2 study, this section will remark one of the key messages, which is also important in this thesis.

OER catalysts' performance is often measured by collecting the electrical charges participating in the reaction at an electrical potential. However, the electrical charges could also be collected from a pseudo-capacitance or dissolution of materials. The uncertainty in the OER activity measurement becomes even more serious when characterizing the OER activity of ruthenium oxide especially at a low overpotential because it has very high pseudo-capacitance and is not stable in acidic electrolyte. Scott clarifies the uncertainty by collecting both electrical charge and oxygen product from an amorphous ruthenium oxide film and showing their difference.[34]. The electrochemical mass-spectrometer (EC-MS) used for the experiment is depicted in Figure 2.2A. The EC-MS enables the in-situ characterization of gaseous products with high sensitivity (pmol/s) and fast response time (< 1 sec). Figure 2.2B shows the discrepancy between the charge collection and the gas collection at a low overpotential range. As the electrical potential increases to 1.37 V vs RHE (2525 s), the current density also increases, however, oxygen is not detected because the charges are mostly originated from charging the pseudo-capacitance of the film.

The gas collection by EC-MS is further improved by using the isotope-labeled electrolyte. By using the isotope-labeled electrolyte, the oxygen molecules originated from the water-splitting reaction and lattice oxygen can be distinguished. The water molecules in the isotope-labeled electrolyte are composed of 97 % $H_2^{18}O$, and the oxygen product

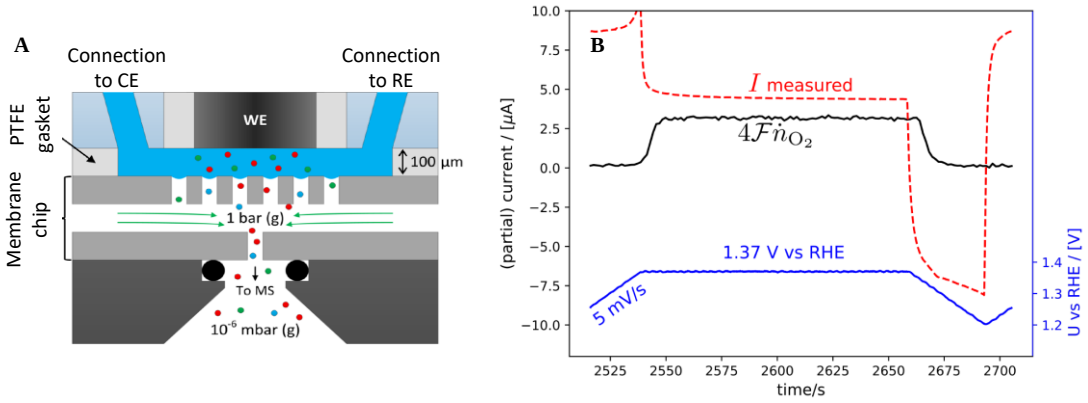

Figure 2.2: OER activity of sputtered amorphous RuO_2 film characterized by collecting both electrical charge and gaseous products. (A) shows a schematic diagram of EC-MS used for the characterization, and (B) shows the discrepancy between the charge collection and gas collection. The images are taken from [34]

produced from the electrolyte should provide a commensurate amount of $^{36}O_2$ and $^{34}O_2$. In this way, the OER activity of RuO_2 catalyst at a low overpotential is very precisely characterized. One of the most interesting results is from highly porous Ru foams, which is having a huge surface area ($\sim$ 2000 of roughness factor), as shown in Figure 2.3A. Because their large surface area provides a larger amount of oxygen products compared to a flat thin film, the activity of the Ru foams can be characterized with higher accuracy. The Ru foam is prepared by electrochemical deposition of Ru with 10 mM of $RuCl_3$ in 0.1 M $HClO_4$. Ru is deposited at a very low deposition potential, -6 V vs RHE, and it results in a vigorous hydrogen evolution making bubbles on its surface. When the OER activity of the Ru foam is measured in EC-MS with the isotope-labeled electrolyte, the oxygen products from the water-splitting reaction is detected at 1.29 V vs RHE, which is only 60 mV above the thermodynamic water splitting potential as shown in Figure 2.3B. The OER

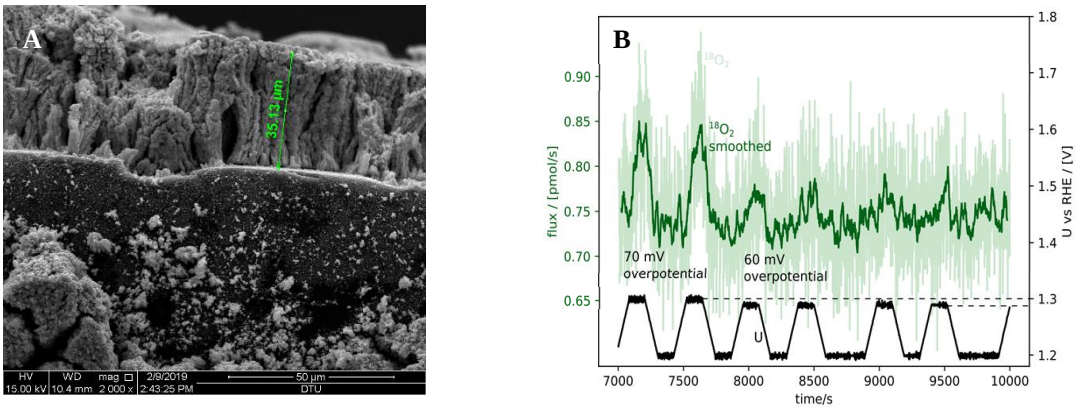

Figure 2.3: Detection of oxygen evolution with 60 mV of overpotential. (A) The SEM image of Ru foam used for the measurement. (B) $^{36}O_2$ evolved from the isotope-labeled electrolyte is detected at 1.29 V vs RHE. The images are taken from [34]

study delivers a message also important for PEC study. Many PEC studies are collecting charges for evaluating the performance of their PEC devices, however, the characterization by collecting only electrical charges could potentially lead to over-estimation of the device performance just as shown by the RuO_2 study.

2.2 Solar cells for PEC

This section will elaborate on photovoltaics used for preparing PEC devices. It will start by briefly introducing photo-excited charge carrier generation and separation by the p-n junction or solid-liquid junction. The efficiency of solar cells and its improvement by the tandem approach will also be introduced because it is necessary to drive the water-splitting reaction without any external energy input.

2.2.1 Single junction solar cell

When light hits a semiconductor material with a bandgap, photons whose energy is larger than the bandgap can excite electrons in the valence band to a conduction band and creates a pair of electron and hole. The high energy electron in the conduction band is relaxed to the energy level just above the bandgap, and the high energy hole in the valence band is relaxed to the energy level just below the bandgap immediately ($\sim$ 1 ps).[35] The energy lost during the relaxation is thermally dissipated. Unless the electron and hole separated by the band gap are separated, they will recombine and emit photoluminescence soon after the excitation ($\sim$ 1 ns).[35] To avoid the recombination of the charge carriers and make them participate in an electrochemical reaction before they recombine, a built-in electric field could be applied to separate the charge carriers having opposite sign of charge. PEC device has two different way to apply the electric field. The first way is using a buried p-n junction like a conventional solar cell (Figure 2.4A and B). The second way is using a solid/liquid junction (SLJ), which resembles metal-semiconductor contacts but uniquely possible in PEC. Depending on the energy level of redox couple in electrolyte and electron affinity of semiconductor (Schottky-Mott rule), energy barrier separating electron and hole could be formed in the solid/liquid junction (Figure 2.4C and D). A PEC device with electrons approaching an electrolyte makes a reducing reaction and denoted as photocathode (Figure 2.4A and C), whereas a device with holes approaching an electrolyte makes an oxidizing reaction and called as photoanode (Figure 2.4B and D).

The energy output from the solar cell can be found by multiplying the photocurrent and photovoltage generated by the solar cell. Photovoltage is determined mainly by the bandgap of the semiconductor. As explained in the previous charge separation mechanism, photons with energy larger than the band gap will thermally dissipate the excess amount of energy and generate electron-hole pair, and their energy difference is determined by the bandgap. Therefore, large bandgap semiconductors provide higher photovoltage. However, the large bandgap limits the current density because photons with energy lower than the bandgap cannot excite the electron-hole pairs. Therefore, a solar cell made up of a single semiconductor junction has a trade-off between photovoltage and photocurrent depending on the size of a bandgap. The theoretical maximum efficiency

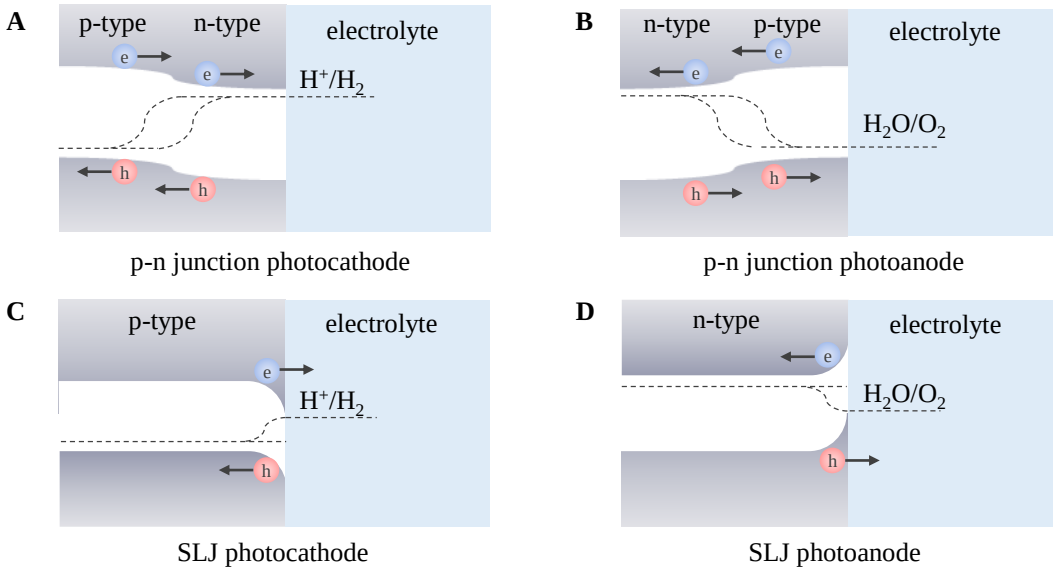

Figure 2.4: Charce carrier separation in PEC devices.

of solar cells considering the energy loss by the thermal dissipation, unabsorbed photon and other minor effects (recombination and blackbody radiation) is known as Shockley–Queisser (SQ) limit.[36, 37] The solid line in Figure 2.5 shows the SQ limit of solar cell and the data points shows the efficiency of various solar cells, which are lying below SQ limit.

Furthermore, the solar cell used for PEC should be able to supply a sufficient photovoltage to drive an electrochemical reaction. For example, the water-splitting reaction requires around 1.8 V of photovoltage (including the overpotential), but the SQ limit shows that it would not be possible to achieve high efficiency when using a single junction solar cell for PEC.

2.2.2 Multi-junction solar cell

One of the most promising ways to overcome the SQ limit is a tandem or multi-junction approach. A multi-junction solar cell is made up of more than two single-junction solar cells with different bandgaps, which are monolithically integrated into a series. A large bandgap junction is placed on top of the low bandgap junction because large bandgap materials are transparent to low energy photons. Recombination layers are placed between the junctions, and photo-charge carriers (electrons and holes) generated from a junction recombines with photo-charge carriers from neighboring junctions to flow through the stack of junctions. Because the current is flowing through the solar cell by recombination at the interface, an excess amount of photo-charge carriers from a junction would not be able to transfer to the neighboring junction and will dissipate by photo-luminescence. Therefore, it is important to match the current density generated by each junction. The multi-junction solar cell can minimize the energy loss by absorbing broadband of spectrum thermal dissipation and achieves high efficiency by absorbing high energy photons in a

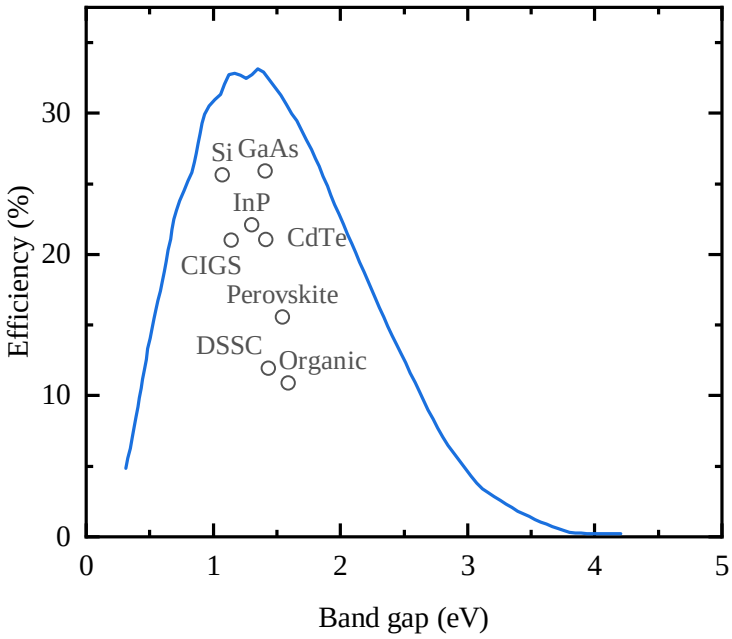

Figure 2.5: The efficiency of a solar cell illuminated with AM 1.5G spectral irradiance at room temperature. The solid line shows the SQ limit. The figure is reproduced from [36, 37].

large bandgap junction and lower energy photons in a lower bandgap junction. Figure2.6 shows the benchmark of solar cell efficiency, and the best solar cell efficiency has been achieved by multi-junction solar cell made of III-V materials.

The multi-junction solar cell for PEC should be able to generate a sufficient photovoltage to drive a water-splitting reaction. The thermodynamic potential for water splitting is 1.23 V and around 700 mV of overpotential would be necessary to overcome the activation energy of reaction and the ohmic loss. The current density between the junctions should be matched to be similar and should be as large as possible to maximize efficiency. Thus, a proper combination of the semiconductors would enhance the STH efficiency of a PEC device. Döscher et al. investigated the proper combination of materials for the tandem solar cell for the PEC water splitting device.

2.3 How to combine electrocatalysts and solar cell?

There are several different ways to combine electrocatalyst and solar cells and there are many factors to be considered for the system optimization. While the most straightforward way to combine them would be PV+EC, which establishes an electrical connection between commercial water electrolyzer and solar cell. Meanwhile, PEC, which is replacing the electrical connection with solid/liquid junction also emerged as a potential candidate. In the following section, a short introduction to PEC device and its several different types of configuration first, and it will be compared with PV+EC.

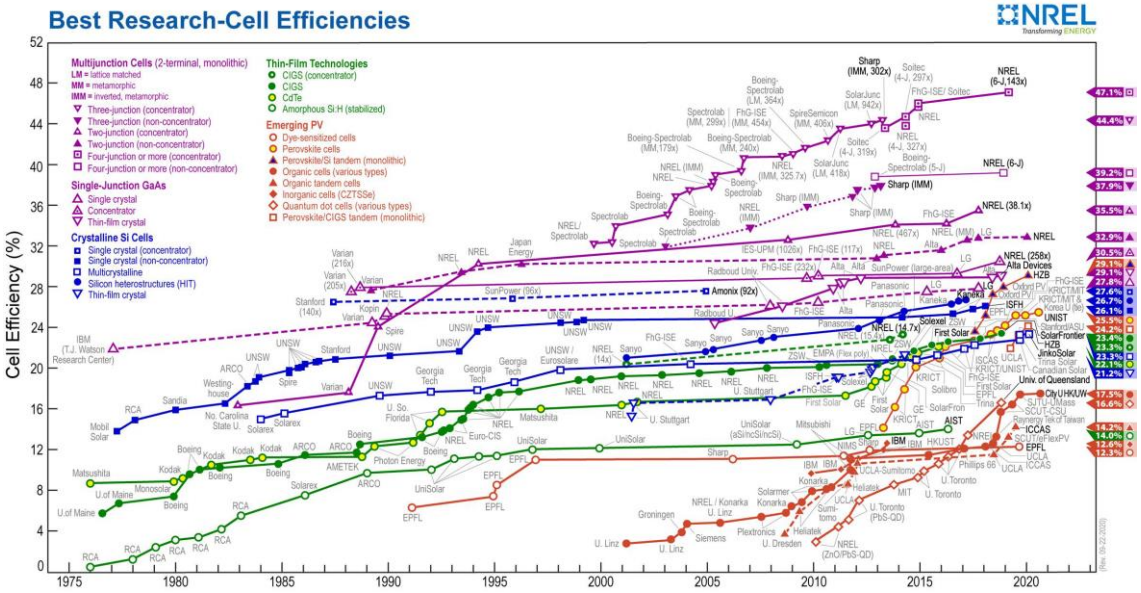

Figure 2.6: The benchmark on the solar cell efficiency.

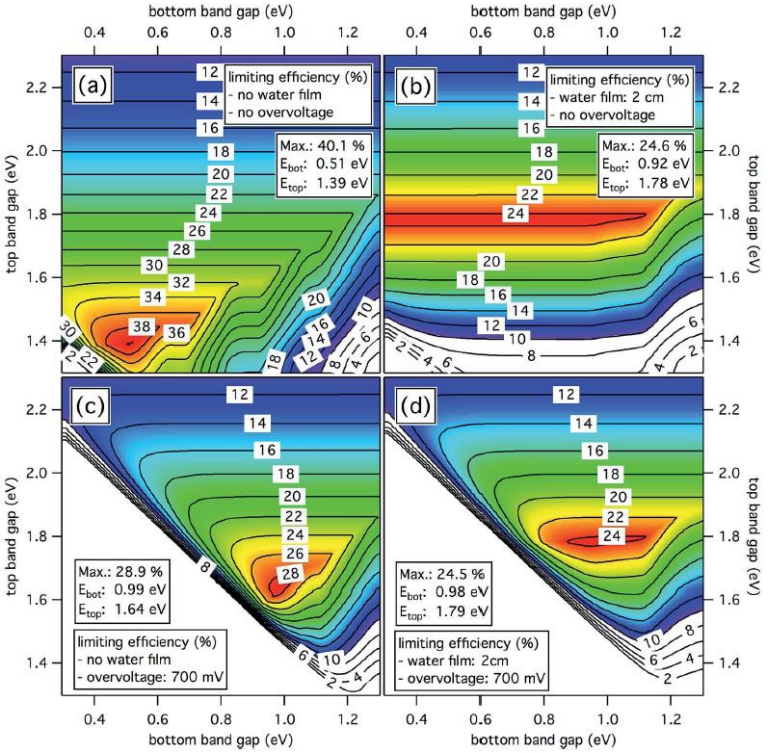

Figure 2.7: Theoretical investigation on PEC efficiency depending on the combination of semiconductors' band gap in a tandem solar cell.

2.3.1 PEC device configurations

PEC is a field of a study investigating an electrochemical reaction induced by photo-excited charge carriers on the surface of photovoltaics. PEC devices are made of a water electrolyzer integrated onto the surface of the solar cell. Figure 2.8 shows three typical structures of PEC devices found in literatures.

Probably, the most widely used type of configuration is the wired configuration (shown in Figure 2.8A) either in photocathode or photoanode. The light is illuminated on the front side of the PEC device through an electrolyte. The front side of the device is electrocatalysts. The backside of the device in the dark has a connection to reference or counter electrodes through a potentiostat and electrical wire. Photo-excited charge carriers are flowing between the working and counter electrode, and the potentiostat can measure the current density with high sensitivity.

The major difference between the inverted-wired configuration (shown in Figure 2.8B) and the wired configuration is that the inverted-wired configuration has a dry optical front side and wet backside while the wired configuration has a wet front side and dry backside. The optical front side in the inverted wired configuration is covered with a metal grid or TCO used for conventional solar cells which are leading to potentiostat and counter electrode. The backside is covered with electrocatalysts for an electrochemical reaction. The potential advantage of the inverted wired configuration compared to the wired configuration is that there are fewer restrictions on the protection layer against the electrolyte because the protection layer on the backside of the device does not have to be transparent. However, this configuration has to transport electrical charge across the surface of a solar cell, which results in higher ohmic resistance and system cost compared to other PEC configurations.

The last type of configuration is the wireless configuration (Figure 2.8C). Both front and backside of the solar cell are exposed to electrolyte and covered with electrocatalysts. Therefore, there is not any electrical connection to the device, and should be able to operate by itself. The wireless configuration would be the most interesting structure because it can fully utilize the advantage of PEC. The photo-excited current flows only over the thickness of the solar cell, and it can minimize ohmic loss from electron conduction. Furthermore, this configuration potentially lower system costs by removing any external wiring and other miscellaneous electronic components. However, due to the lack of external wiring and potentiostat, its performance can only be measured by analyzing the products from the wireless PEC device. The product analysis requires an electrochemical cell with a delicate design that gives low ohmic resistance and gas-tight tubings, which would be more challenging than collecting charges from electrically wired devices.

To sum up, the wireless configuration (Figure 2.8C)would be the most suitable design for practical hydrogen production because it can make the most of PEC's advantage. However, because of difficulties in characterizing the wireless device, wired or inverted-wired configurations (Figure 2.8A and B) are often used for scientific studies. Collecting

charges from the wired or inverted-wired device enables the facile characterization of the devices. Nevertheless, we should keep in mind that the charges may not be always originated from a desired electrochemical reaction. In addition, the inverted-wired configuration would not be able to take advantage of PEC by transporting electrical charges across the surface, especially at a large scale device for practical hydrogen production.

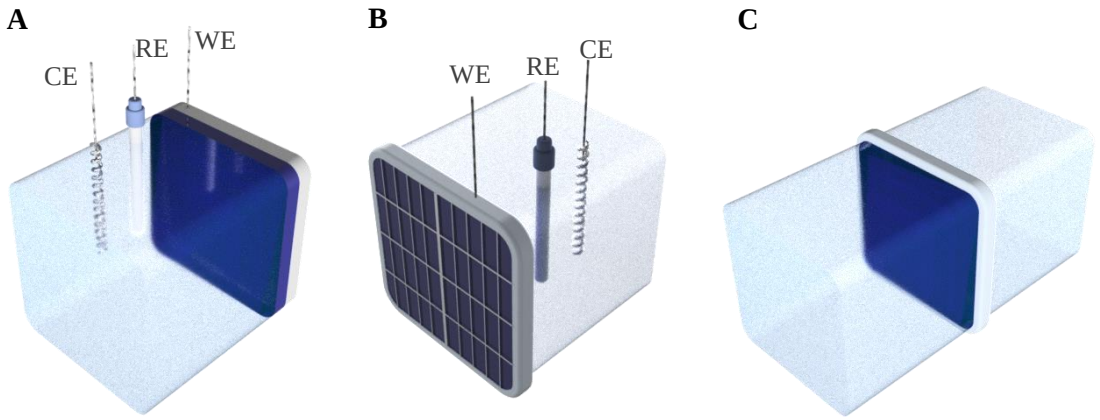

Figure 2.8: 3 types of PEC configurations. (A) wired, (B) inverted-wired and (C) wireless configurations

2.3.2 Solar to hydrogen conversion efficiency and unassisted solar water splitting

One of the most important figures of merit of PEC devices is solar to hydrogen conversion efficiency. The STH efficiency is expressed as the ratio between the thermodynamic energy acquirable from hydrogen outflux and the solar energy influx.

$$STH = \frac{f_{H_2} \times \Delta G}{P_{solar}} \tag{2.3}$$

Here, f_{H_2} is the flux of hydrogen in the unit of mol/cm^2/s, and ΔG is the thermodynamic energy for water-splitting, 237 kJ/mol. P_{solar} is the intensity of solar illumination 100 mW/cm^2. In most cases, the current density generated during the water-splitting reaction is collected instead of the gaseous products (H_2 and O_2) in the wired or inverted-wired configuration. In these cases, Equation 2.3 can be written in terms of the current density by using Equation 2.2.

$$STH = \frac{J \times U_{th}}{P_{solar}} \tag{2.4}$$

Here, J is the photocurrent density and U_{th} is the thermodynamic potential for water-splitting reaction. In the case of using a photoelectrode that cannot supply enough photovoltage to activate an electrochemical so that it needs assistance from an external power source, external energy input should be subtracted from the acquirable energy from hydrogen. The external energy assisting the reaction is equal to the current multiplied by the external bias.

$$STH = \frac{J \times (V_{th} - V_{ext})}{P_{solar}} \tag{2.5}$$

Here, V_{ext} represents the potential difference between working and counter electrodes.

2.3.3 Comparing PV+EC and PEC

The major difference between PEC and PV+EC is that photo-generated charge carriers from PEC participate in an electrochemical reaction directly on the surface of the solar cell, while the charge carriers from PV+EC flows to the water electrolyzer through electrical contacts and power electronics. The difference makes PEC potentially be more advantageous for both improving efficiency and reducing system cost compared to PV+EC. PV+EC collects and injects photocurrent into a water electrolyzer operating at high current density ($\sim$ 1 A/cm^2). Because the water electrolyzer operates at a high current density, large ohmic loss occurs due to electrical resistance. Increasing the number of electrolyzers connected to solar cells would reduce the ohmic loss, but the expensive cost of water electrolyzer forces to use a small number of water electrolyzers and put up with a large ohmic loss. On the other hand, PEC devices operate with a low current density ($\sim$ 10 mA/cm^2) flowing over a very short distance because photo-excited charge carriers are widely distributed over the large surface area of the solar cell and participate in an electrochemical reaction on site. Thus, ohmic loss by electrical resistance would be much lower compared to PV+EC. In addition, PEC does not require power electronics such as DC-DC inverter, which is mandatory for the PV+EC system and usually has 10 % of loss during the conversion. From a cost point of view, the solid/liquid junction in PEC needs much less effort to be prepared compared to electrical contact in a solid-state device. The electrical contact in a solid-state solar cell often requires a metal patterning process for extracting charge carriers. When considering the front surface metallization accounts for the most expensive single step in the manufacturing process of commercial crystalline silicon solar cell[38], replacing the electrical contact with solid/liquid junction would be a much economic approach. Moreover, PEC does not require the intermediary components such as DC-DC inverter for matching different operation voltage between photovoltaics and electrolyzer.

2.4 The most critical challenges in realizing practical hydrogen production by PEC

Although PEC could be more advantageous over PV+EC in combining solar cells and electrocatalysts, there are also challenges in PEC that have to be resolved to be economically feasible technology for hydrogen production. The first and most important limitation of PEC would be the stability of the PEC device. Because most of the semiconductor materials for solar cells are unstable in acidic or alkaline electrolytes, thus, the lifetime of PEC devices are usually much shorter than the solid-state solar cells. Secondly, the activity of a solar cell in PEC configuration is still less active compared to its dry solid-state counterpart because PEC lacks a good anti-reflection coating. Lastly, the ohmic resistance from the proton conduction can potentially cause significant loss, especially for a large-scale device. In the following sections, each problem will be further discussed in detail, and the approaches taken in this thesis will be introduced.

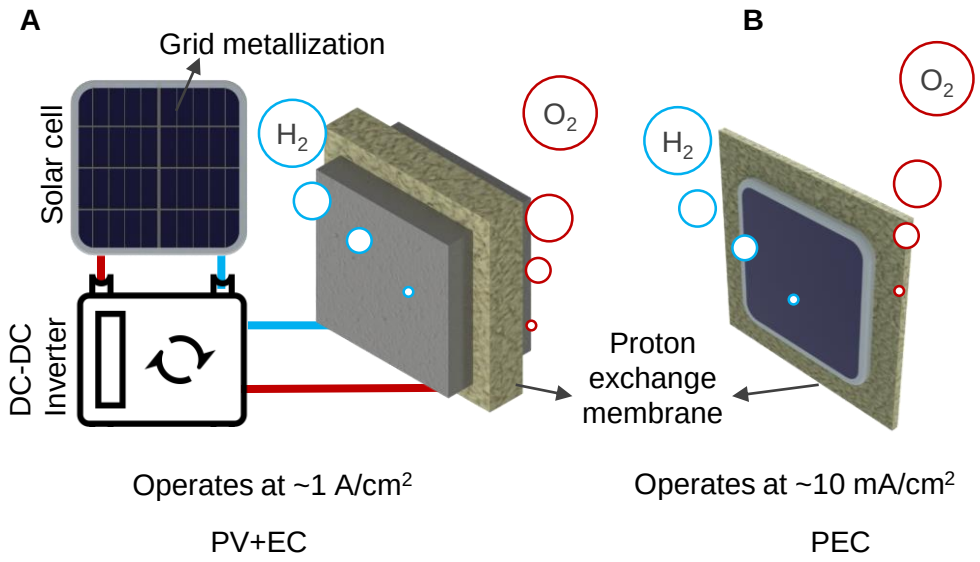

Figure 2.9: Comparison between (A) PV+EC and (B) PEC. PEC has less ohmic loss by operating at lower current density and a concise system architecture.

2.4.1 Overcoming the stability gap

The most critical issue in the PEC study has been the stable operation of a solar cell in a corrosive environment. There have been studies for improving the stability of PEC devices, however, state-of-art PEC devices run around tens of days.[39] When considering that the warranty period of commercial solar cells is usually 20 years, the stability of PEC devices has to improve significantly. Probably the most common approach to resolve the stability issue in PEC devices is the coating protection layer, which is covering the surface to avoid direct contact between the solar cell and an electrolyte. An ideal protection layer is expected to be transparent, conductive, stable and impermeable to an electrolyte[40], and series of materials including TiO_2, $SrTiO_3$, MoS_2 and others have been investigated as a protection layer. However, the stability of PEC devices are still far away from a satisfactory level. Ben-Naim et al. compared PEC devices in literature and PEC Goal (suggested by DOE) and pointed out that while STH efficiency is getting closed to PEC Goal, the stability of PEC devices still has to be improved by two orders of magnitude to find economic feasibility in hydrogen production by PEC.

In this study, titanium dioxide layer is adopted as a protection layer[41–48] because it satisfies aforementioned requirements except impermeability. TiO_2 is stable in a broad range of pH and electrical potential and also transparent over a broad range of visible light. Furthermore, its conduction band edge is well aligned with hydrogen redox potential, and it facilitates the conduction of electrons without energy loss.[41] However, pin-holes or cracks in the TiO_2 protection layer allows contact between a solar cell and electrolyte, and it leads to the poor stability of TiO_2-protected PEC devices. This study shows that thickening the TiO_2 protection layer and carefully controlling the deposition condition can reduce or remove pin-holes in the protection layer. Furthermore, this study shows that

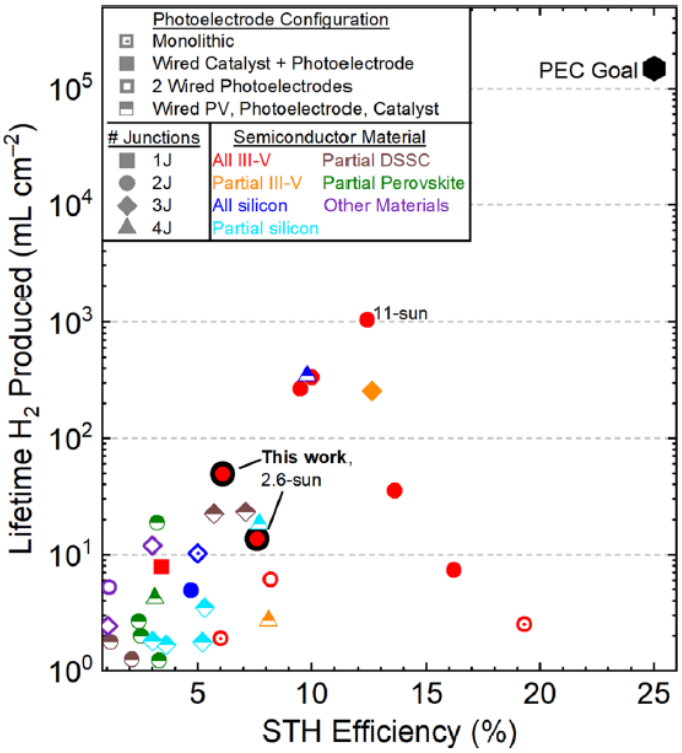

Figure 2.10: The stability gap addressed by Ben-Naim et al. For PEC to achieve economical feasibility, device performance has to reach ”PEC Goal”.

UV-illumination can improve the stability of a PEC device.

2.4.2 Reducing optical loss

The optical reflection of any light-harvesting device has to be minimized to acquire ideal efficiency, and an anti-reflective coating is usually deposited in front of a solar cell in this regard. Thus, PEC devices need to have an anti-reflection coating as good as that of the conventional solar cell to be comparable to PV+EC. However, it is challenging to develop an anti-reflection coating for PEC because of design restrictions. Unlike conventional solar cells, the anti-reflection for PEC has to conduct charge carriers, stable in acidic electrolytes. The difficulties in preparing a good ARC for PEC make PEC performance less active compared to PV+EC made of the same photoabsorber. For example, the conventional GaInP/GaInAs tandem solar cell with a good anti-reflection coating achieves 32 % of efficiency, and when the tandem solar cell is combined with a water electrolyzer with 70 % of efficiency, STH efficiency would be 22.4 %. However, the current state-of-art PEC device made of the same GaInP/GaInAs tandem solar cell has only 19 % of STH efficiency, as shown in Figure 2.11. The PEC device tries to minimize its reflection by controlling the thickness of the protection layer, which also serves as a monolayer anti-reflection coating. However, there is around 15 % of discrepancy compared to theoretical maximum, and it is mainly from the loss by reflection.

In this study, because the titanium dioxide layer is deposited on top of III-V solar cell as a protection layer, and its performance as the anti-reflective coating is characterized. The

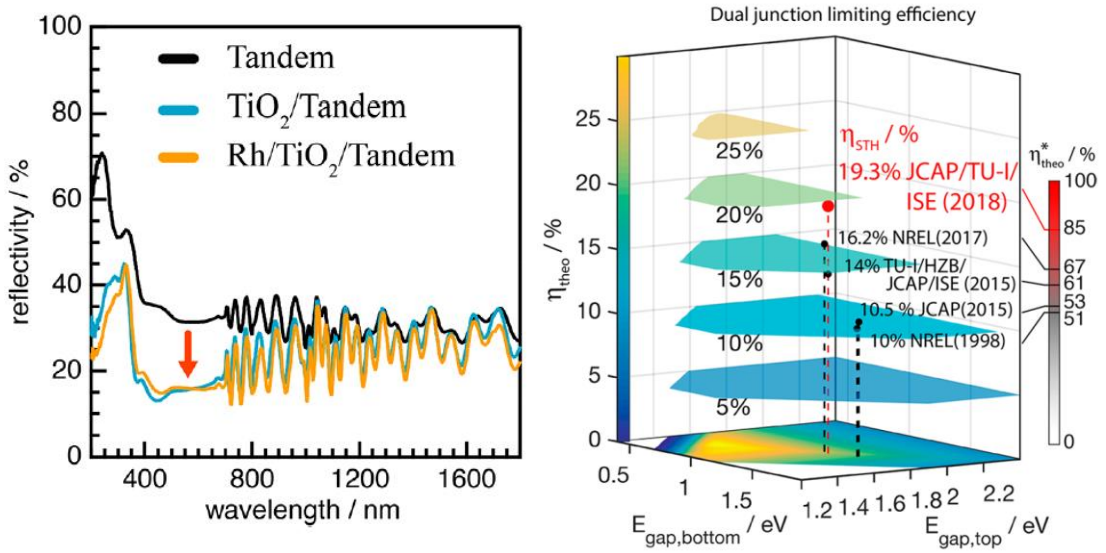

Figure 2.11: STH efficiencies of state of art PEC devices. The major difference between the theoretical maximum efficiency and experimental efficiency comes from optical loss.

thickness of TiO_2 ranges from 50 to 400 nm, and its effect on reflection and device activity is investigated by using both experiment and calculation. The study shows the current density from each junction and which of the junction is limiting the current density in III-V solar cell. The limitation of monolayer TiO_2 as ARC is also discussed and a potential strategy to improve it is also suggested.

2.4.3 Electrochemical cell design

Although PEC can reduce ohmic loss from electron conduction drastically, it could have an ohmic loss from proton conduction. This problem is not an issue in a small laboratory scale device ($\sim$ 1 cm^2), but it would become a serious issue when it comes to a practical scale device ($\sim$ 10 cm^2) for hydrogen production. The ohmic loss from electrolytes take place along the distance between the working and counter electrode, thus, it is important to minimize the distance between them. In a laboratory-scale device without gas separation, where the size of the PEC device is less than 1 cm $\times$ 1 cm scale, the ohmic loss from the electrolyte has not been a serious issue because it is easy to place small working and counter electrode closed to each other. However, a practical PEC device for hydrogen production would require a larger device area with gas separation, for example, larger than 10 cm $\times$ 10 cm scale. Depending on the device structure, ions in electrolytes should travel across the large surface of PEC device, and it will result in a large ohmic loss. There are several theoretical and experimental studies investigating the scaling effect[49–52], for example, Haussener et al. conducted a theoretical study showing that ohmic voltage drop of a one-dimensional wireless device increases as the device size scales up, especially when the water layer thickness in front of the water layer is getting thinner.[52] Thus, a clever design for an electrochemical cell is necessary to minimize ohmic loss from an electrolyte.

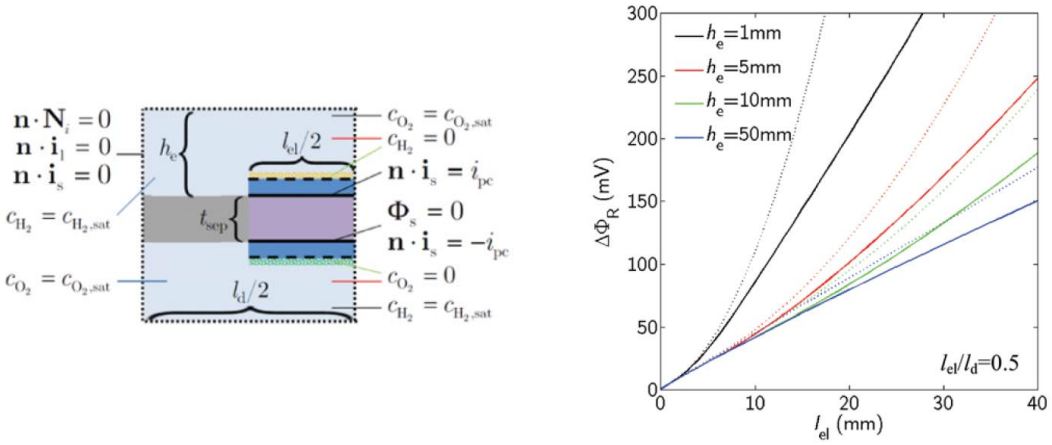

Figure 2.12: Theoretical study on a the effect of device size on the performance of a device.[52]

This thesis focuses on a laboratory scale PEC device whose surface area is around 0.2 cm^2 and the PEC device on a large scale is out of the scope of this thesis. However, an electrochemical cell for testing a laboratory-scale PEC device in the wireless configuration is designed, and ohmic loss in the cell is investigated. Based on the specific cell design, difficulties in up-scaling PEC by ohmic loss is discussed.

2.5 Technoeconomic analysis on PEC from previous studies

In the previous sections, major advantages and challenges in PEC study are introduced. To clarify how much improvement is required to overcome the challenges and how much cost reduction is expected from PEC, this section will introduce several selected previous techno-economic analyses on PEC.

There have been several techno-economic analysis on PEC considering many factors based on many assumptions. According to Sharner et al.[53], who conducted a techno-economic analysis comparing PV+EC and PEC in 2016, the costs for balance-of-system (BOS) of PEC and PV+EC are 55 USD/m^2 and 106 USD/m^2, respectively. The lower BOS cost is originated from 1) gas collection from PEC at low pressure is less expensive compared to power electronics for PV+EC, and 2) the cost for mounting integrated PEC unit is less complicated than that for mounting separated PV+EC module. However, they assumed that the lifetime of a PEC device (7 years) would be much shorter than that of a dry solar cell (20 years), and it makes the levelized cost for hydrogen production by PEC (11.4 USD/kgH_2) to be similar with that by PV+EC (12.1 USD/kgH_2) at the same STH efficiency (10 %). The techno-economic analysis from Pinaud et al.[54] also drew a similar conclusion in 2013 (10.4 USD/kgH_2). These results imply that PEC devices should be stable enough to run more than 7 years to be competitive over PV+EC. Assuming 10 % of STH efficiency and 20 % of capacity factor (the portion of operation time in a day), 7 years of operation corresponds to producing 42 L/cm^2 of hydrogen over its lifetime. The long-term goal suggested by DOE (25 % of STH efficiency, 10 years of lifetime and 20 %

of capacity factor) is 149 L/cm^2.[55] However, there is no PEC device that has reached this value, as shown in Figure 2.10. As pointed out by Ben-Naim et al.[56], there are still two orders of magnitude difference between the PEC goal and the current PEC devices.

In addition to the improvement in the stability of PEC devices, a cost-efficient photoabsorber would be necessary for solar hydrogen production (both PV+EC and PEC), because they are still much more expensive compared to the technologies based on fossil fuels. SMR or gasification spends only 1 $\sim$ 2 USD/kgH_2[6] based on the current level of technology, and it is much more affordable compared to solar hydrogen production ($\sim$ 10 USD/kgH_2). Cost analysis show that when STH efficiency is improved to be 20 % (or 25 %), the cost for hydrogen production decreases to 6.1 USD/kgH_2 (or 5.1 USD/kgH_2). According to Figure 2.7, 25 % of STH efficiency would be achievable by a tandem solar cell made up of two semiconductors whose band gaps are 1.8 and 1.1 eV. Although the combination of semiconductors can be realized by III-V solar cells, III-V materials are still too expensive for a practical application yet. Unless a significant cost reduction in III-V solar cell is realized, other materials for tandem solar cells have to be prepared. Because silicon has 1.1 eV of the band gap and has been studied for many years, it would be ideal for a lower bandgap junction for the tandem solar cell. On the other hand, larger bandgap material for the tandem solar cell is still under development.

A major portion of solar hydrogen production cost comes from semiconductors for photovoltaics.[53, 54] Therefore, cost reduction by combining a PEC device and solar concentration for reducing the area of the expensive solar cell could be possible. The techno-economic analysis on PEC devices with 10:1 concentration would cost 2.9 USD/kgH_2[54] (7.4 USD/kgH_2, when assuming higher cost for the solar concentrator and shorter lifetime[53]), assuming that 25 % of STH efficiency and 10 years of lifetime. Besides, PEC could be more attractive compared to PV+EC when combined with the solar concentrator because circulating electrolyte can remove heat from a solar cell. The heat removal by electrolyte can prevent efficiency loss by high temperature and also provide a chance to reuse heat.

2.6 Major questions on PEC and the approaches taken in this thesis

To sum up, the major issue in the PEC addressed in the previous sections and the approaches are taken in this thesis are summarized as follows:

- STH efficiency of PEC is still less than the theoretical maximum.
  - For the state-of-art device, the discrepancy between measurements and the theoretical maximum is mainly from optical loss.
  - PEC devices have a larger optical loss compared to conventional solar cells because it does not have a proper anti-reflective coating.
  - In this study, TiO_2 protection layer also serves as the anti-reflective coating.

The optical effect from the protection layer is investigated, and a potential pathway for improvement is discussed.

- PEC devices have a poor stability in electrolyte.
  - Most solar cell materials are unstable in acidic or alkaline electrolytes, and it results in poor stability.
  - Protection layers for PEC devices have been studied, however, complete protection against electrolyte has not been realized.
  - In this study, various thicknesses of TiO_2 protection layer has been investigated and brings a significant improvement compared to the previous studies. The corrosion mechanism of PEC devices is investigated and strategies for improving stability are discussed.
- PEC device at a large scale
  - There are only a few cases that demonstrate hydrogen production by PEC on a large scale because of the difficulties in designing an electrochemical cell for a large-scale PEC device.
  - Large-scale PEC device is out of the scope of this thesis, however, electrochemical cell for a lab-scale device is designed and tested. Based on the result and discussed

CHAPTER 3

Experimental methods

The PEC study requires a variety of experimental methods for device preparation and characterization. This chapter will focus on important experimental methods and procedures carried out it this thesis.

3.1 Sample preparation

The PEC devices used in this study are prepared by depositing a protection layer and catalysts on a solar cell. This section starts by introducing the solar cell used in this study and introduces three different deposition techniques (sputter, atomic layer deposition (ALD) and e-beam evaporation). Lastly, the overall process for device preparation including details will be introduced.

3.1.1 Solar cell used in this study

The triple-junction solar cell used in this study is purchased from AZUR SPACE Solar Power GmbH. The three junctions in the solar cell are made up of III-V materials with three different bandgaps: GaInP (1.8 eV), GaAs (1.4 eV) and Ge (0.7 eV), respectively. The solar cell is optimized for operation in aerospace. Figure 3.1 shows the internal quantum efficiency provided by the solar cell manufacturer.[57] Under AM 0 spectrum (details on sunlight spectrum will be introduced in the later, section 3.2.1), the photovoltage and photocurrent are 2.7 V and 17.1 mA/cm^2, respectively. It should be noted that the photocurrent generated from each junction is matched to be similar because the excess amount of electrons and holes from a junction will fail to transport to its neighbouring junction. Thus, the total current density from the multi-junction solar cell is limited by one of the junction with the lowest current density.

3.1.2 Sputter

The deposition of materials on a substrate can be carried out by exposing the substrate to the stream of ionized atoms. The source of the atoms can be created from a target, which is a bulk of the desired materials placed nearby the substrate. By impinging the target with an inert and energetic projectile, the atoms from the target pop up to reach surroundings including the substrate. (Figure 3.2) The projectile is usually ionized noble

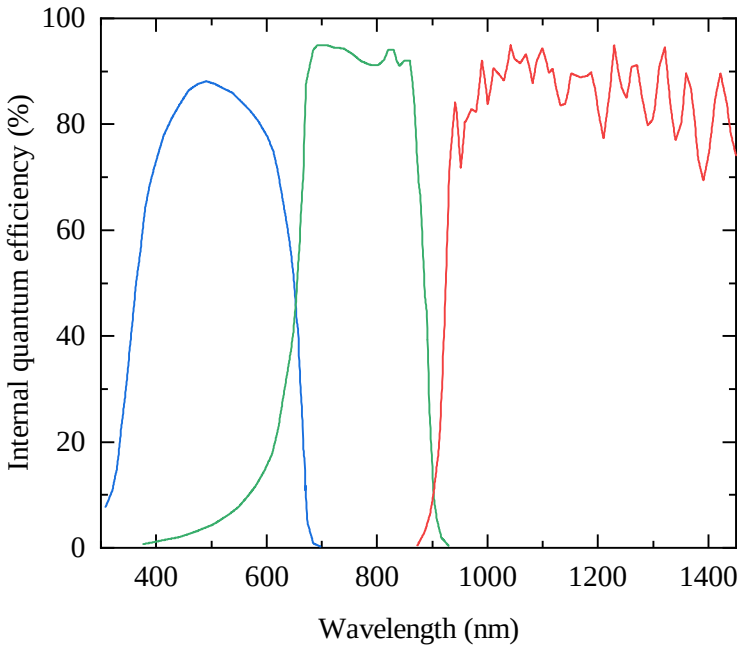

Figure 3.1: The external quantum efficiency of a triple junction solar cell provided from AZUR space. The figure is reproduced from [57]

gas atoms, which is ionized by an electric field created between the target and the electrically grounded surrounding. The ionized gas is accelerated to the surface of the target, and the flux of particles is guided and focused on the target using a magnetic field created by a strong magnet placed under the target.

To acquire a sufficient amount of noble gas ions bombarding on to the target, the noble gas pressure is controlled to be a proper level that can maintain a stable glowing arc plasma, which is an avalanche of gas ionization. When there is an ionized gas molecule, an electron is ejected from the gas molecules travels until it hits another gas molecule. In the course of the travel, the electric field supplies energy to the electron, and if the amount of energy is larger than the ionization energy of the gas molecule, the electron will ionize the encountered gas molecule and eject another electron. This will induce a chain reaction of ionization and generate a plasma. Therefore, the generation of plasma depends on the strength of the electric field and the mean free path of electrons. Paschen's curve depicts an empirical relationship between the minimum voltage required for plasma generation, pressure and the distance between the electrode.(Figure 3.3)[58] While the distance between the electrode is given by a system, the pressure is related to the inverse of the mean free path of electrons, according to Boltzman's ideal gas law. When the pressure is too high, electrons from ionized molecules hit another gas molecules before it gets sufficient energy for ionization, and when the pressure is too low, electrons will get sufficient energy, but they will hardly encounter another gas molecule. Assuming that the

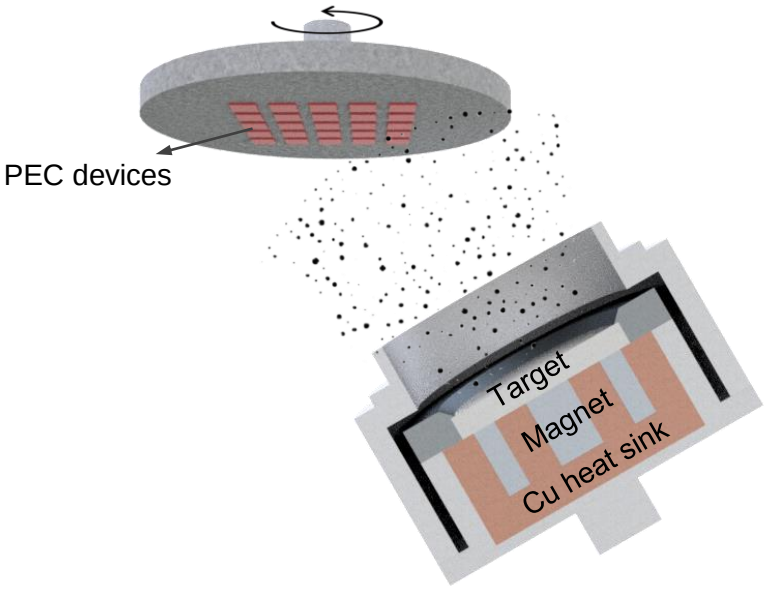

Figure 3.2: A schematic diagram of sputter for thin film deposition

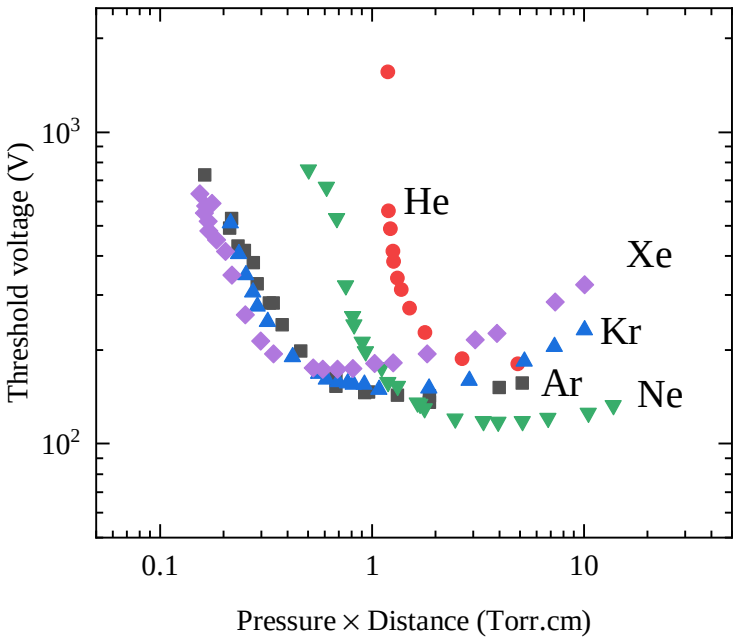

Figure 3.3: Empirical correlation between the minimum voltage required to generate plasma depending on the multiplication of pressure and the distance between two electrodes. The figure is reproduced from [58]

distance between the electrode (between the target and grounded surrounding) is around 10 cm, the proper level of pressure is around 100 mTorr ($\sim$ 0.1 mbar). However, actual deposition is usually carried out in a much lower pressure range (1 $\sim$ 10 mTorr) to extend the mean free path of sputtered species and increase the deposition rate of materials.

Among the noble gases for sputtering, argon is preferred in many cases because of its large atomic mass and its price. Figure 3.4 shows the sputter yield (the number of ejected target atoms per the number of impinging projectile atoms) of target materials used in this thesis depending on the energy of projectile atoms.[59] It shows that argon has the larger sputter yield compared to helium because of its larger atomic mass.

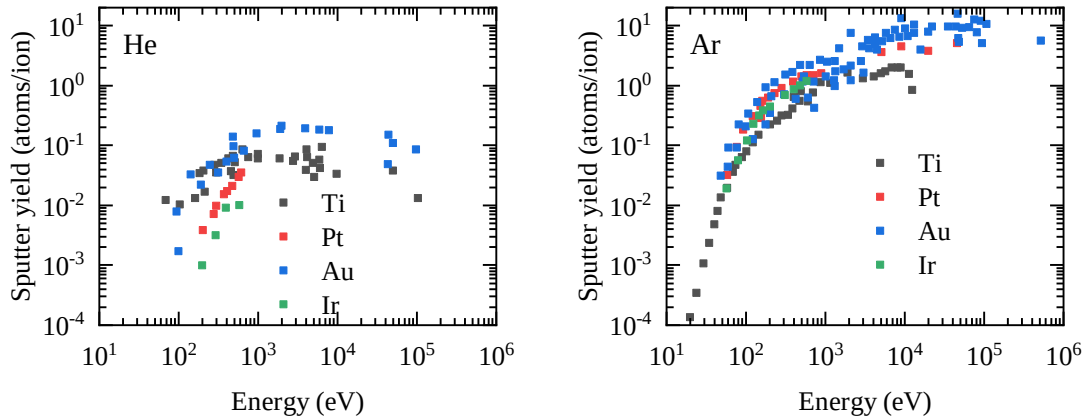

Figure 3.4: Sputter yield of materials deposited by sputter in this thesis. The figure is reproduced from [59]

Materials preferred as a target in sputtering are mostly metallic materials because their high electric and thermal conductivity is less likely to cause problems from thermal expansion. To deposit materials other than metals, it is possible to induce a reaction by introducing a reactive gas together with the inter gas during the deposition. For example, while sputtering a metallic target, introducing oxygen or nitrogen colliding with the atoms ejected from a target, and it will deposit an oxide or nitride layer. Alternatively, instead of introducing the reactive gas, the target itself can be an oxide, nitride or other types of alloy targets. If the electrical and thermal conductivity of the alloy target is low, a radio-frequency (RF) power supply should be used to mitigate the thermal expansion problem.

In this thesis, the sputter is mainly used to deposit titanium dioxide protection layer, platinum, and iridium oxide as HER and OER catalysts. The titanium dioxide layer is deposited by using a titanium target with 180 W of DC power source under 5 mTorr of argon/oxygen mixture in 10 to 1 ratio. The platinum catalyst is deposited with a platinum target with 80 W of DC power source under 3 mTorr of argon pressure. The iridium oxide catalyst is deposited by using an iridium target with 80 W of DC power source under 5 mTorr of argon/oxygen mixture in 4 to 1 ratio.

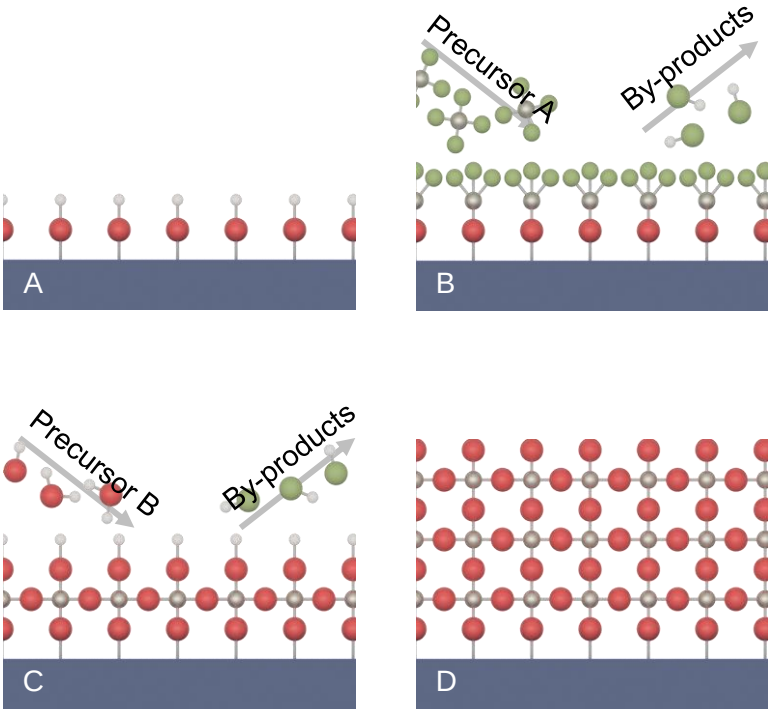

Figure 3.5: The schematic diagram of ALD process. (A) A surface functionalized for a reaction. (B) Precursor A reacts with the surface to forms a monolayer of thin-film and by-products. (C) Precursor B is introduced to form another monolayer on top. (D) Thin-film of materials can be deposited by repeating (B) and (C).

3.1.3 Atomic layer deposition

ALD is a thin film deposition process by a series of chemical reactions in vapor phase over the surface of substrate. Figure 3.5 shows a schematic diagram of the ALD process. ALD process starts from a surface functionalized with a chemical species to start a reaction.(Figure 3.5A) When a precursor A is introduced to the chamber, it reacts with the surface functionalization to form a monolayer of thin-film, leaving some by-products depending on reactions. (Figure 3.5B) Because precursor A can only react with the surface functionalization, it will not create a bilayer of film. After removing an excess amount of the precursor A and by-products by pulsing an inert gas, precursor B is introduced into the chamber to form another monolayer on top of the layer deposited by the precursor A. (Figure 3.5C) For the same reason, The layer created by the precursor B is self-limiting and will not create a bilayer of film. On top of the layers, the precursor A and B can repeat the same reaction to deposit a thin film.(Figure 3.5D)

The advantage of ALD is that 1) conformal deposition of a thin film without pin-hole is possible, and 2) by controlling the number of cycles, it can precisely control the thickness of the thin film.[60] These advantages are attributed to the self-limiting nature of the ALD deposition process.

These advantages make ALD very suitable adequate for depositing titanium dioxide

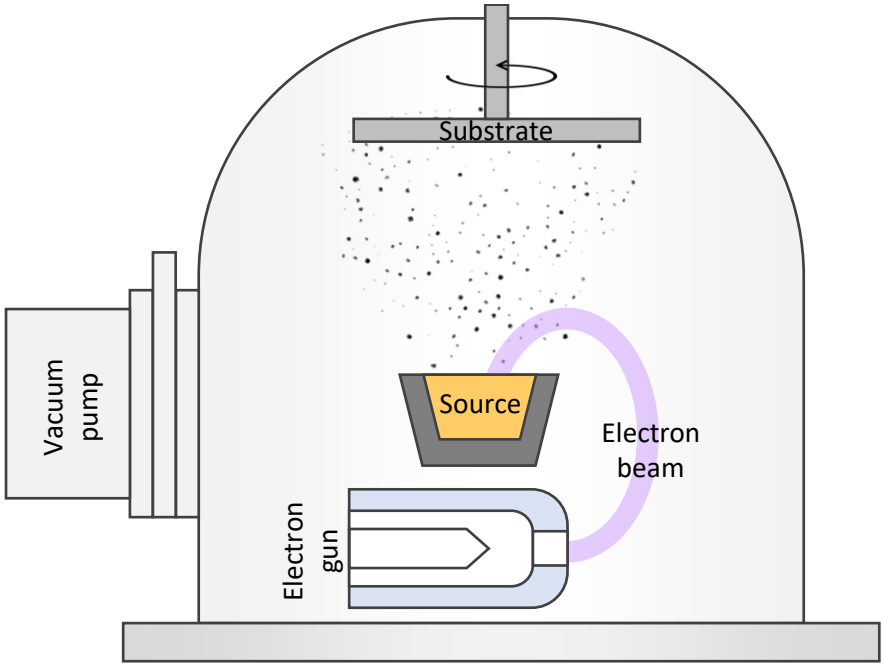

Figure 3.6: Schematic diagram of e-beam evaporator. The electron beam generated from the electron gun transfer energy to the source and the source evaporates to the substrate.

layer, which is used as a protection layer and anti-reflective coating in this thesis. It is expected that the titanium dioxide layer deposited by ALD would be less permeable to electrolyte because the layer is less likely to have pin-holes. Furthermore, the thickness of the anti-reflective coating can be precisely controlled to acquire a minimum reflectance and improve efficiency. In this study, the ALD for titanium dioxide thin-film uses titanium chloride and water as precursors for the reaction.

$$TiCl_4 + 2H_2O \rightarrow TiO_2 + 4HCl \tag{3.1}$$

$TiCl_4$ and H_2O precursors are pulsed for 0.1 s for each cycle, and the deposition process is usually carried out at 250 °C.

3.1.4 E-beam evaporation

E-beam evaporation is a thin film deposition technique that uses an electron beam to makes source materials vaporized and condensed on a substrate. The e-beam evaporator is made of four major components: an electron gun, source materials contained in a pocket, a substrate and a chamber with a vacuum pump.[61] The generation of electron beam from the electron gun will be explained in the section 3.2.5. The electron beam is guided and focused on the source materials by using an electric or magnetic field. The kinetic energy of electrons transferred to the source materials will make atoms on the surface evaporate and travel across the chamber. The pressure of the chamber is kept to be low enough to make the mean-free path of the atoms longer than the distance between the source materials and substrate.[62].

The deposition rate of materials will depends on the evaporation rate of the source, and the relative position and angle between the source and substrate. The evaporation rate of materials can be estimated based on the classical kinetic theory.[63] The number of atoms N leaving a surface with area A over time t is formulated as below:

$$\frac{dN}{Adt} = \alpha(p_v - p)\sqrt{\frac{N_A}{2\pi M k_B T}} \tag{3.2}$$

Here, p_v and p are the vapor pressure and chamber pressure, respectively. M and T are the atomic mass and temperature of the source, respectively. k_B and N_A are Boltzmann's constant and Avogadro's number, respectively. α is an evaporation coefficient between 0 and 1, and the value strongly depends on the condition of the surface.[63] The vapor pressure of materials is a physical parameter that represents thermodynamic equilibrium pressure at a given temperature in a closed system. The difference between the vapor pressure and the chamber pressure $(p_v - p)$determines the direction of the phase transition to be either evaporation or condensation. The vapor pressure of materials is depicted in Figure 3.7. To acquire a reasonable deposition rate, the temperature of source materials is heated up to have the vapor pressure larger than 10 mTorr, and the chamber pressure is kept to be much lower than that. By controlling the relevant parameters, the deposition rate of e-beam evaporator ranges from 10 nm/min to 100 μm/min[61], and its capability of faster deposition rate compared to the other deposition techniques introduced in the previous sections (sputtering and ALD) is a major advantage of e-beam evaporation. Therefore, an e-beam evaporator is used for depositing a metallic titanium layer thicker than one micrometer in this study.

3.1.5 PEC device preparation

The PEC device studied in this thesis is based on solar cell wafers provided from AZUR SPACE Solar Power GmbH. The PEC devices are prepared by using the aforementioned deposition techniques on both sides of the solar cell wafers. The device preparation always starts from a series of cleaning and deposition procedure for the backside (Ge substrate). In the first step, the solar cell wafer is sonicated in ethanol and water for 2 minutes each to remove organic contamination. After the sonication, the native oxide layers are removed by rinsing in 1 M HCl and water for 2 minutes and 5 minutes, respectively. According to the reference[65], a monolayer of the native oxide layer on a pristine Ge (100) or Ge (111) substrate grows in around 30 minutes. Therefore, the cleaned wafers are placed in a sputter or e-beam evaporator chamber under a vacuum soon after the cleaning process. If possible, the Ge backside is cleaned once more by sputtering Ar ions, and 10 nm of gold layer is deposited as a contact layer. In the case of a wireless device whose backside will be opened to an electrolyte, 2 μm of metallic Ti is also deposited over the gold layer as a protection layer by an e-bean evaporator as shown in Figure 3.8B.

After the deposition on the backside, the TiO_2 protection layer is deposited on the front side and diced into small pieces with 1 cm $\times$ 1 cm size. Before starting the deposition, the front side of the solar cell is treated by a mixture of citric acid solution (50 %wt) and

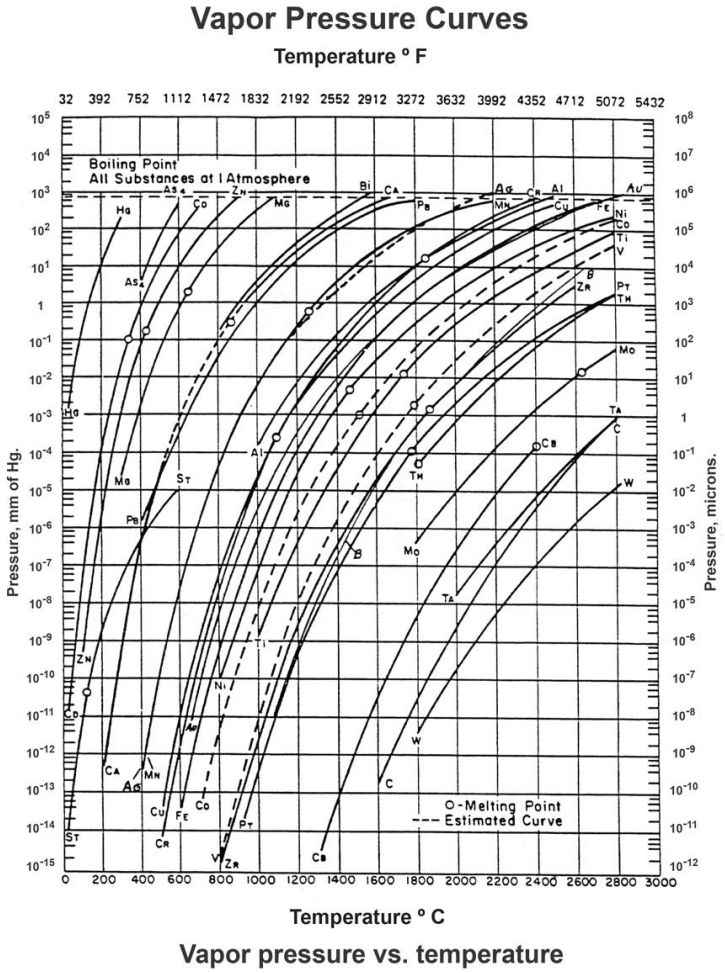

Figure 3.7: Vapor pressure of materials. The figure is taken from [64]

hydrogen peroxide(30 %wt). The mixture is prepared by mixing the citric acid solution and hydrogen peroxide in a 5:1 volume ratio. Soon after the chemical treatment, the wafer is placed in a sputter chamber to deposit 3 nm of metallic Ti, which works as an adhesion layer between the TiO_2 protection layer and the solar cell wafer. After the deposition of Ti, TiO_2 protection layer is deposited either by sputter or ALD as shown in Figure 3.8A.

The wafer covered with TiO_2 is diced into small pieces with 1 cm $\times$ 1 cm size to be able to make many devices from one wafer. Because the dicing process can potentially cause mechanical or electrical damage (e.g. debris from the dicing process could sit on the cross-section of the solar cell stack lower the shunt resistance), it is important to avoid any contact between the dicing blade and solar cell junctions. To prevent the damage, the cutting has to start from the backside to the front side of the wafer and the depth of cutting is controlled to be around 70 $\sim$ while the total thickness of the wafer is $\sim$ 150 μm. After cutting the wafer only half-depth, the wafer is cleaved by gently pressing with fingers. After cutting the wafers into small pieces, the stack of III-V solar cell materials is opened on the edge side, and it is important to prevent any damage or contamination on the edge side because it often lowers the shunt resistance of the solar cell and deteriorates performance. Thus, any kind of touching on the edge side is avoided while handling the pieces of wafers and Teflon tweezer is always used instead of a metallic tweezer to prevent mechanical damage.

The dicing process also can also be carried out before TiO_2 protection layer deposition. The advantage of dicing before TiO_2 deposition is that it is possible to change the TiO_2 deposition condition for every sample. Thus, the samples used for investigating the effect of TiO_2 thicknesses are prepared by this method. However, there is a risk of damaging the solar cell by depositing materials on the exposed cross-section of the solar cell. After dicing the wafers, the stack of the solar cells are exposed on the edge side of the solar cell pieces, and the deposition of materials over the exposed side could lower the shunt resistance of the devices. Therefore, a shadow mask is used when sputtering after dicing. ALD deposition is not allowed after dicing the wafers because, as explained in the previous section 3.1.3, ALD is a chemical reaction in the vapor phase, and it deposit materials on every opened surface in the ALD chamber.

Pt nanoparticles with 0.5 nm of nominal thickness are also deposited as an HER catalyst over the TiO_2 protection layer using sputter and a shadow mask. Before the deposition of Pt, the sample is cleaned by sputtering Ar ions for 5 minutes. After the deposition of Pt, the surface is sputtered again by oxygen ion for 2 minutes to functionalize the surface with hydroxide. Functionalizing the surface with hydroxide makes the sample surface hydrophilic and facilitates the hydrogen bubble removal during the PEC experiment. However, the sample exposed to air usually lost its hydrophilicity in an hour, possibly due to the contamination from the air. To avoid contamination from the air and maintain hydrophilicity, the samples are often kept in clean millipore water. Alternatively, hydrophilicity can be recovered by illuminated with UV light on the sample. The large bandgap of TiO_2 under UV

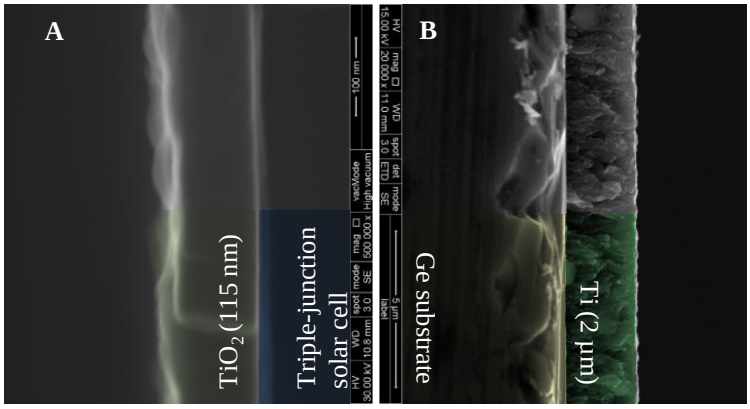

Figure 3.8: The crosssection image on the front side (left) and the backside (right) of the PEC device.

light generates highly energetic charge carriers that can degrade carbon contamination on the surface.

In the case of a wireless device, 20 nm IrO_2 is sputtered over the backside covered with 2 μm of metallic Ti. In the case of wired samples, copper wire is attached on the backside covered with the gold layer using a silver paste instead of the thick metallic Ti layer. The sample and the copper wire are encapsulated in an epoxy and glass tube with a reaction area on the front side. The epoxy used in this study is LOCTITE® Hysol® 1C™.

3.2 Characterization

The performances of wired and wireless devices are evaluated under a light source simulating the sunlight. The performances of wired and wireless devices are measured by collecting the photocurrent density and by collecting the gaseous product, respectively. In the following sections, the light sources and experimental setup used for the measurements will be introduced in detail.

3.2.1 Light source

PEC devices are expected to operate in an outdoor condition under the natural sunlight when this technology is put to practical use. The intensity of the natural sunlight depends on many factors such as time, latitude and weather. The intensity of sunlight before entering the atmosphere is defined as air mass (AM) 0 spectrum, which is close to the black radiation spectrum from the sun's surface temperature ($\sim$ 5500 K).[66] As the light travel through the atmosphere, a certain portion of the spectrum is lost by scattering or absorption. In the short wavelength range (< 700 nm), Rayleigh scattering by molecules and particles in the air reduces intensity. In the long-wavelength range (> 900 nm), absorbed mostly by interaction with water molecules in the air. The absorption by air will also depend on the latitude because the length of the path through the atmosphere will depend on it. The solar light intensity at the latitude 48.2° is referred to as AM 1.5 spectrum, and the number 1.5 comes from $1/cos(48.2) = 1.5$. The spectrum around the

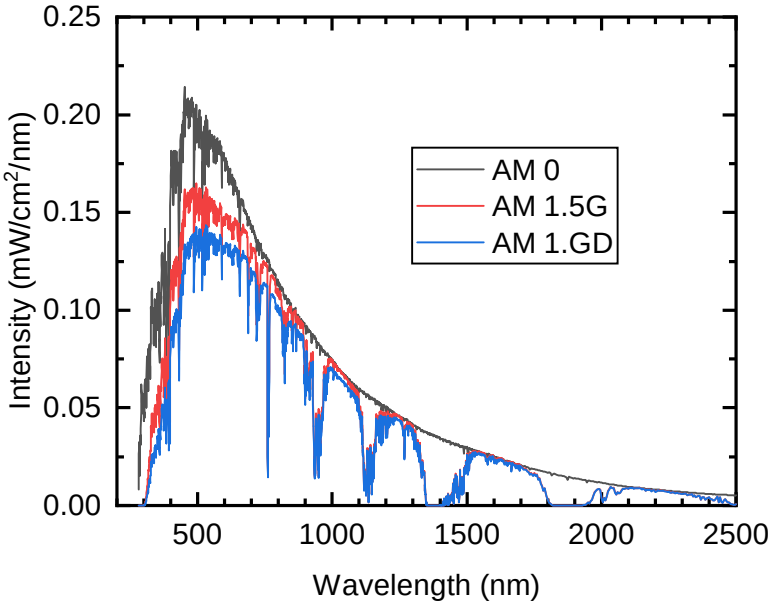

Figure 3.9: The reference spectrum of sunlight. Figure is reproduced from [66]

latitude is a matter of interest because many countries are located around this latitude. The American society for testing and materials (ASTM) defined the AM 1.5G and AM 1.5D spectrum based on average atmospheric conditions in the united states at the latitude.[66] AM 1.5G is a global intensity including the direct illumination from the sun and scatterings from surroundings, and AM 1.5D includes only the direct illumination from the sun.[66] The intensity of AM 1.5G is 100 mW/cm^2, and a potential PEC device is expected to run under this spectrum. AM 1.5D is suitable for studying a solar cell with integrating optics because the integrating optics cannot concentrate on the diffusive component of the sunlight. The spectral intensities of AM 0, AM 1.5G and AM 1.5D are depicted in Figure 3.9.[66]

In a laboratory environment, a light source which can simulate the natural light is normally used instead to acquire reproducible intensity. In this study, a Xenon lamp with AM 1.5G filter provided from Newport Corporation is used to reproduce the natural sunlight and denoted as the light source in this thesis. The xenon lamp is made of two tungsten electrodes and xenon gas encapsulated in a fused silica bulb. It produces plasma by applying a high voltage on the two electrodes and ionize Xenon gas, as described in section 3.1.2. While the ionized gas molecule recombines with electrons, the electrons emit photons whose energy depends on the orbital level of the Xenon atom. The spectrum of the light from the plasma resembles AM 1.5 spectrum except for large peaks around 800 $\sim$ 1000 nm range. To make the Xenon lamp spectrum closer to the AM 1.5G spectrum, a filter is applied to lower the peaks, as illustrated in Figure 3.10. The spectral intensity is measured by the light source provider (Newport Corporation) and double-checked by using a spectrophotometer (Ocean Optics Inc, USB4000-UV-vis) in the UV-visible light range. The lamp light power is calibrated to be 68.4 mW/cm^2 in 300nm $\sim$ 900 nm wave-

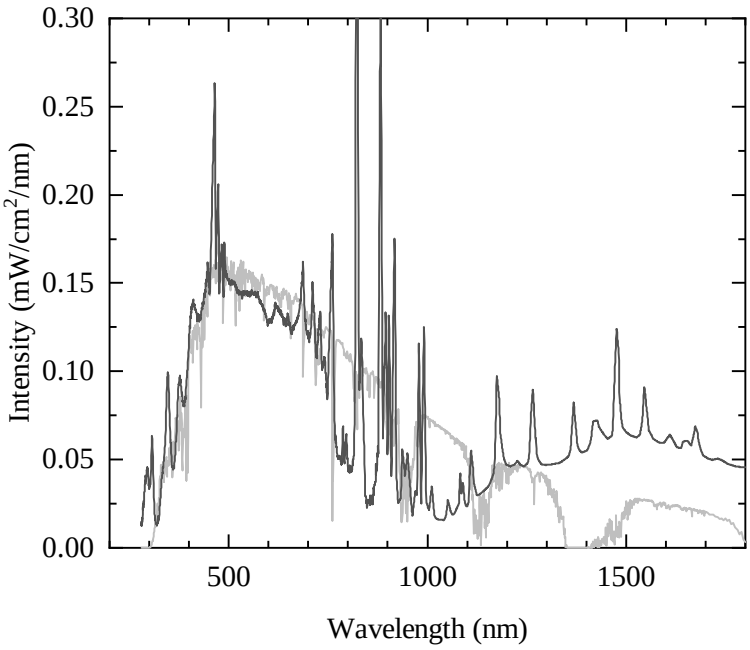

Figure 3.10: The spectrum of light source used in this study (black) compared to the reference 1.5G spectrum (grey).[66]

length range, and it will give the same intensity from the AM 1.5G spectrum in the same wavelength range.

The amount of the photocurrent is proportional to the intensity of the solar spectrum. The solar spectrum illuminating a semiconductor in a solar cell excites electrons in a valence band to a conduction band to generate a photocurrent. Assuming that a single photon excites a single electron in a semiconductor, it is possible to calculate how much charges could be produced from the spectrum. Thus, solar intensity in the unit of ”power density (mW/cm^2/nm)” can be expressed as the unit of ”photon flux (photons/cm^2/nm)” or ”current density (mA/cm^2/nm)”. When discussing the activity of solar cell depending on the solar spectrum, it would be more straightforward to use the unit of current density rather than the unit of power density.

It should be noted that the light source used in this study and the standard AM 1.5G spectrum are not identical, and the difference between the spectrum is shown in Figure 3.11 in the unit of current density. The spectrum range where the light source has higher(or lower) intensity compared to AM 1.5G spectrum is filled with red(or blue). The solid line represents the integration of the difference from the left to right. The light source used in this study has a higher intensity in the infrared range, while the intensity at the visible light range shows a relatively smaller difference. The large difference is mainly because AM 1.5G spectrum undergoes strong infrared absorption by water molecules and has lower intensity around 1400 nm.

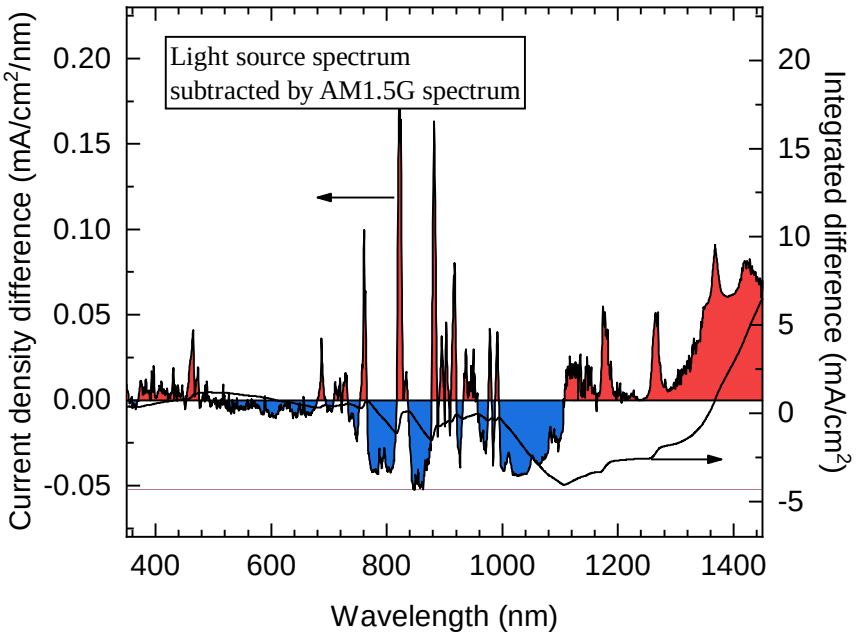

Figure 3.11: The difference between the light source and the AM 1.5G. The red and blue area represent the range where the light source is higher or lower than the AM 1.5G. The black solid line shows the integration of the difference from left to right.

3.2.2 Reflectance calculation

Conventional solar cells usually adopt mono- or multi-layer of anti-reflective coating over its optical front side to minimize loss by reflection. The working principle of the anti-reflective coating is based on a coherent optical interference inside of the layers. By choosing a suitable material and thickness of the layered structure, it is possible to design a stack of films inducing a destructive interference to reflection and a constructive interference to transmission, and it will minimize the reflection of a solar cell. The design of the anti-reflective coating requires calculation on the reflection and transmission of the layers by solving Maxwell's equation, which can be carried out by the transfer matrix method.[67] The transfer matrix method nicely condenses boundary conditions of Maxwell's equation and phase change during the propagation into simple products of 2 $\times$ 2 matrices. Each 2 $\times$ 2 matrix corresponds to one layer or one interface between the layers. When there is an optical wave propagating through a multi-layer structure in the normal direction, the relationship between the electric field before and after propagating through ith layer and the interface between ith and $i+1$th layer is described as below:

$$\begin{pmatrix} E_{i+1}^{f} \\ E_{i+1}^{b} \end{pmatrix} = M_{i}^{i+1} P_{i} \begin{pmatrix} E_{i}^{f} \\ E_{i}^{b} \end{pmatrix} \tag{3.3}$$

Here, f and b represent forward and backward propagating components, respectively. The matrix P represents the phase shift during the propagation of the ith layer.

$$P_i = \begin{pmatrix} e^{ik_i d_i} & 0 \\ 0 & e^{-ik_i d_i} \end{pmatrix} \tag{3.4}$$

Here, k_i and d_i represents the wavenumber and the thickness of the ith layer, respectively. The wavenumber is determined by the wavelength of light and the complex refractive index of materials n_i.

$$k_i = \frac{2\pi}{\lambda} n_i \tag{3.5}$$

The imaginary component of the refractive index represents the decreasing electric field by absorption. The matrix M_i^{i+1} represents the Fresnel equation derived from the boundary condition of Maxwell's equation at the interface between ith and $i+1$th layer.

$$M_i^{i+1} = \begin{pmatrix} \frac{n_i+n_{i+1}}{2n_{i+1}} & \frac{-n_i+n_{i+1}}{2n_{i+1}} \\ \frac{-n_i+n_{i+1}}{2n_{i+1}} & \frac{n_i+n_{i+1}}{2n_{i+1}} \end{pmatrix} \tag{3.6}$$

When there is N number of layers between two layers where the light is incoming and outgoing (see Figure –), the optical wave propagates through N number of layers and $N+1$ number of interfaces, and the change of electric field from incoming wave to outgoing wave can be found by multiplying $2N+1$ number of 2 $\times$ 2 matrices. Each layer and interface corresponds to P_i or M_i^{i+1} matrix in the equation 3.3. Therefore, the electric field before and after the propagation can be found by solving the equation.

$$\begin{pmatrix} E_{N+1}^f \\ 0 \end{pmatrix} = M_N^{N+1} P_N ... M_i^{i+1} P_i ... M_1^2 P_1 M_0^1 \begin{pmatrix} E_0^f \\ E_0^b \end{pmatrix} \tag{3.7}$$

The subscript 0 and $N+1$ represent two layers where the light is incoming (water or air) and outgoing (germanium substrate), respectively. It is assumed that the last outgoing layer is infinitely long that there is no reflection wave after the boundary between Nth and $N+1$th layer ($E_{N+1}^b = 0$). Thus, there are three unknown variables, E_0^f, E_0^b and E_{N+1}^f, and the reflectivity and transmissivity of the layers can be calculated by using the ratio between three variables. The major advantage of the transfer matrix method is that it can calculate the optical properties very quickly compared to other methods like finite element methods. However, this method is suitable for a one-dimensional structure (such as the stack of films) and not applicable to a complex 3D structure. In addition, this method often faces numerical error from exponential terms, which have values with very different orders of magnitude. The exponential terms with a very small value are often rounded off during computation and result in an erroneous result. This problem often becomes serious when dealing with extreme conditions such as a layer much thicker than the optical wavelength. To avoid the numerical error, it is necessary to increase the number of significant figures in the calculation sufficiently, but it may cost a computational resource.

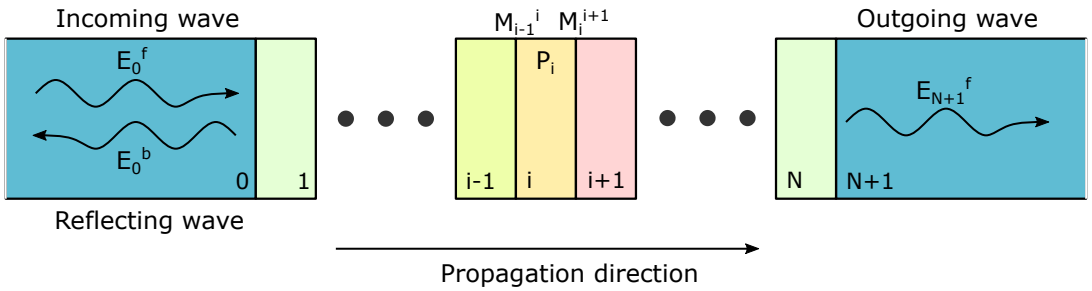

Figure 3.12: Schematic diagram showing the transfer matrix methode for reflectance calculation. Because there are three variables (E_0^f, E_0^b and E_{N+1}^f) and two equations from the transfer matrix method (equation 3.7) it is possible to acquire the ratio between the electric fields.

The multi-layer structure of the PEC device includes GaInP, GaAs, Ge and TiO_2. For EQE measurement, which will be explained later, ITO is also deposited on top of TiO_2 layer. Reflection calculation on PEC devices requires the refractive indexes of those materials. While the refractive indexes of GaInP, GaAs, Ge and TiO_2 are adopted from the references[68–71], the refractive index of ITO is measured by ellipsometry. These refractive indexes are plotted in Figure 3.13.

3.2.3 Electrochemical setup for a wired PEC device

Wired PEC devices are characterized in an electrochemical cell by collecting either electrical charge or gaseous products. Charge collection is carried out by using a three-electrode setup shown in Figure 3.14, and gaseous products can be collected by connecting eudiometers to the setup. Details about the gas collection are described in the next section (for wireless device which can be only characterized by the gas collection), and this section will focus on the charge collection from the three-electrode setup. The three-electrode setup is made of three compartments containing working, counter and reference electrodes. The working electrode is the wired PEC device with a copper wire contact on the backside. The wired PEC device is illuminated under the standard light source introduced in the previous section. The counter electrode used in this study is iridium oxide deposited on a gold mesh. The electrode is prepared by drop-casting 1 mM $IrCl_3$ on gold mesh and annealed in air 400 °C for 2 hours. During water splitting experiments, the counter electrode provides a large surface area, and OER takes place at a low overpotential ($\sim$ 1.6 V vs RHE). The red graph in Figure 3.15 shows the performance of the iridium oxide counter electrode. The reference electrode is $Hg_2/HgSO_4$ electrode, and the electrical potential on these electrodes are controlled by a potentiostat. The electrochemical cell is filled with 0.1 M $HClO_4$, and it is prepared by 70 % $HClO_4$ diluted in millipore water.

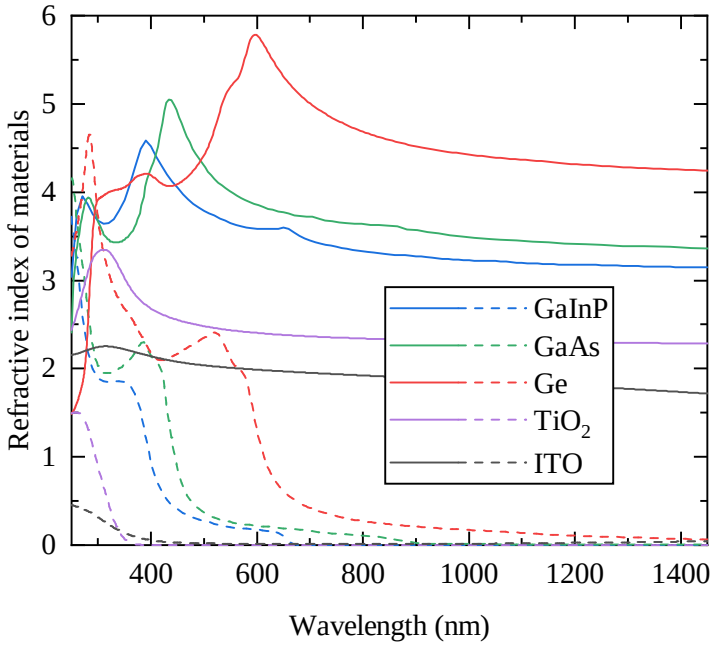

Figure 3.13: The refractive index of materials used for the calculations in this study Solid lines and dashed lines are the real and imaginary part of the refractive index, respectively.

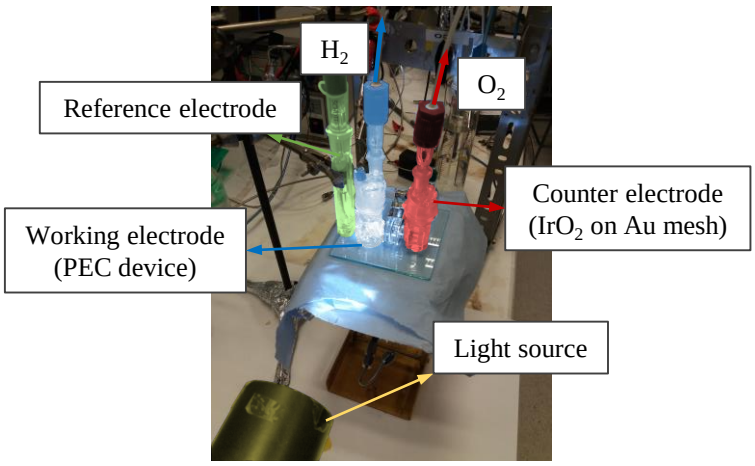

Figure 3.14: Electrochemical cell used for characterizing wired PEC devices

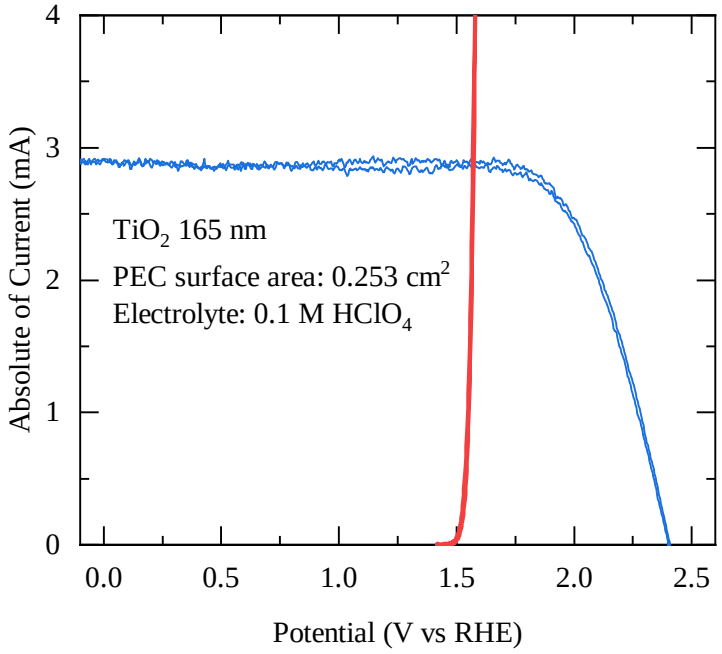

Figure 3.15: Electrochemical cell used for characterizing wired PEC devices

The activity of wired devices are measured by cyclic voltammetry. The electrical potential of the working electrode is controlled from -0.3 $\sim$ 2.6 V vs RHE with 50 mV/s of scan rate. Based on the cyclic voltammetry data, three important characteristics of a PEC device is determined: short-circuit current (I_{sc}), open-circuit photovoltage (V_{oc})and fill factor. The short circuit current density is defined to be the current density at 0 V vs RHE, while the photovoltage is defined to be the voltage when the current density is zero. The fill factor is defined by the following equation.

$$F.F. = \int_{0V\,vs\,RHE}^{photovoltage} I(V)dV/(V_{oc} \times I_{sc}) \tag{3.8}$$

The fill factor represents the ratio between the area under the cyclic voltammetry measurement and $V_{oc} \times I_{sc}$. While there are many factors affecting the fill factor, it is mainly affected by series resistance, shunt resistance and energy barrier for electrochemical reaction in this study. The typical value of the fill factor in this study is around 88 $\sim$ 90 %.

The stability of wired devices is tested by chronoamperometry at 0 V vs IrO_2. The chronoamperometry is carried out in a two-electrode setup. The working electrode is short-circuited to the counter electrode and $Hg_2/HgSO_4$ reference electrode is not involved in the measurement. The photovoltage from PEC device will load a potential difference between the surface of the PEC device and the counter electrode and it will drive a water-splitting reaction without any external energy input from outside.

The $Hg_2/HgSO_4$ reference electrode potential is calibrated in a three-electrode setup filled with hydrogen saturated electrolyte with two platinum wires as working and counter electrodes. The platinum working electrode is cleaned by applying an anodic potential (1.5 $\sim$ 1.6 V vs RHE) to oxidize contaminants, and the oxidized platinum surface is reduced at cathodic potential (0.1 $\sim$ 0.2 V vs RHE). After the cleaning, the open-circuit potential of the working electrode is measured as the reference electrode potential.

3.2.4 Gas collection for wireless PEC devices

In cases of testing wireless devices without any external electrical connection, it is not possible to characterize the device by measuring current density because there is no electrical wire connected to the device. Instead of measuring current density, the gaseous products have to be collected and quantified to test its performance of wireless devices. However, collecting the gaseous products from a wireless device requires an elaborate design of an electrochemical cell satisfying the following requirements. 1) The electrochemical cell has to be able to separate the gaseous products by a membrane, and there should not be any significant leakage or cross-over of the gaseous products. The rate of leakage (or cross-over between two compartments) should be less than 1 % of the expected amount of product, which is around 10 μl/hr of hydrogen and 5 μl/hr of oxygen. 2) Ohmic resistance from proton conduction also should be as low as possible not to hamper the activity of wireless devices. 3) While both front and backside of the solar cell are exposed to an electrolyte, the edge-side of the piece of a solar cell, where the stack of the solar cell is exposed, should not be in contact with an electrolyte to maintain high shunt resistance and prevent damage on the solar cell. 4) The thickness of the water layer between a glass window and a PEC device has to be less than 2 mm to minimize infrared absorption by water. (The requirement on the water layer thickness will be explained in the later, section 4.1) 5) Every surface in contact with an electrolyte should be stable.

Figure 3.16 shows a compression cell design satisfying the design requirements. The body of compression cells and o-rings are made of PEEK and FFKM, which are stable in acid. Two compartments are separated by the Nafion membrane and a PEC device and filled with 1 M $HClO_4$. HER takes place on the optical front side of the PEC device, while OER takes place on the other side. The thickness of the water layer is $\sim$ 1.6 mm. The proton is conducted all the way along with the red dashed line in Figure 3.16 with a certain level of ohmic loss.

The gaseous products from hydrogen and oxygen compartments are collected by eudiometers (25 ml total volume, $\sim$ 50 cm length and 50 μl graduation) as shown in Figure 3.17. Before starting the experiment, two eudiometers are connected to the hydrogen and oxygen compartments, respectively. (To avoid the overestimation by thermal expansion of gas volume by the light source, the eudiometers could be connected after 5 $\sim$ 10 min of an experiment, especially when using eudiometers with a smaller volume and graduation.) The pressure inside of the chamber is equal to atmospheric pressure, and the water level inside and outside of the eudiometer is equal to each other (Figure 3.17A). As the

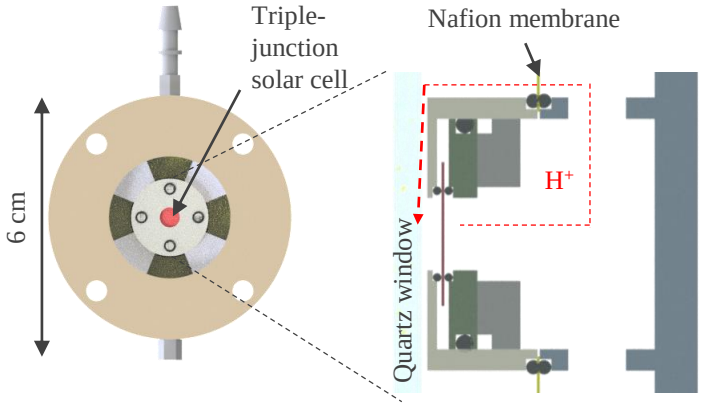

Figure 3.16: The design of the compression cell. The red dashed line shows the proton conduction path

experiment goes on, the volume of gas inside of the electrochemical cell expands, and the water level inside of the eudiometers is pushed down to a lower level (Figure 3.17B). The pressure inside of the cell is larger than the atmospheric pressure (as much as the water level difference in and outside of the eudiometer), and it would underestimate the volume of gas products. To measure the gas volume at the atmospheric pressure, the eudiometers are lifted up until the water levels inside and outside of the eudiometers become equal (Figure 3.17C).

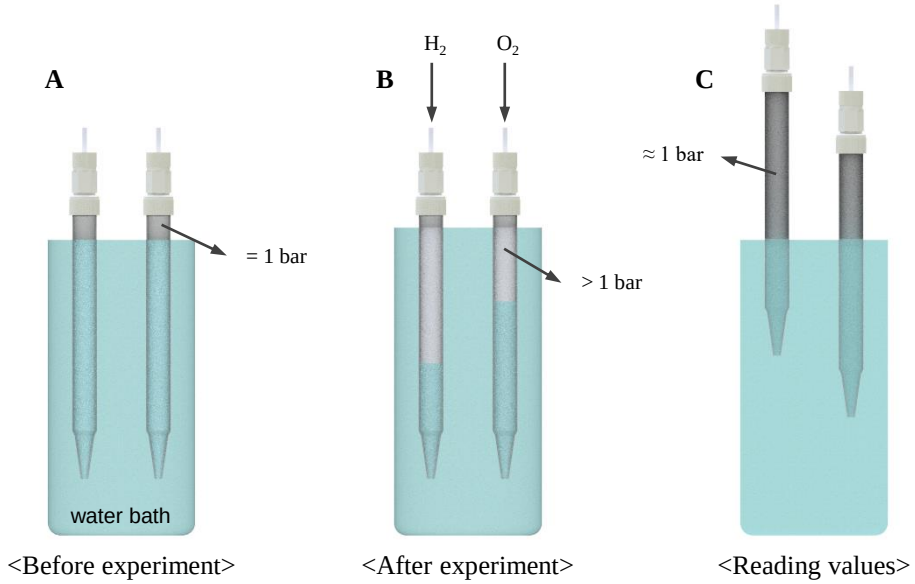

Figure 3.17: Illustration on the gas volume measurement using eudiometers. (A) Before starting the water splitting reaction, the water levels inside and outside of the eudiometers are the same. (B) After or during the measurement, the water level inside of the eudiometers is pushed down. (C) When reading the volume of the gaseous products, eudiometers are lifted up to make the pressure inside to be closed to atmospheric pressure.

As one of the design requirements of the cell is reducing the loss of product by leakage

to be less than 1 % of the expected total amount of product, a leak test on the electrochemical cell is carried out by using the eudiometers. While doing the leak test, a certain volume of air is filled into the eudiometers intentionally and left for a while to see if there is volume reduction in the eudiometers by leakage. For sensitive leak test, very thin eudiometers (1 ml total volume, $\sim$ 40 cm length and 10 μl graduation) is used to detect a tiny amount of leakage. The thin eudiometer is sensitive enough to detect the thermal expansion of gas by heat transferred from hands touching the electrochemical cell or tubings immediately. Therefore, it is necessary to wait for 3 $\sim$ 5 minutes until the setup reaches thermal equilibrium with the surrounding environment before reading the marks to see if there is a leak.

To quantify the effect of ohmic loss by the proton conduction in the cell, electrochemical impedance spectroscopy (EIS) is conducted by inserting two electrodes into the electrochemical cell. At position where the PEC device is supposed to be, titanium foil with the same size is placed as a working electrode, and the backside of Ti foil is connected to copper wire. The backside of Ti foil and copper wire is not in contact with the electrolyte by covering them with acid-stable polymers and tubes. As a counter electrode, platinum wire covered with an acid-stable tube is inserted into the oxygen evolution chamber of the compression cell. The position of the platinum wire's tip is placed nearby the backside of the Ti foil to make sure that the electrochemical impedance spectroscopy measures the proton conduction resistance along the red dashed line in Figure 3.16. The measurement shows that the resistance from the proton conduction is around 48 ohm as shown in Figure 3.16A, which is an acceptable value in this experiment.

Computational simulation based on finite element methods is also conducted to estimate ohmic loss by using COMSOL Multiphysics®. Figure 3.16B shows the volume of electrolyte inside of the cell, and the following electrostatic equation is solved in the geometry.

$$\vec{J} = -\sigma \nabla V \tag{3.9}$$

Here, σ, J and V are the conductivity, the current density vector and electric potential. For simplicity, the pH of the electrolyte is constant all over the space, and the conductivity of the electrolyte and PEM membrane is chosen to be 41.69 S/m and 10 S/m, respectively[72, 73]. Except for two surfaces where are in contact with a solar cell, all of the boundaries are having insulating boundary condition.

$$\vec{n} \cdot \vec{J} = 0 \tag{3.10}$$

Here, $\vec{n}$ represents the surface normal vector. On the two surfaces where contact with the front and backside of the PEC device, boundary conditions for influx and outflux current density are applied to simulate the photocurrent density from a solar cell.

$$\vec{n} \cdot \vec{J} = \pm 10 mA/cm^2 \tag{3.11}$$

Mesh size for solving the finite element equation is reduced until the simulation results converge. The simulation on the potential drop across the volume of electrolyte is illustrated in Figure 3.16 (c). The overpotential from ohmic loss (η_{proton}) is defined by the difference between the average potential of the front and backside of the PEC device.

$$\eta_{proton} = \frac{1}{S_a}\int_{S_a} V(x)dx - \frac{1}{S_c}\int_{S_a} V(x)dx \tag{3.12}$$

Here, S_a and S_c are the surface area of the cathode and anode, respectively. Therefore, the ohmic resistance in the cell is defined as below.

$$R_{proton} = \frac{\eta_{proton}}{S_c \times 10mA/cm^2} \tag{3.13}$$

The simulation shows that the resistance from proton conduction is 35 ohm, which is similar to the experimentally measured value. According to the simulation, about 60 % of the resistance is attributed to the shallow channel of the water layer in front of the solar cell.

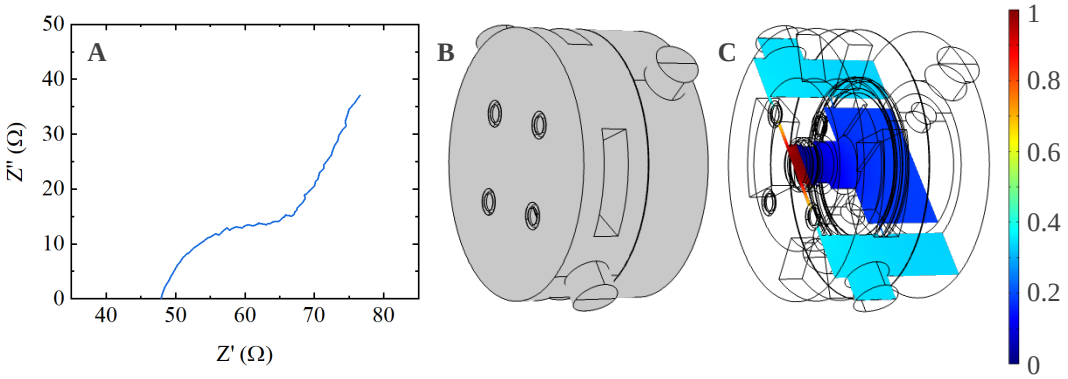

Figure 3.18: Ohmic resistance inside of the compression cell. (A) EIS measurement shows 48 ohm, and (B,C) FEM simulation shows 35 ohm.

As discussed in section 2.4.3, scaling up of PEC device as a practical hydrogen production could encounter a problem by having massive ohmic loss from the proton conduction. Although scaling up of a PEC device is not a significant subject to be investigated in this thesis, the adverse effect of scaling up is discussed by using the FEM simulation on the compression cell design. To estimate the change in the ohmic resistance and the voltage drop, the same FEM simulation is carried out by scaling the cell's geometry in the planar direction of the solar cell, which would result in a larger reaction area and longer proton transfer distance. The simulation result on the resistance and voltage drop depending on the length scaling are shown in Figure 3.19. The ohmic resistance in the cell design in compression cell design is mostly originated from a shallow water layer in front of the device, and it becomes more dominant on a larger scale. When considering the geometry of water volume depicted in Figure 3.18B, the resistance from the shallow water gap can

be approximated as an electrical resistance from an inner ring to the outer ring of a disk, which can be expressed as the following equation.

$$R = \frac{\sigma}{2\pi t} ln\left(\frac{r_{outer}}{r_{inner}}\right) \tag{3.14}$$

The following equation is the averaged resistance over the surface of the solar cell would be close to the contribution from the shallow water layer on the ohmic resistance.

$$\begin{aligned} R_{watergap} &= \int_0^{r_c} \frac{\sigma}{2\pi t} ln\left(\frac{r_{holder}}{r}\right) 2\pi r dr / \int_0^{r_c} 2\pi r dr \\ &= 23.4\Omega \end{aligned} \tag{3.15}$$

Here, r_c is the radius of the cathode (2.5 mm, equals to r_a), and r_{holder} is the radius of the sample holder (19 mm). t is the thickness of the shallow water gap, which is around 0.3 $\sim$ 0.6 mm depending on o-ring compression. Please note that $R_{watergap}$ is independent of the scaling of the geometry in the planar direction. On the other hand, the resistance from the other part of the cell gets smaller as the scale gets larger. Therefore, the resistance from the shallow water gap becomes dominant, and the total proton conduction resistance converges to 23.4 Ω, as shown in Figure 3.19A. Although the ohmic resistance decreases slowly as the geometry scales up, the total current increases proportionally to the square of the scale factor (current density multiplied by the surface area) and thus, scaling the geometry increases ohmic voltage drop. For example, when the geometry is scaled to be five times larger in the planar direction, the ohmic voltage drop in the cell would be 1.75 V as shown in Figure 3.19B. These simple calculation and simulation implies that scaling up of a PEC device would face an ohmic loss issue.

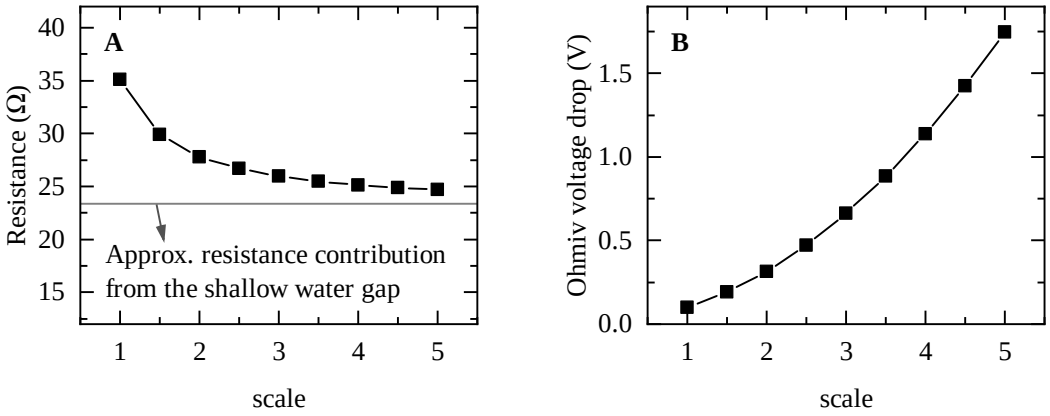

Figure 3.19: FEM study on ohmic resistance and voltage drop in the electrochemical cell scaled-up in the planar direction.

3.2.5 SEM and EDS

The change in the surface morphology before and after the experiment or the cross-section of PEC devices are observed by scanning electron microscopy (SEM) and energy-

dispersive X-ray spectroscopy (EDS). High energy electrons impinging on the surface of the sample interact with atoms and release various signals containing information on surface topology or composition. The high energy electron beam generation and signal analysis are carried out by using Quanta FEG 250 provided by FEI Company.

The electron beam is generated from an electron gun, which is usually based on thermionic emission or field emission. In the case of a thermionic emission gun, a piece of metal is heated up to supply thermal energy to electrons in the metal. The electrons will escape from the metal when they acquire thermal energy large enough to overcome the work function of a metal. In regards to field emission guns, an electrostatic field is applied to supply energy to overcome the work function. The SEM used in this study uses field emission gun.

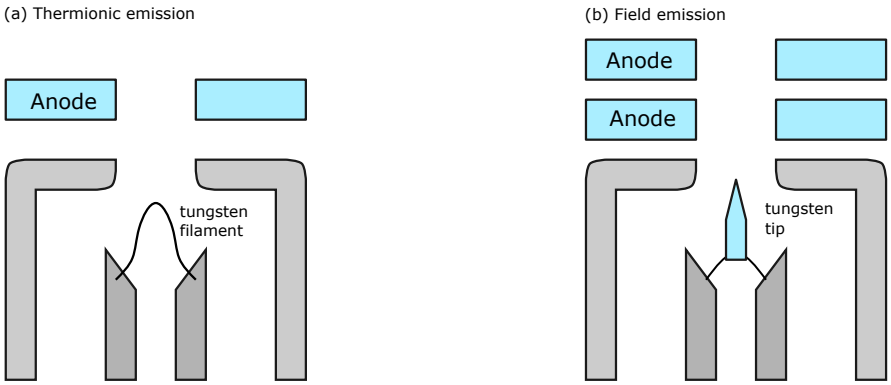

Figure 3.20: A schematic diagram of two different type of electron gun.

When a primary electron beam is focused on a particular point of a sample surface, its high energy can ionize atoms in a small area where the beam is focused. The secondary electrons released during the ionization process can be detected by an electron detector. The number of secondary electrons escaping the surface depends on surface geometry, as shown in Figure3.21.

While the SEM detects secondary electrons, EDS detects X-ray for analysis. The atoms on the surface ionized by the focused electron beam are relaxed by electron transition from high energy level to lower energy level. Because each element has its unique orbital, the electron transition process emits a characteristic X-ray containing information on the elemental composition of a sample. EDS detects X-ray from the sample for mapping the distribution of elements over the surface.

3.2.6 XPS

In the case of XPS, X-ray is used to ionize the atoms (instead of the primary electron in SEM), and analyze the kinetic energy of electrons escaping from the surface. When the energy of an X-ray photon is higher than the binding energy of an electron, it will make the electron escape with a certain kinetic energy, which can be described by the following

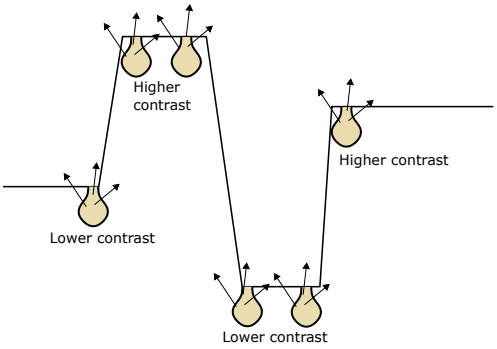

Figure 3.21: Schematic illustration for explaining color contrast in SEM image.

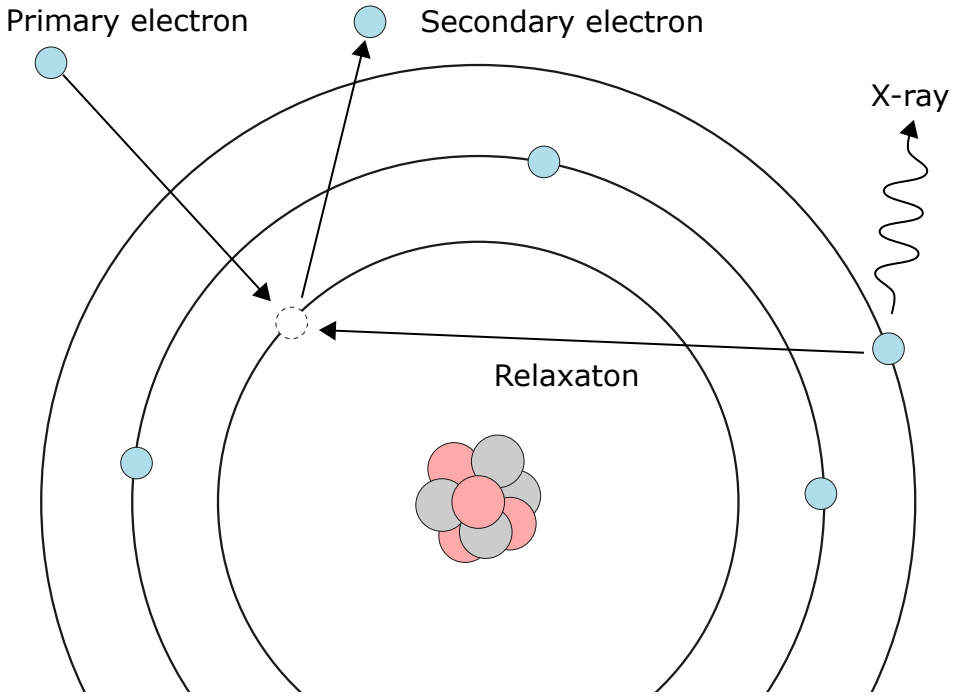

Figure 3.22: Illustration on secondary electron and X-ray generation during ionization and relaxation process.

equation.

$$E_k = h\nu - E_b - \Phi \tag{3.16}$$

Here, E_k, E_b, $h\nu$ and Φ are the kinetic energy of an electron, binding energy of an electron, energy of a photon and the work function of electron detector. Because each element has its own characteristic energy level, the kinetic energy of electrons provides the elemental composition of a sample. One of the major advantages of XPS is that it is an extremely surface-sensitive technique that can analyze the elemental composition of the surface. The surface sensitivity originates from the mean free path of electrons in a solid. The energy of an X-ray photon is typically around 1500 eV, thus the kinetic energy of electrons would be lower than that. In this kinetic energy range, the mean free path of electrons inside of solids is around 1 $\sim$ 2 nm. Thus, the electrons excited by XPS are not able to escape from a sample unless it comes from the vicinity of the surface. Therefore, XPS measurement provides information on the 1 $\sim$ 2 nm of the depth of a sample. The XPS used in this study is a ThetaProbe Instrument produced by Thermo Scientific. The X-ray source is made of Al$_{K\alpha}$, whose energy is 1486.7 eV.

CHAPTER 4

Improving the efficiency of the PEC device based on the triple-junction solar cell

There have been efforts to improve the efficiency of PEC devices, which is affected by many factors. However, the state-of-art PEC device with the highest efficiency shows the lower activity (19 %) compared to theoretical maximum expected from the solar cell used in their study (23 %)[74], as explained in the previous section 2.4.2. The major reason for the discrepancy between the theoretical maximum and experimental results is from optical loss. Unlike conventional solar cells, there are only a limited number of studies on anti-reflection coating for PEC devices.

In this chapter, optical losses in the PEC device based on the triple-junction solar cell will be investigated. This chapter will start from how the water layer in front of the PEC device affects the device performance by absorption and also discuss how the thickness of TiO_2 protection layer changes the reflection and activity of the device. In the course of the characterization, the current density generated from each junction, which is valuable information for optimizing the solar cell, will be investigated by both measurements and calculation.

4.1 The effect water layer thickness in front of the PEC device

Because a PEC device is expected to operate in an electrolyte, the absorption by water at the visible-infrared light range could affect the device performance (unless the PEC device is in the inverted-wired configuration (Fig 2.8B) whose optical front side is contacting TCO while the backside is contacting an electrolyte).[75] The light absorption by water molecules is induced by intra/intermolecular vibration modes, especially in the infrared range.[76, 77] Figure 4.1 shows the absorption coefficient of the water.[78] Please note that the y-axis is in log-scale and the absorption coefficient is much larger at the infrared range compared to that in the visible light range. In the infrared range, the absorption coefficient is larger than 1 cm^{-1}, which means that only 1 cm of water layer absorbs more than 37 % of intensity. Therefore, a water layer in front of the PEC could compromise device performance by absorbing a portion of the infrared light (based on the thickness of

this water layer) before it reaches the PEC. In the case of using a solar cell designed to operate at the infrared range, the infrared absorption by the water layer could deteriorate the device performance significantly.

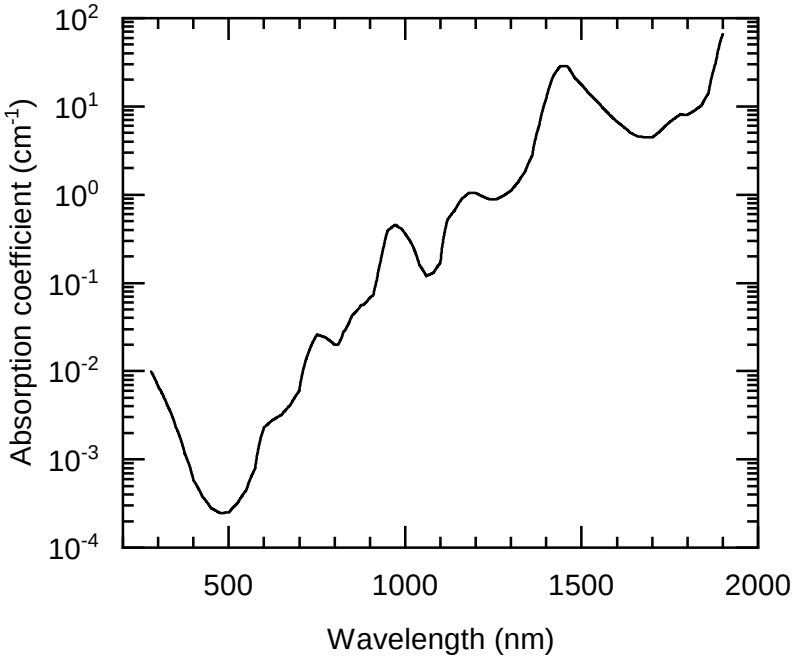

Figure 4.1: The absorption coefficient of water.[78] The absorption coefficient at the infrared range is much higher than that of the visible light range due to inter or intra molecular interactions

The triple-junction solar cell used in this study includes GaInP top junction, GaAs middle junction and Ge bottom junction. The bandgap of Ge bottom junction is 0.7 eV and expected to absorb the infrared light whose wavelength is longer than 1000 nm. When considering the large infrared absorption by water, the bottom junction in the PEC device should be affected by the water layer. To see the effect of the infrared absorption, the PEC device performance is measured with various water layer thickness and shown in Figure 4.2. The water layer thickness is controlled to be 2$\pm$ 0.5, 4$\pm$ 0.5, or 8$\pm$ 0.5 mm, and the current density at the higher potential range ($\sim$ 1.5 V vs RHE) decreases as the water layer thickness increases while the current density and the lower potential range ($\sim$ 0 V vs RHE) remains the same. The fill factor of the J-V curve measured at 2, 4 and 8 mm are 88, 82 and 71 %, respectively. To prove that the change of J-V characteristics is originated from the lack of infrared light by absorption, the additional intensity in the infrared range is supplied to the PEC device, which is prepared by using a halogen lamp filtered with a double-side polished silicon wafer. Because the bandgap of the silicon wafer is 1.1 eV, the additional light source can illuminate the light with a wavelength longer than 1000 nm, which can increase the photocurrent density from the Ge bottom junction only. As shown

in Figure 4.2, the additional light source provided to the PEC device with 8 mm of water layer recovers the lost current density at the higher potential range ($\sim$ 1.7 V vs RHE) and the fill factor. These measurements show that such changes in the J-V measurement are from the lack of infrared intensity due to the absorption by the water layer.

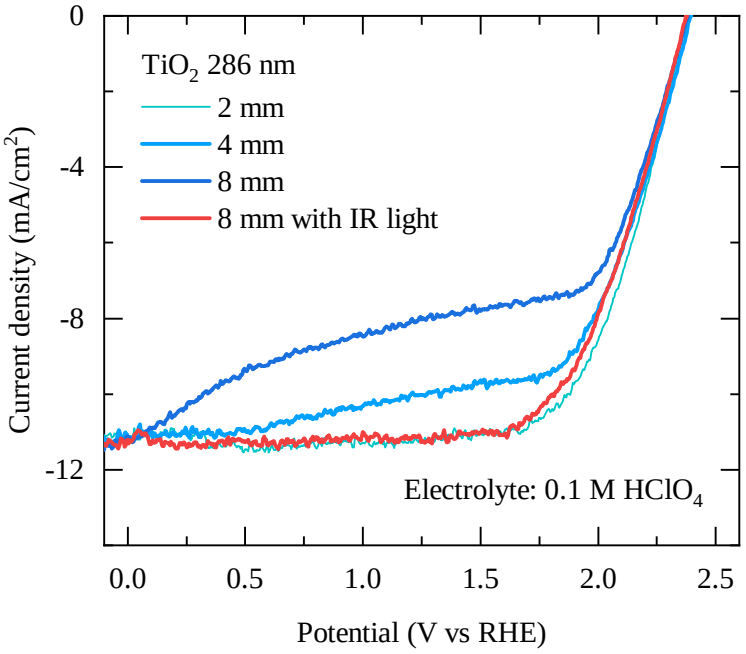

Figure 4.2: The effect of water layer thickness on the performance of the PEC device.

The change in the cyclic voltammetry measurement by the water layer thickness can be explained by two factors, 1) a low current density from the Ge bottom junction due to lack of the infrared intensity, 2) the diode behavior of the Ge bottom junction in the breakdown regime.[79–81] At the higher potential range ($\sim$ 1.5 V vs RHE), the infrared absorption by the water layer decreases photocurrent from the Ge bottom junction and limits the total current density from the system, because the current density from a multi-junction solar cell is limited by one of the junctions with the lowest current density. The excess amount of the current density from the top and middle junctions will be lost by recombination and photoluminescence. At the low potential range ($\sim$ 0 V vs RHE), the Ge bottom junction does not limit the current density because the breakdown of the Ge junction takes place. Figure 4.3 shows the equivalent circuit diagram for the triple-junction solar cell. It should be noted that the photovoltages from the top and middle junctions are applied on the bottom junction diode in the reverse direction, while the external bias from the potentiostat is in the forward direction in this PEC experiment. Thus, total electrical bias applied on the Ge bottom junction is the sum of photovoltages from the top and middle junction, and external electrical bias. When the external bias in the forward direction is small, the total bias applied on the Ge bottom junction is in the reverse direction, and it

is large enough to cause the breakdown of the Ge diode. When the breakdown of the Ge diode takes place, the current density of the solar cell is not limited by the Ge bottom junction even if the Ge bottom junction is generating a smaller amount of photocurrent density compared to the other junctions. The breakdown of Ge diode occurs in the low potential range ($\sim$ 0 V vs RHE), and the total current density is limited by either top or middle junction. At the higher potential regime ($\sim$ 1.5 V vs RHE), the external bias in the forward direction cancels out the photovoltages in the reverse direction. Thus, the breakdown of the Ge bottom junction does not take place, and the total current density of the device is limited by the Ge bottom junction.

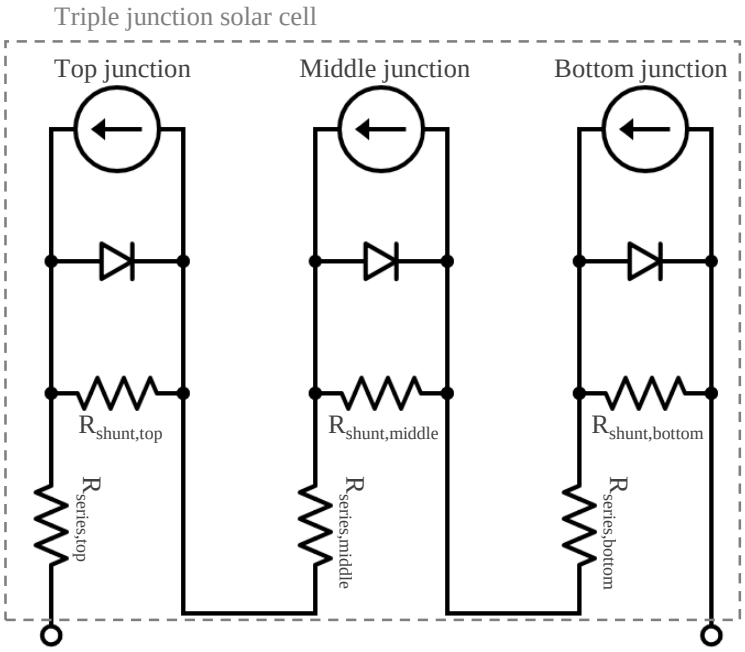

Figure 4.3: The equivalent circuit diagram for the triple junction solar cell.

4.2 Characterization of sub-cell current densities of a PEC device based on multi-junction solar cell

To get a better understanding on the performance of the device, it is important to figure out which junction is limiting the current density, and if possible, it would be nice to figure out how much photocurrent density is generated from each junction. In this PEC device made of the triple-junction solar cell, we can realize that the Ge bottom junction is not the current limiting junction based on the experiments with the controlled water layer thickness in the previous section. As shown in Figure 4.2, the PEC device with a current limiting bottom junction shows a unique shape of the J-V curve with a low fill factor. However, the PEC device measured with water layer thickness thinner than 2 mm does not shows the unique J-V curve, therefore, the current limiting junction should be either GaInP top

junction or GaAs middle junction. In this section, the methods and results for investigating the current density from the top and middle junction will be introduced.

4.2.1 Experimental setup with additional light sources

Each junction in the solar cell absorbs a different part of the light spectrum and generates current density, and the total current density of a PEC device is limited by one of the junctions with the lowest current density. Therefore, it is expected that increasing spectral intensity corresponding to the current limiting junction will increase the current density of the PEC device. Therefore, it is possible to figure out the current limiting junction by adding additional light sources for the top or middle junction to the measurement setup. The spectrum range where each junction is working can be found by the quantum efficiency measurement from the solar cell supplier (refer back to Figure 3.1 in section3.1.1), and the additional light source with the corresponding spectrum is prepared by an additional Xenon lamp with optical filters. The spectrum of the additional light sources is shown in Figure 4.4. For activating the top junction only, the filter transparent from 400 $\sim$ 500 nm is applied and denoted as the blue light. For activating the middle junction only, the filter transparent from 650 $\sim$ 900 nm is applied and denoted as the red light.

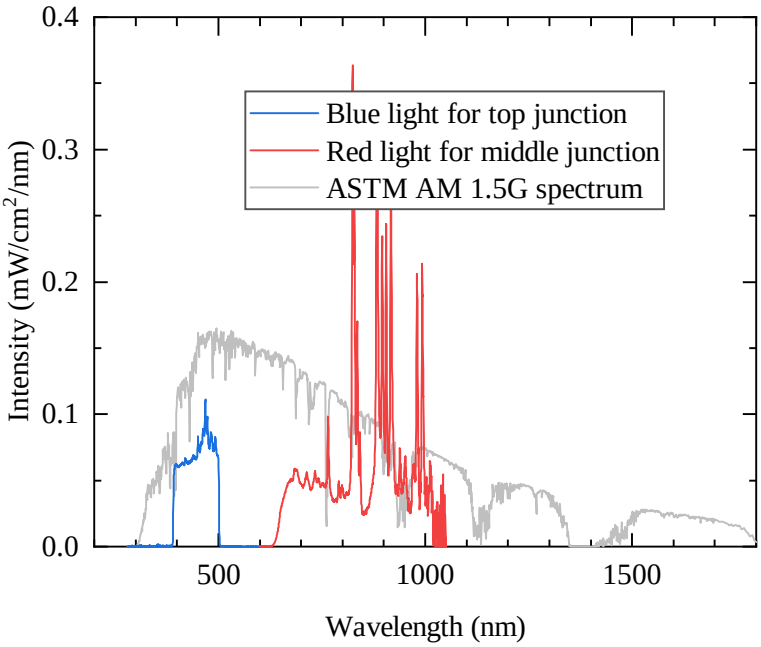

Figure 4.4: The spectrum of the additional light sources used to figure out the current limiting junction.

4.2.2 Confirmation of the current limiting junction with the additional light sources

The PEC device studied in this study is covered with TiO_2 protection layer. In principle, the thickness of the TiO_2 protection layer can affect the reflection and the performance of

the PEC devices. The PEC device with various TiO_2 thickness are prepared and tested under the standard light source (Xenon lamp with AM 1.5G filter, Figure 3.10) with or without the additional light source (Figure 4.4) and they are shown in Figure 4.5. The black lines show the photocurrent density without any additional light sources, which are around $11 \sim 12$ mA/cm^2. The blue and red lines show the results with the additional blue and red light on top of the standard light source, and the additional light sources are turned on and off during illumination. For all of the PEC devices, the current density increased when the additional blue light is supplied and did not show any response under the additional red light. Such an exclusive response to the blue light shows that the GaInP top junction is limiting the current density of the PEC devices. The relatively lower current density from the top junction is related to the design of the solar cell from the supplier. The solar cell is designed to operate in extraterrestrial space where the intensity of sunlight is closer to AM 0. However, the standard light source used in this study is trying to simulate AM 1.5G spectrum, which is having around 20 % lower intensity at the top junction spectrum range ($300 \sim 500$ nm) as shown in Figure 3.9 (refer back to section3.2.1). Because of the poor current matching in AM 1.5G spectrum, PEC devices studied in this study shows the current limitation by the top junction.

It is interesting to notice that the current density under the blue light is different between the PEC devices shown in Figure 4.5. For example, the current density from PEC device with 165 nm and 220 nm of protection layer under the additional blue light are 11.8 mA/cm^2 and 13.2 mA/cm^2, respectively. The 220 nm device is having a larger photocurrent under the additional blue light compared to that of the 165 nm device, while the photocurrent without the additional blue lights is similar to each other. The different current density under the additional blue light is not originated from the blue light intensity because changing the intensity does not change the current density increment, as shown in Figure 4.6. The current density from the PEC device with 286 nm of TiO_2 protection layer is measured under the blue light with different intensity of the additional blue light. Two different power inputs, 800 W and 1000 W, are supplied to the power source to control the intensity, and there is no clear difference depending on the blue light intensity, as shown in Figure 4.6. This result also implies that there is not significant photoluminescence coupling effect (which will be explained later in section 4.3.2)

The factor determining the current density under the additional blue light would be related to the other junction limiting the current density. As the top junction is sufficiently saturated, the photocurrent density would be limited by the GaAs middle junction or Ge bottom junction. Here, we can exclude a Ge bottom junction because the J-V curve under the blue light does not shows the characteristic shape when having the current limiting bottom junction. Then the current under the blue light would be limited by the middle junction. In the following section, further details about the current density from the middle junction will be explained.

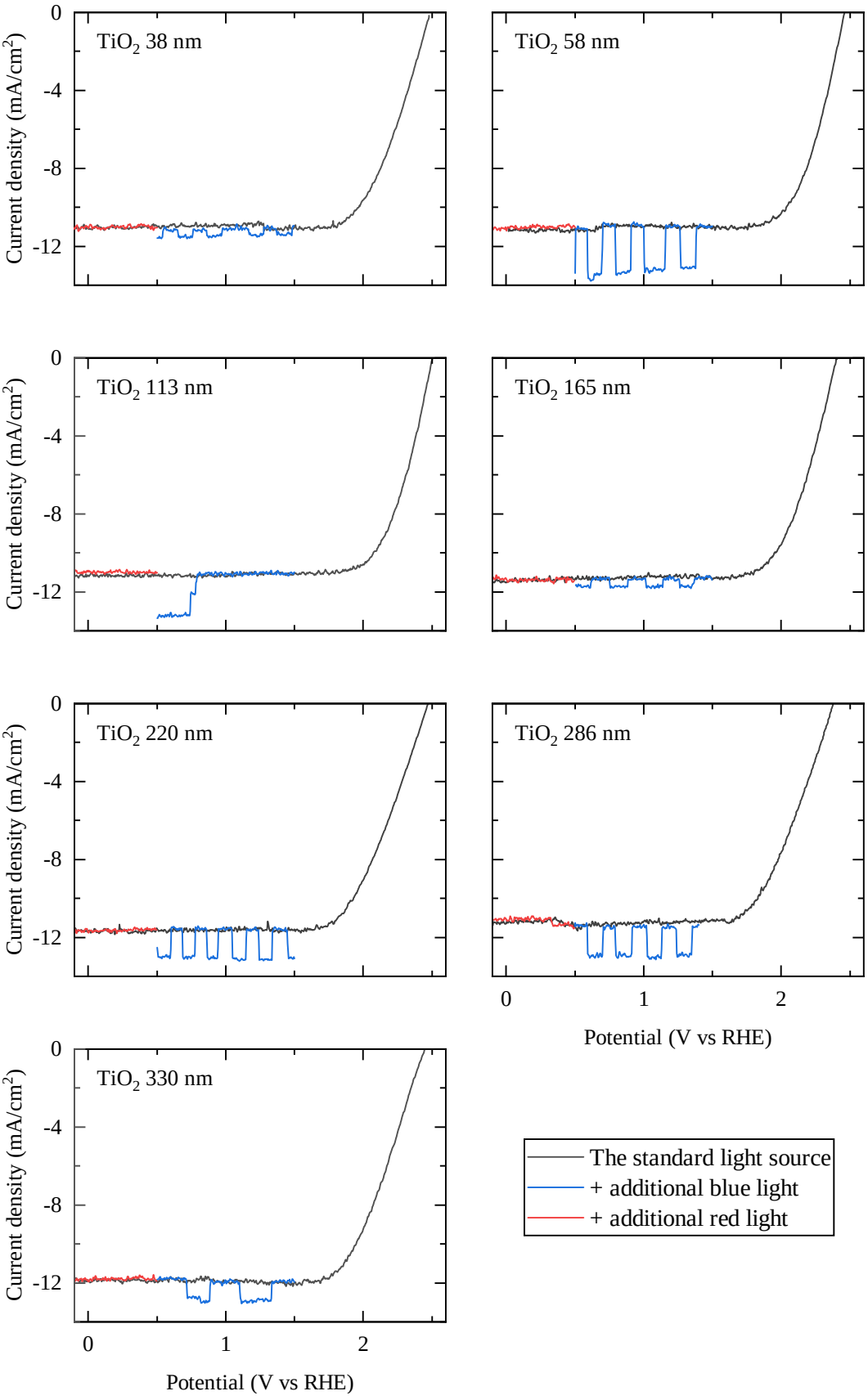

Figure 4.5: The performance of the PEC devices measured with the additional blue or red light sources

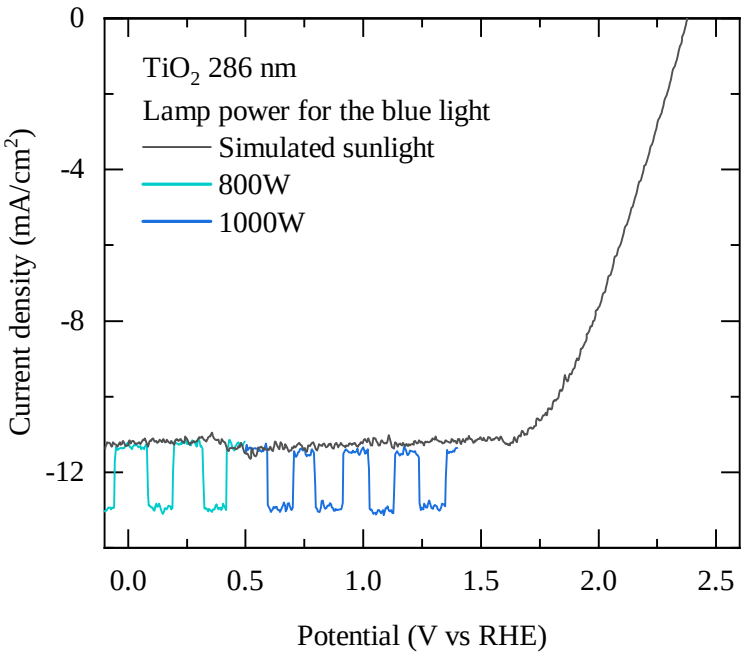

Figure 4.6: The photocurrent density by under the additional blue light. The photocurrent density does not depend on the blue light intensity.

4.3 The relationship between the reflection and subcell current densities

The experiments combined with the additional light sources shown in the previous section let us know the current limiting junction of the device and measure the current density from the top and middle junction. To figure out major factors affecting the current density from each junction, a theoretical calculation is carried out by using the spectrum of the light source, internal quantum efficiency, the reflectance of a device, and the absorption by water. While the spectrum of the standard light source and the absorption by water is introduced in Figure 3.10 and 4.1, the reflection and internal quantum efficiency of the PEC device have not been introduced yet. In the following sections, the reflection and quantum efficiency measurements on the PEC device and the current density calculation will be presented.

4.3.1 The reflection of the PEC device

It is expected that the current density under the additional blue light is limited by the current density from the middle junction and affected by reflection. Thus, the reflection of PEC devices with the seven different TiO_2 protection layer thicknesses presented in Figure 4.5 are measured and compared with calculated reflection, as shown in Figure 4.7. The dashed lines show the measured reflection between 450 $\sim$ 900 nm, while the solid lines show the calculated reflection using the transfer matrix method introduced in section 3.2.2. The change in the reflection over the wavelength is from the interference of

light inside of the stack of films. In the 250 $\sim$ 850 range, the reflectance is mostly affected by TiO_2 thickness. As the thickness increases, the number of possible interference mode increases (which means that, e.g., the number of wavelengths that can occur constructive/destructive interference increases), and it results in a larger number of maximum and minimum in the reflectance spectrum. Several sharp peaks around 850 $\sim$ 1000 nm are mostly from Bragg reflector buried inside of the III-V solar cell for reusing photons.

Based on the reflection, it is possible to explain the different current density under the additional blue light shown in Figure 4.5. When considering PEC devices with 165 and 220 nm of TiO_2 protection layer as representative examples, the reflection of the 165 nm device is higher than that of the 220 nm device at the spectrum range 650 $\sim$ 850 nm where the middle junction is absorbing. Due to the higher reflection at the middle junction range, a lower current density form the middle junction is expected from 165 nm device compared to 220 nm device, which is in agreement with the experimental result shown in Figure 4.5.

The information from the cyclic voltammetry with the additional blue light and reflection measurement gives a guideline for optimizing TiO_2 protection layer thickness for optimizing the activity of the PEC device. As discussed in section 4.2.2, the PEC device generally lacks the current density from the GaInP top junction. Therefore, it is important to reduce the reflection in the top junction spectrum range by controlling TiO_2 thickness. However, it should be noted that the current density from the middle junction changes as shown by the experiment with the blue light and having too much reflection in the middle junction range should be avoided.

4.3.2 The quantum efficiency of the PEC device

Although the change in the reflection explains the current density under the blue light qualitatively, it would be a great help for PEC device optimization if it is possible to calculate the photocurrent density from each junction and quantify the correlation between the reflection and the photocurrent density. For the photocurrent density calculation, the internal quantum efficiency of the PEC devices is necessary. The internal quantum efficiency of PEC devices can be derived from the external quantum efficiency and the reflection of the PEC device by the following equation.

$$IQE(\lambda) = EQE(\lambda)/(1 - R(\lambda)) \tag{4.1}$$

Here, $R(\lambda)$ represents the reflection of the device at the wavelength of λ. The external quantum efficiency of a solar cell is measured by collecting photocurrent under a monochromator light with two bias light sources. Because the monochromator light can excite only one of the junctions in the triple-junction solar cell, an additional light bias for the other two junctions, which are not measured by the monochromator, has to be applied to make the photocurrent flow through the triple junction device. For example, Figure 4.8 shows the moment when measuring the external quantum efficiency of the bottom junction of the PEC device. While the setup is measuring the EQE of the bottom junction by

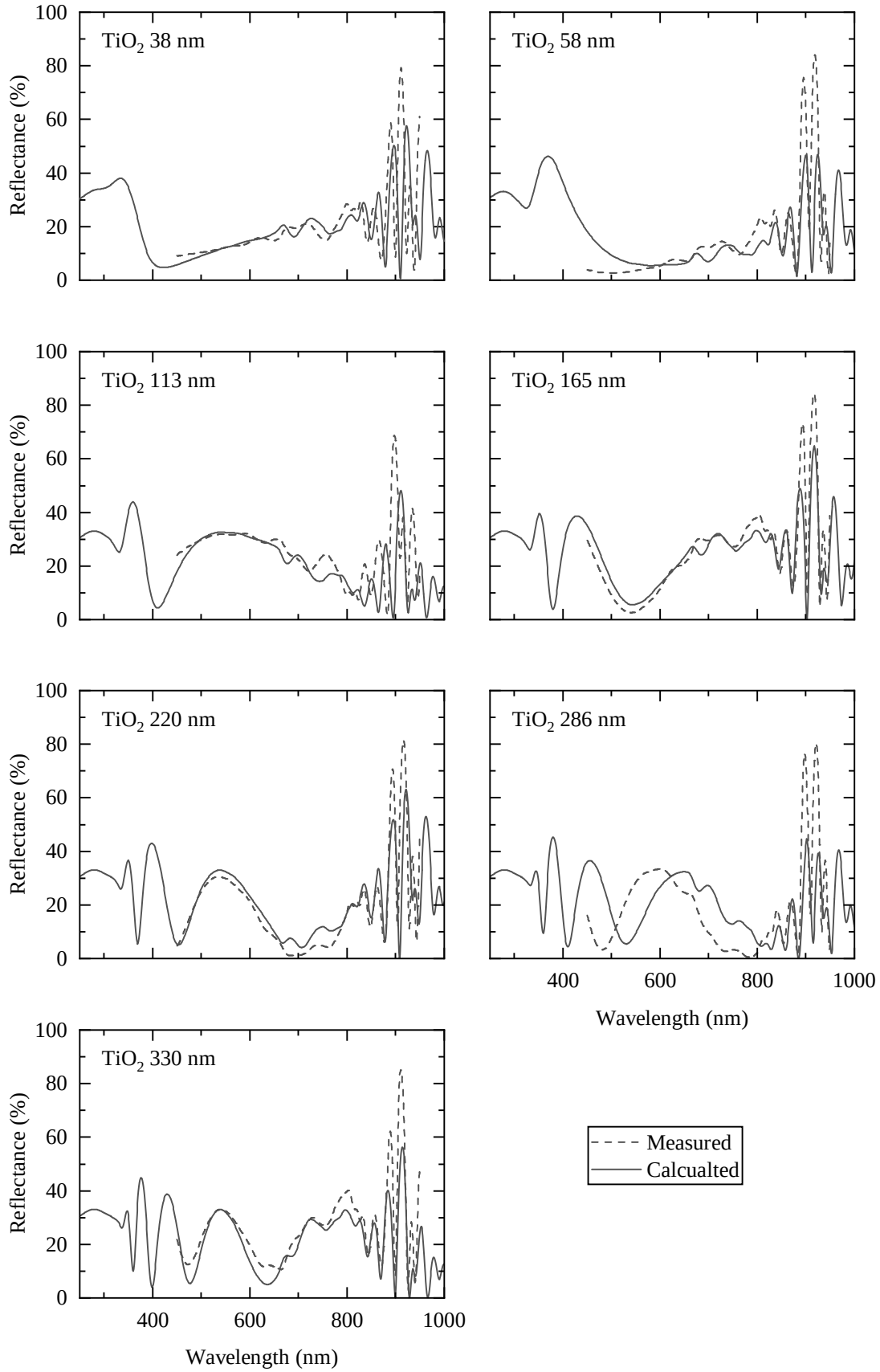

Figure 4.7: The reflection of the PEC devices with 7 different TiO_2 protection layer thicknesses. The solid and dashed lines are calculated and measured results, respectively.

using a monochromator, the external bias light for the top and middle junction (which are shown in blue and red illumination in Figure 4.8) illuminates the PEC device. To collect the photocurrent from the device, indium tin oxide (ITO) is coated over the TiO_2 protection layer as an electrical contact instead of the Pt catalyst. ITO layer is in contact with a metallic pin covered with a conducting rubber to prevent damage to the PEC device. The backside of the PEC device (Ge substrate) is covered with gold and in contact with the conducting stage.

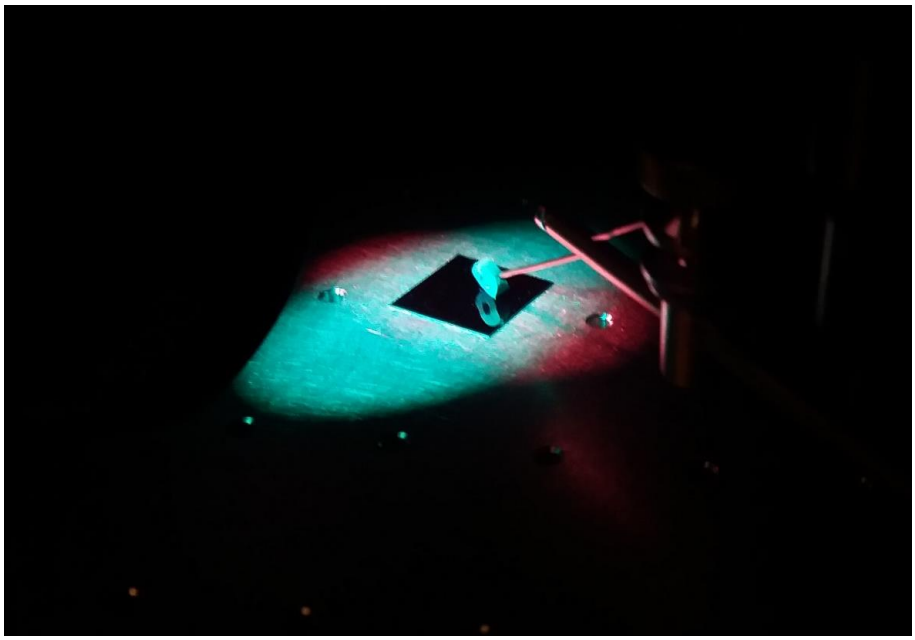

Figure 4.8: The photo of the PEC device under measurement for external quantum efficiency. The photo is taken when measuring the EQE of the bottom junction. The PEC device is illuminated with three light sources: monochromator (invisible in this photo), the external light bias for the top (blue) and middle (red) junction.

It should be noted that there could be a measurement artifact in the EQE measurement for the Ge bottom junction. As shown in Figure 4.9, the Ge bottom junction shows 5 $\sim$ 10 % of external quantum efficiency response at the middle junction range (800 $\sim$ 900 nm), but this is an unexpected signal. This artifact could be originated from 1) the breakdown of the Ge diode[79–81], 2)photoluminescence coupling effect[68] or 3) low shunt resistance in Ge junction.

As explained in the previous section 4.1, the breakdown of the Ge diode could occur because the photovoltages from the top and the middle junction is applied on the Ge bottom junction in the reverse direction. The photovoltages from the top and middle junction would be around 2 V and applied to Ge bottom junction in the reverse direction and the photovoltage is large enough to invoke the breakdown of the Ge bottom junction. To compensate the photovoltages from the top and middle junction, external electrical bias has to be applied in the forward direction of the Ge p-n junction to avoid the breakdown. Figure 4.9A shows the EQE of the bottom junction depending on the external bias. When

the external bias is zero or very low, EQE responses at the top or middle junction range because the current density of the sample is not limited by the Ge bottom junction due to the breakdown. As the external bias increases from 1.8 V to 2 V, the breakdown does not occur and the measurement artifact decreases. When the external bias is higher than 2 V, it works as a potential energy barrier that stops the current flow and decreases EQE of the bottom junction. Thus, around 2 V of external bias is appropriate for EQE measurement.

The bias light intensity also needs to be adequately adjusted to avoid the photoluminescence coupling effect, especially when measuring EQE of the bottom junction. When measuring the EQE of the bottom junction, bias lights for the top and middle junction are applied, but their intensity is usually higher than the monochromator in the infrared range. The application of these bias light results in a smaller amount of photocurrent density produced by the Ge bottom junction compared to the other junctions. This mismatch in the current densities among the junctions means that the current density which should be transferred from the middle junction to the bottom junction, cannot be transferred to the bottom junction but recombines and emits photoluminescence. The photoluminescence can be absorbed again by the Ge bottom junction, and it makes Ge bottom junction current density is affected by the photons for the middle junction. Therefore, EQE of the bottom junction shows a response by the monochromator light in the middle junction range. Figure 4.9B shows EQE measurement with 2 V of external bias and the measurement artifact is created by the strong intensity of the middle junction bias light. When the bias light for the middle junction is high, the middle junction is over-flooded and generates photoluminescence to show the EQE response of the bottom junction in the spectrum range for the middle junction. The measurement artifact decreases as the intensity of the bias light for the middle junction decreases, as shown in Figure 4.9B. A similar measurement artifact could occur from a strong bias on the top junction, which shows a large signal in the top junction range. Therefore, measuring the EQE of the device without the artifact requires a moderate balance between the electrical bias and optical bias lights.

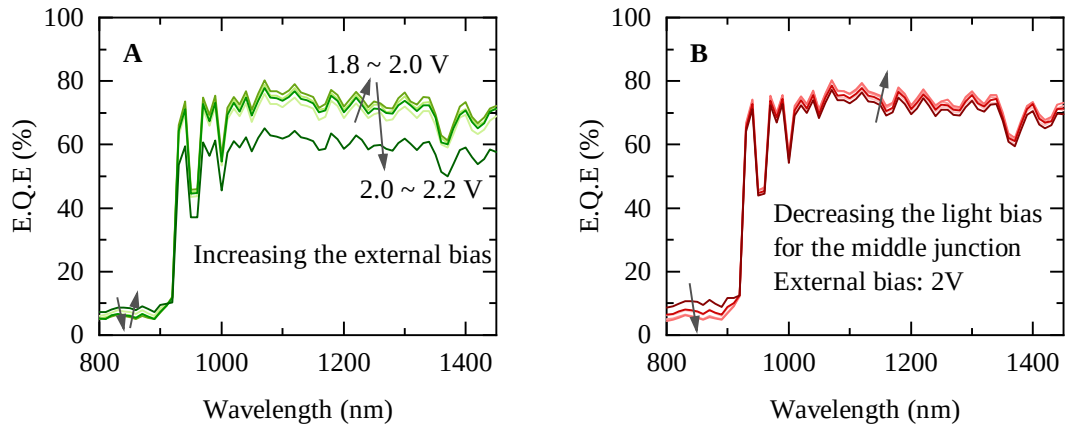

Figure 4.9: EQE measurement on the bottom junction with (A) different external bias and (B) different intensity of bias light for the middle junction.

To minimize the measurement artifact, especially for the Ge bottom junction, the external electrical bias and the intensity of optical bias should be adjusted to a proper level. The adjustment for EQE measurements is carried out by following the procedure introduced in the reference.[82] The procedure is repeated three times for measuring the EQE of each junction, and each procedure cycles the following steps: 1-1) EQE of the junction to be measured. To carry out the procedure quickly, only one wavelength point is measured. 1-2) and control the electrical bias and optical bias to maximize the signal and 2) EQE measurements on the junctions not to be measured, and control the electrical bias and optical bias to minimize the signal. The process repeats until the repetition of the process does not change the EQE signal significantly. The residual artifact that could not be completely removed is corrected by subtracting a baseline, which is the middle junction EQE multiplied by a small number similar to the artifact in scale. The result of the measurement is shown in Figure4.10

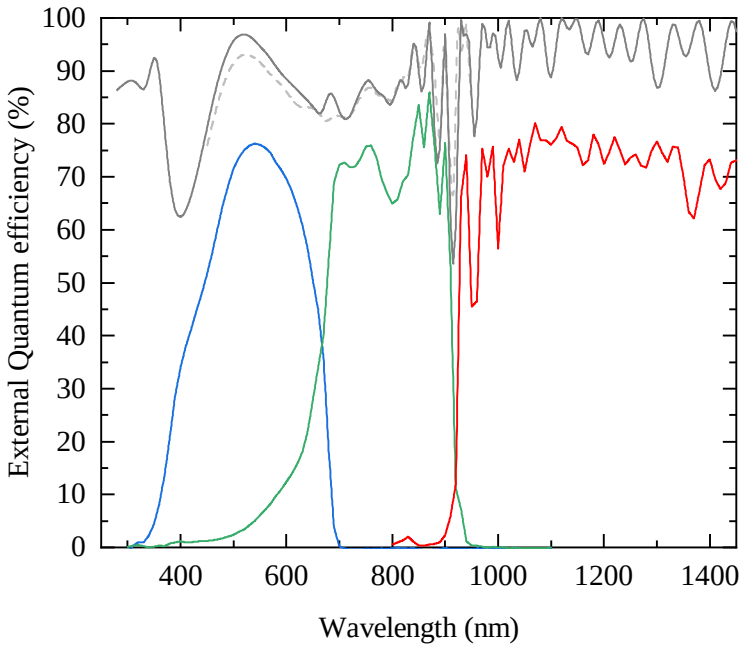

Figure 4.10: EQE and reflection of PEC device covered with the ITO layer. The blue, green and red lines represent EQE of the top, middle and bottom junction. The solid and dashed grey line represents calculated and measured reflection of the PEC device.

To derived the IQE of the device, the reflection of the PEC device covered with the ITO contact layer also should be found. The dashed gray line in Figure 4.10 shows the measured reflectance (100 % - reflectance) from 450 nm to 900 nm. Because the reflection measurement does not cover the entire spectrum range of the PEC device, it is also calculated using the same method introduced in section 3.2.2. For the reflection calculation, the refractive index of the TiO_2, GaInP, GaAs and Ge are adopted from the references,

but the refractive index of ITO is measured by ellipsometry in this study because it depends largely on the deposition condition. The measured and fitted ellipsometry data are shown in Figure 4.11. The model used for fitting the ellipsometry data is introduced in the reference. Figure 3.13 shows the refractive index of ITO derived from the ellipsometry data is shown together with the refractive index of the other materials used in this study. By using the refractive index and the transfer matrix method, the reflectance of the PEC device is calculated and shown in Figure 4.10 (solid grey line). Using the calculated reflectance and EQE measurement, IQE can be derived by the equation 4.1.

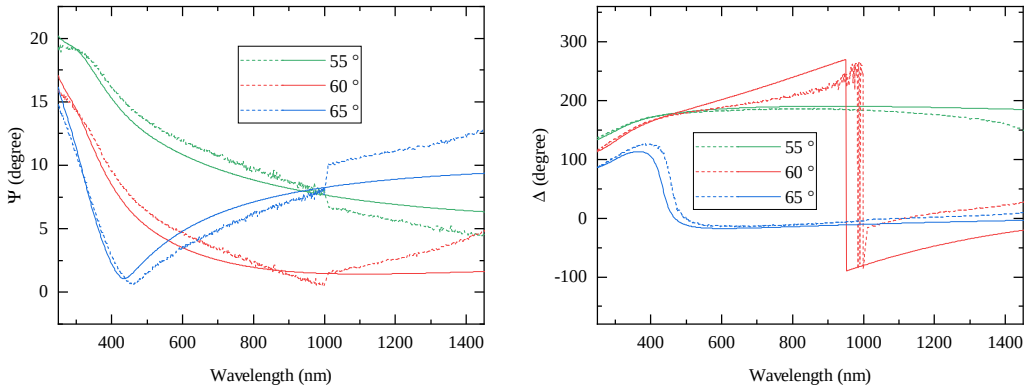

Figure 4.11: Ellipsometry data for measuring the refractive index of ITO. The measurements are carried out with three different incidence angles, 55°, 60° and 65°. Dashed and solid lines are measurement and fitting, respectively.

4.3.3 The current density from each junction

By using IQE and the reflection, it is possible to derive the current density from each junction by multiplying the spectral intensity of the light source, internal quantum efficiency, 1 - reflection of the device and the absorption by water layer as shown in the following equation.

$$J_i = \int_{300}^{1800} Intensity(\lambda) \times IQE_i(\lambda) \times (1 - R(\lambda)) \times e^{-\alpha d} d\lambda \tag{4.2}$$

Here, α and d are the absorption coefficient (Figure 4.1) and the thickness of water, which is assumed to be 2 mm, to consider the light absorption by the water layer. Subscript i represents each junction. It should be noted that the reflection in this equation is not from the reflection in the air, but the reflection in the water. The reflection of the PEC device in water is calculated by using the same matrix transfer method (see section 3.2.2), but the air is replaced with water in the calculation model. The refractive index of water is assumed to be 1.33 all over the wavelength. The calculated reflection depends on the thickness of the TiO_2 protection layer. Thus, the expected current density from each junction also changes depending on the thickness of the TiO_2 protection layer, as shown in Figure 4.12. The purple, green and yellow line represents the expected current density from the top, middle and bottom junction of PEC device depending on the thickness of TiO_2 protection layer thicknesses.

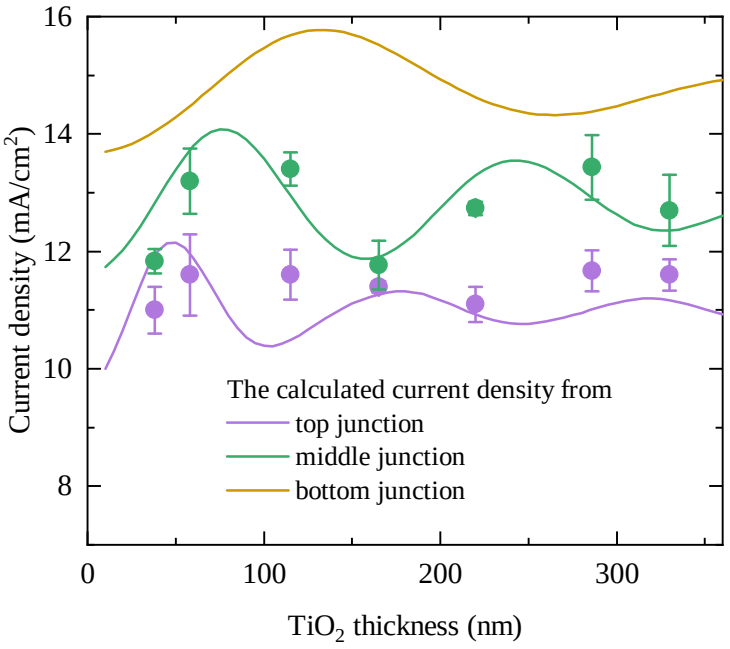

Figure 4.12: The solid line shows the calculated current density form each junction. The purple and green datapoints are the current density measured without or with the additional blue light, respectively.

The solid lines are showing a periodic change over the thickness of TiO_2 protection layer because of the interference of light inside of the layer. The interference results in destructive interference when satisfying the following equation.

$$d = \left(\frac{1}{4} + \frac{1}{2}m\right)\frac{\lambda}{n} \tag{4.3}$$

Here, d, m, λ and n represents the thickness of TiO_2, any integer number, wavelength of light in vacuum and the refractive index of TiO_2. The equation 4.3 implies that, as TiO_2 layer thickness increases, the reflection changes periodically with half-wavelength periodicity, and there will be the first minimum in reflection at quarter-wavelength thickness. Take the top junction as an example, the wavelength of the light corresponding to the top junction is around 600 nm in a vacuum, and its wavelength in TiO_2 is around 240 nm because the refractive index of TiO_2 is around 2.5 (600 nm/2.5). Therefore, the first minimum in the reflection would be a quarter of 240 nm, which is 60 nm. The calculated current density from the top junction also shows a larger reflection around 60 nm because the light corresponding to the top junction has the first minimum in the reflection. The periodicity of the reflection is half-wavelength, which is 120 nm. Therefore, the second and third minimum of the reflection would be around 180 nm and 300 nm, and the calculated current density from the top junction also has maximums around the wavelengths. The same goes for the middle and bottom junction with longer periodicity because they are

absorbing longer wavelengths of light. The calculation result on the middle and bottom junction shows around 160 nm and 280 nm of periodicity. The different periodic change in the calculated current density from each junction shows that it would be difficult to prepare an ideal anti-reflective coating by using a monolayer.

No matter what the TiO_2 thickness is, the current density from the top junction is the smallest. The purple data points are the measured current density from PEC devices under the standard light source, which are depicted in Figure 4.5 as a black graph, and it is in accordance with the calculation result. The green data points in Figure 4.12 shows the current density measured with the additional blue light, which is depicted in Figure 4.5 as a blue graph, and the measured current density matches very well with the calculated current density from the middle junction. This result clearly shows that the current density of this PEC device is always limited by the top junction, as discussed in section 4.2.2. To be more specific about the loss mechanism, the III-V solar cell used in this study is able to produce 17 mA/cm^2 under the AM0 spectrum, according to the datasheet provided by the solar cell provider. However, this study uses the standard light source reproducing AM 1.5G spectrum, and as explained in section 3.2.1, it has a smaller intensity in UV range due to Rayleigh scattering. When considering the intensity difference, the current density from the top junction is decreased to 13.5 mA/cm^2. It seems that there is a parasitic loss of 0.9 mA/cm^2 possibly due to absorption by Pt catalyst, Ti adhesion layer or TiO_2 protection layer. Thus the PEC device without any reflection has 12.6 mA/cm^2 from the top junction. In addition, the reflection depending on TiO_2 thickness reduces the current density further, so that the current density from the top junction varies between 10 $\sim$ 12.1 mA/cm$_2$.

By conducting the same calculation using equation 4.2 with different water layer thicknesses, it is possible to figure out the water layer affects the performance of the PEC device. Figure 4.13 shows the current density from each junction with 1, 2, 4 and 8 mm of water layer thickness. The current density from the top and middle junction do not show an apparent difference. However, the current density from the bottom junction decreases drastically because water has a much larger absorption coefficient at infrared range compared to the visible light range. This calculation result is in accordance with the measurement with different water layer thicknesses (Figure 4.2). The Ge bottom junction does not limit the current density when the water layer thickness is less than 2 mm.

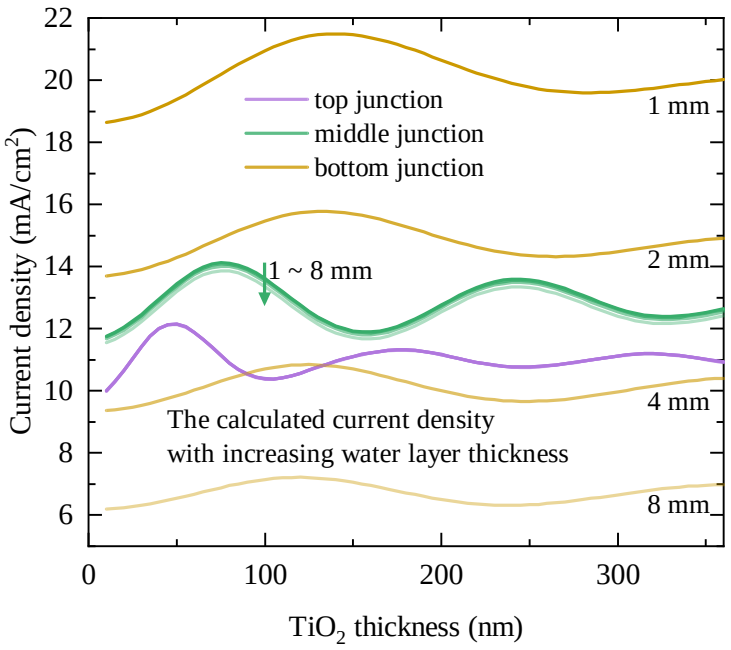

Figure 4.13: The calculated current density with varying water layer thickness. While the water layer thickness changes from 1 mm to 8, top junction current density is more or less the same, middle junction current density decreases only slightly, and bottom junction current density decreases drastically.

CHAPTER 5

Improving the stability of PEC devices

One of the most major challenges in PEC study is improving the stability of PEC devices.[39, 56] As explained in the section 2.4.1, PEC devices need to be able to produce at least two orders of magnitude larger amount of hydrogen over its lifetime compared to the current level of studies to find economic feasibility, and it corresponds to about $\sim$ 10 years of operation.[56] Thus, a major breakthrough in the stability would be necessary to produce hydrogen from PEC.

This chapter will start by discussing important considerations for characterizing the stability of PEC devices first and explain why the analysis of the gaseous product is important. After that, the stability tests on PEC devices based on the III-V solar cell with various thicknesses of TiO_2 protection layers in wired or wireless configuration will be presented, and the corrosion mechanism of this specific PEC device will also be dissed. The key messages to be delivered in this chapter are 1) the rigorous stability test with gas collection shows the best record in H_2-lifetime among wireless devices, and 2) further improvement in the stability is achieved (more than 2 weeks of operation) by thickening TiO_2 protection layer for removing pin-holes and illuminating UV-light.

5.1 Considerations for PEC stability test

In most previous studies, the stability of PEC devices has been usually tested by collecting charges over long hours in an electrolyte.[41–48, 83–101] To collect the charges from PEC devices, a wired or inverted-wired configuration (Figure 2.8) is usually adopted, and the devices are held at a certain electrochemical potential for doing chronoamperometry. The figure of merit used for the stability of the PEC device is usually operation time, and the reduction in the current density is often described together. For example, the stability of PEC devices are expressed as ”The PEC device operated 24 hours and 90 % of the initial current density is maintained at the end of the test.”.

However, it is important to realize that carrying out only chronoamperometry may not be a pertinent method for the stability test because the collected charges from the chronoamperometry may not be from a water-splitting reaction but from other miscellaneous reaction. For example, carbon contaminants in an electrochemical cell could be oxidized or

reduced on the PEC device, and it will contribute to the measured current density. The corrosion of the PEC device could also provide electrical charges. In other words, faradaic efficiency during stability tests may not always be 100 %, therefore it is necessary to analyze the products directly. Nevertheless, most studies have tested the stability only by collecting charge because charge collection is a much more facile method compared to gas collection.

In addition, when considering that the advantage of PEC can be fully utilized in a wireless configuration (see discussions in section 2.3.1), a stability test in the wireless configuration would be more interesting than that in a wired configuration. However, testing a wireless device is more challenging than testing a wired device because 1) both front and backside of the solar cell are opened to an electrolyte, and 2) charge collection from the wireless device is not possible. Because of the difficulties, there are only a few studies on the stability of the wireless device.[102–104]

If a PEC device should be tested in a wired configuration, the electrochemical potential of the device should be chosen close to a proper level because the testing environment would be fundamentally different depending on the electrochemical potential.[105] For example, if a PEC device can provide a sufficient photovoltage to drive an electrochemical reaction, it would be more informative when tested by short-circuiting the working and counter electrodes (0 V vs counter electrode in two-electrode setup). In this way, the PEC device is tested without any assistance from the external power supply and realizes unassisted water-splitting.

Lastly, one may consider using the total amount of products produced over the lifetime of the PEC device (H_2-lifetime) as a figure of merit for expressing the stability of the PEC device instead of operation time. The major advantage of using H_2-lifetime as a figure of merit is that the cost for hydrogen production (in the unit of USD/kgH_2) can be directly deduced by dividing the system cost by H_2-lifetime. According to the techno-economic analysis from DOE [55, 56], PEC could find the economic feasibility when it reaches H_2-lifetime reaches 150 L/cm^2 based on assumptions for producing 1 ton of hydrogen per day.

In this study, both wired and wireless configurations are tested for stability. When collecting the gaseous product from a device, a leak test is always carried out to make it less than $\sim$ 1 % of the expected amount of product. The wired devices are always tested at 0 V vs IrO_2, and H_2-lifetime is provided as the figure of merit. In the following sections, two key points regarding the importance of the gas collection and significant improvement in the stability by thickening the protection layer will be delivered with experimental results.

5.2 The importance of gas collection

In the previous chapter, wired PEC devices whose protection layer thicknesses range from 50 $\sim$ 350 nm are tested to correlate their activity and reflection (Figure 4.12A). The stability of all of these devices are tested by charge collection, and gaseous products from

some of the devices are collected to compare it with charge collection.

5.2.1 Stability test on the wired devices by charge collection

The stability of the wired PEC devices is investigated by collecting the current density generated during a chronoamperometry. As explained in the previous section, a two-electrode setup is adopted for the chronoamperometry by having a PEC device as a working electrode and IrO_2 as a counter electrode.The working and the counter electrodes are short-circuited so that the water-splitting reaction is driven only by the PEC device without any external assistance (see also section 3.2.3 for details). One of the most stable PEC devices in this study has 277 nm of protection layer operates more than 70 hours, and the total amount of charge passed over the lifetime of the PEC device is equivalent to 231 ml/cm^2 of hydrogen (Figure 5.1A). Figure 5.1B compares the stability test with the other studies testing the stability of unassisted PEC devices by charge collection and shows that H_2-lifetime of the device is in the range of the best record. Please note that the y-axis is the equivalent amount of hydrogen, which is derived with an assumption that all of the charges are from the water-splitting reaction.

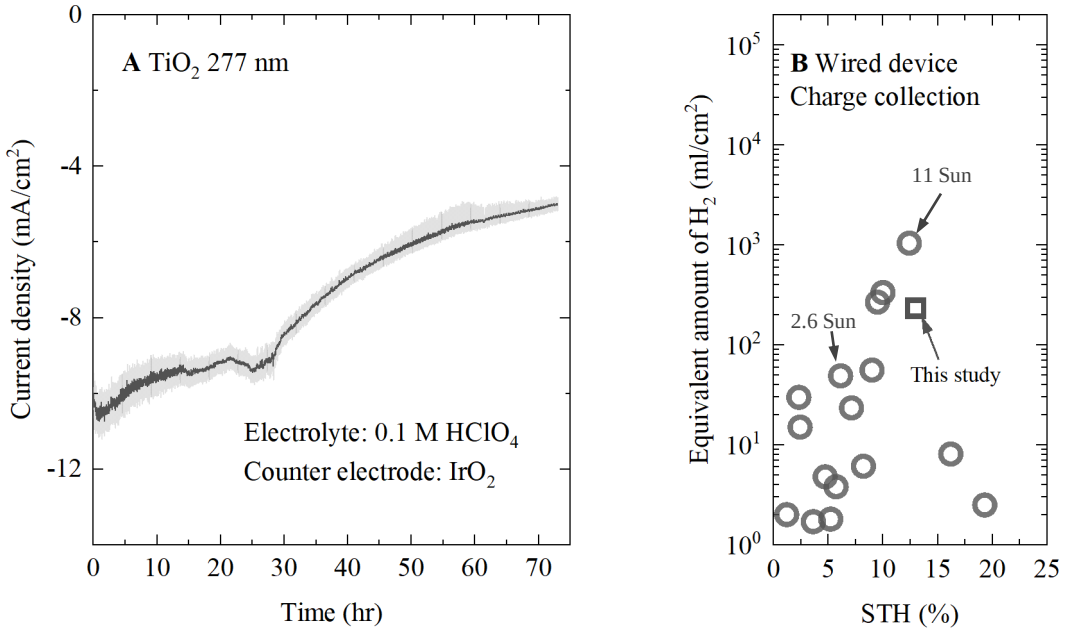

Figure 5.1: The stability test on the PEC device with 277 nm of TiO_2 protection layer. (A) The device operated more than 70 hours, and (B) H_2-lifetime from this thesis and selected papers.

Although the device operated over 70 hours, the current density from the device decreases continuously over its lifetime. Cyclic voltammetry acquired from another device tested over 50 hours (Figure 5.2) shows that both photovoltage and photocurrent density decrease from 2.4 V to 2.1 V and 12 mA/cm^2 to 9 mA/cm^2, respectively. The reduction in

photovoltage and photocurrent would come possibly from the corrosion of the GaInP top junction beneath the protection layer. More details about the corrosion mechanism will be discussed later. The more important point is that the products from the devices should be analyzed to be sure that the current density is originated from a water-splitting reaction.

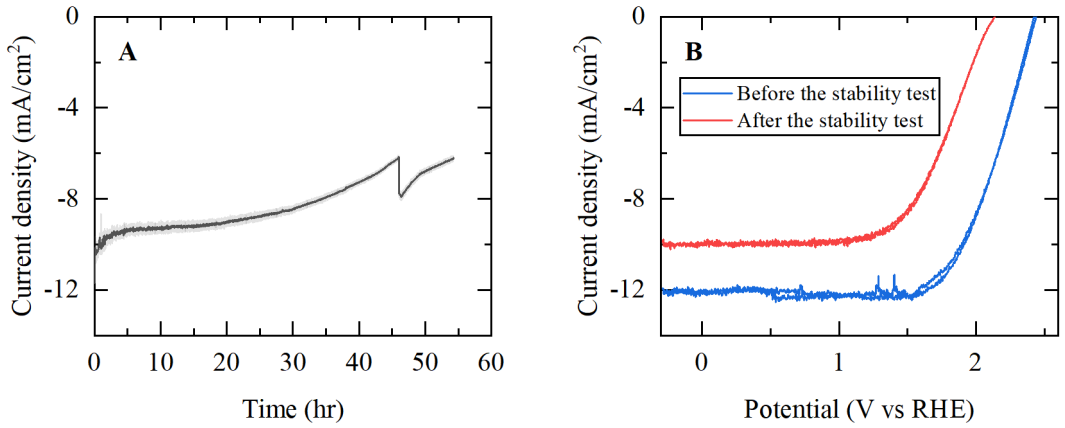

Figure 5.2: The stability test on PEC device. (A) Another stability test over 50 hours (B) Cyclic voltammetry before and after the stability test.

5.2.2 Stability test on a wired device by both charge and gas collection

Even though collecting charges would be a facile way to test the stability of PEC devices, however, a more rigorous way to test the stability is to analyze the gaseous product itself. To carry out the stability test more rigorously, both hydrogen and oxygen products are collected from the electrochemical cell by connecting eudiometers. Figure 5.3A shows chronoamperometry data from one of the stability tests and Figure 5.3B shows the amount of hydrogen and oxygen collected during the test. Notice that the scales of the left y-axis for hydrogen and the right y-axis for oxygen are different by a factor of 2 so that two data points for hydrogen volume and oxygen volume are overlapping each other when they are in the stoichiometric ratio (2:1). The solid line in Figure 5.3B is the equivalent amount of gas volume derived from the charge collection in Figure 5.3A. It is interesting to notice that the amounts of collected gases are not in the stoichiometric ratio after 25 hours of operation. The hydrogen volume is clearly smaller than the expected amount from the charge collection, and it could be related to visibly large corrosion that appeared after $\sim$ 20 of operation. The discrepancy between the charge collection and the gas collection shows that true stability should be measured from the gaseous products.

5.2.3 Stability test on a wireless device by gas collection

A wireless PEC should be used for practical hydrogen production to fully utilize the advantage of PEC (see discussions in section 2.3.1), thus the stability test on a wireless device would also be important. Because wireless devices does not have any external wiring, collecting the gaseous product would be the only way to characterize its stability. The gaseous products from the wireless devices are collected by using the compression cell and eudiometers. Technical details about the compression cell and gas volume mea-

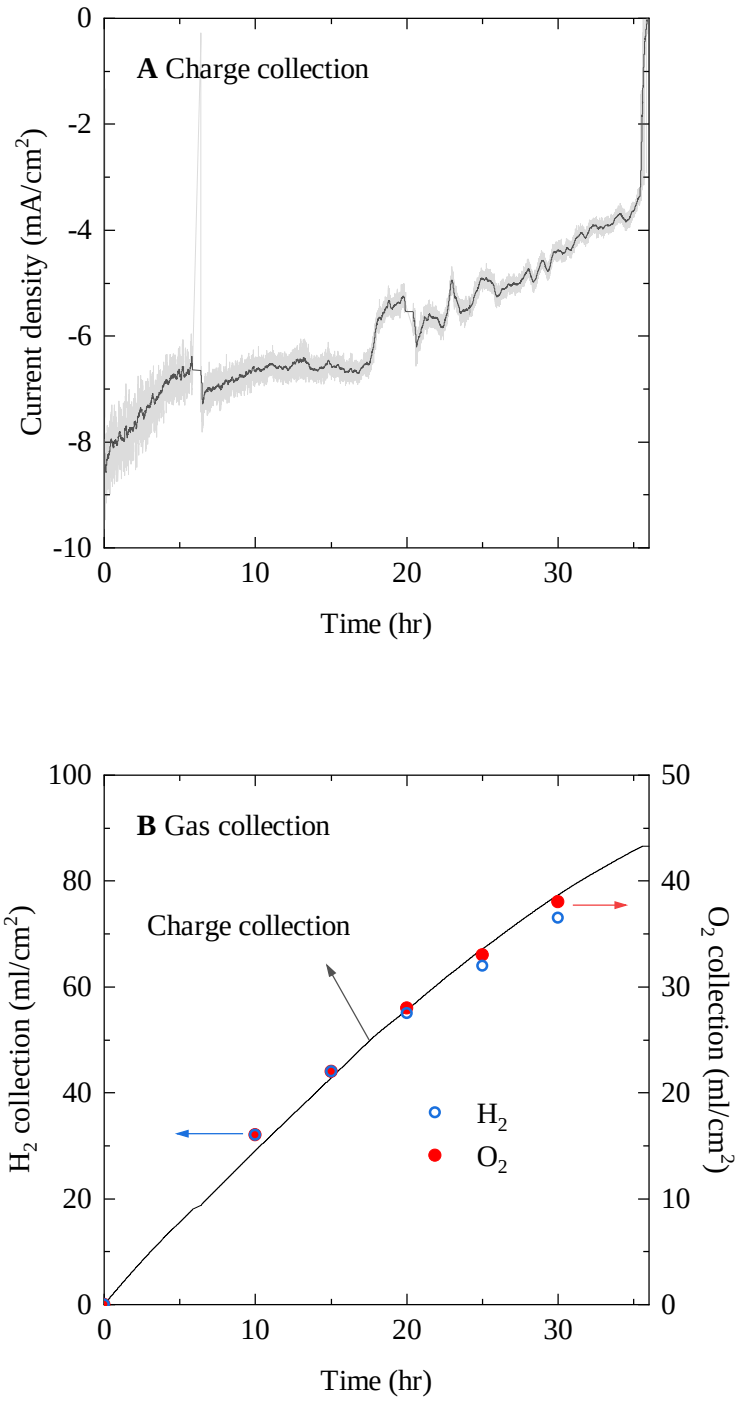

Figure 5.3: Comparision on the stability tests done by (A) charge collection and (B) gas collection. After $\sim$ 25 hours of operation, the volume of collected hydrogen becomes smaller than that expected from the charge collection. This measurement shows the importance of analyzing the gaseous products for the stability test.

surement by using the eudiometers are described in section 3.2.4, and Figure 5.4 shows the photo of them.

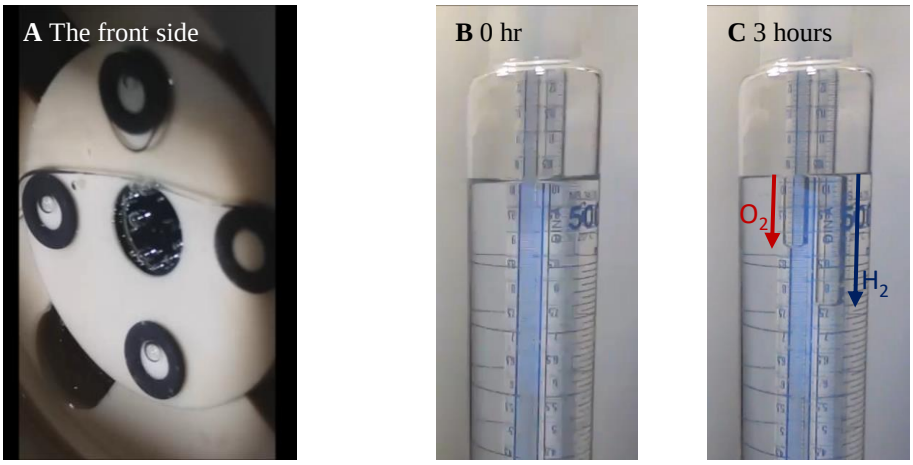

Figure 5.4: The photos showing the gas collection using the compression cell and eudiometers. (A) shows the front side of the PEC device. (B) Before starting the experiment, the water level inside of the eudiometers is equal to the water bath. (C) After 3 hours of operation, the volume of gas expands to push the water level inside of the eudiometers.

Figure 5.5A shows the amount of hydrogen and oxygen collected in the eudiometers for the first 1 hour to determine the activity of the device. As expected from the stoichiometric ratio, the volume of hydrogen and oxygen are in the 2:1 ratio, and the solid line is a linear fitting to the data points. The STH efficiency derived from the line is 13 %. There is a periodic change in the data points, for example, the rate of gas production at 20, 35 and 50 min seems to be slightly faster than 30 and 40 min. This periodic change in activity is originated from sluggish oxygen bubble removal at the backside of the PEC device. The stability test on the wireless device with the gas collection is carried out until the end of the device lifetime, and the H_2-lifetime reached 51 ml/cm^2. Compared to other wireless PEC devices, the PEC device in this study shows higher STH efficiency and H_2-lifetime as shown in Figure 5.5B.

5.3 Corrosion process of the PEC device

To improve the stability of the PEC devices, the corrosion mechanism of these specific PEC devices tested in these studies are investigated by using several different techniques. Because most of the devices are tested in acid, the corrosion mechanism in acid is mainly discussed, but the corrosion mechanism in the alkaline condition is also shortly discussed.

5.3.1 Corrosion in acidic electrolyte

After the stability tests in perchloric acid, the surface of PEC devices is observed by SEM and EDS, as shown in Figure 5.6 to discuss the corrosion mechanism. The figures in the left column (Figure 5.6A,C and H) show the initial stage of corrosion, which were taken about an hour after doing the stability test. In the SEM image (Figure 5.6A), dark spots appear over the surface. EDS line scan over the yellow line in Figure 5.6A shows that the dark spots are showing a lower signal from indium and phosphorous, which are

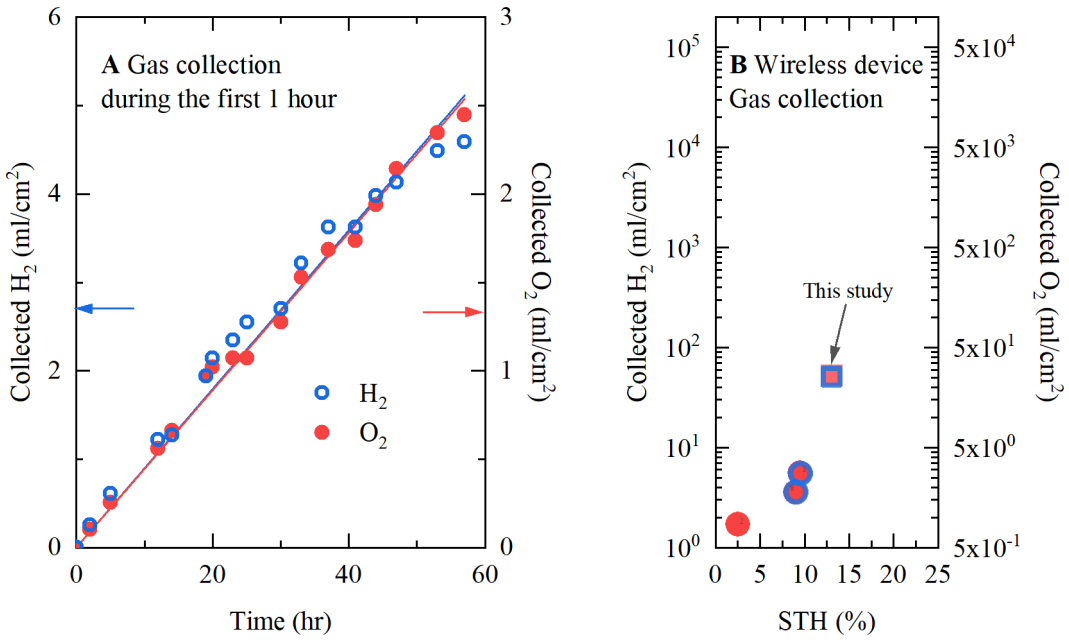

Figure 5.5: The amount of hydrogen collected over the lifetime of PEC devices from this thesis and selected papers.

comprising GaInP top junction, compared to the background (Figure 5.6C). It shows that the corrosion of the top junction already takes place during the first 1 hour of operation. The other figures on the right column (Figure 5.6 B, D, E, F, G and I) show the surface of the device after the stability test. In the SEM image (Figure 5.6B), there is considerable corrosion in the middle, and it is surrounded by a crack. When considering the crack line is sharp and has a rectangular shape, the crack formation could be relevant with the crystalline orientation of a single-crystalline solar cell. EDS mapping on this area ((Figure 5.6 D, E, F and G) shows that GaInP top junction corrodes and GaAs middle junction is opened in the middle. Possibly because GaAs has a faster etch rate in acid compared to GaInP, the GaAs middle junction underneath the GaInP top junction dissolves quickly, and it results in the crack in the top junction in the area where the middle junction is lost. Figure 5.6H and I show a schematic diagram explaining the corrosion process. Through the pin-hole in TiO_2 protection layer, GaInP top junction begins to corrode and it is shown as the dark spots in the SEM image (Figure 5.6A). As the electrolyte penetrates through the top junction and meets the GaAs middle junction, it dissolves the GaAs layer beneath the GaInP top junction, and it eventually delaminates the top junction. To improve the stability of PEC device, it is important to remove any pin-hole in the protection layer and to prevent the start of corrosion.

The delaminated of the top junction is observed by SEM to further support the explanation on the device corrosion process. A flake detached from the device surface is

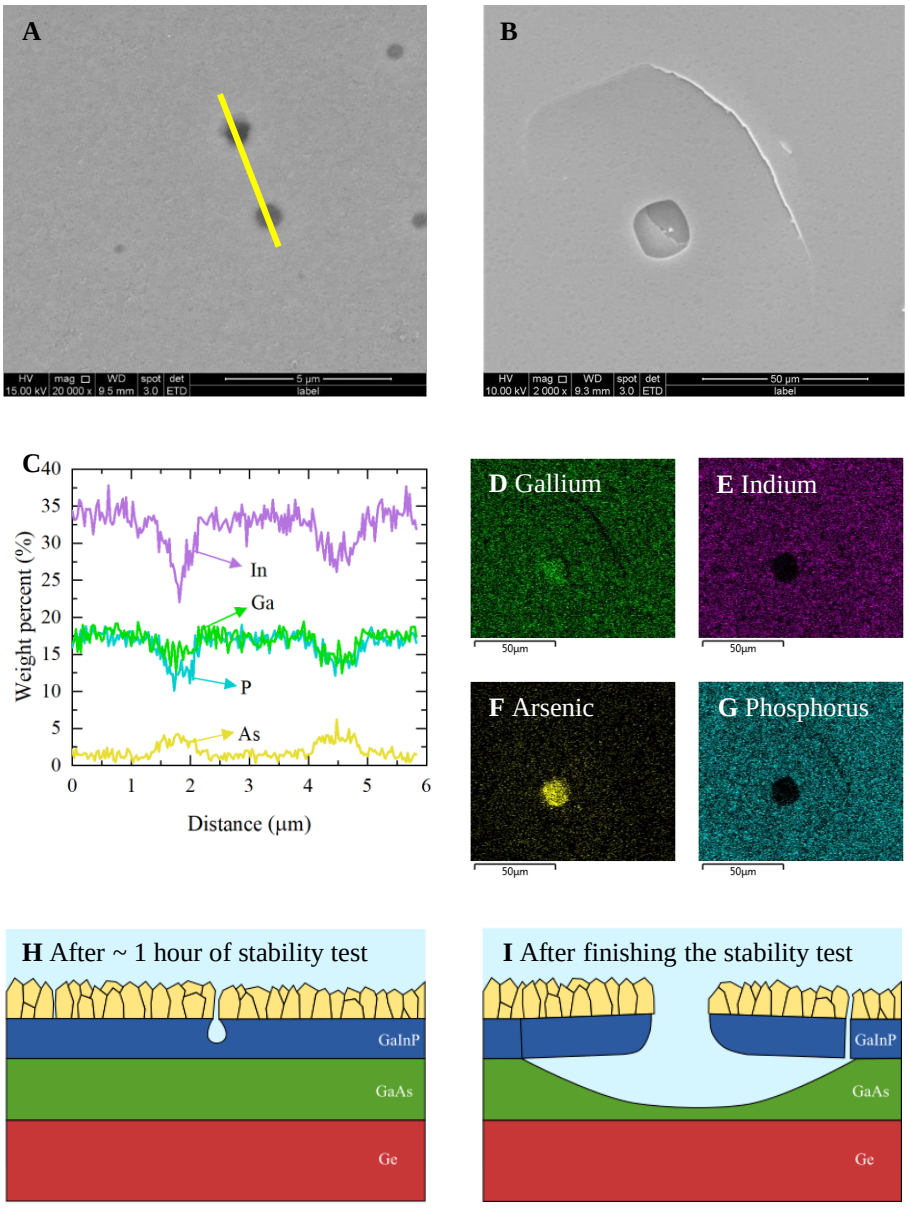

Figure 5.6: The surface of PEC device observed by SEM and EDS in the earlier (A and C) and later (B, D, E, F and G) stage of corrosion. The corrosion process of the PEC device are illustrated in (H) and (I).

transferred on to a silicon wafer and observed by SEM and EDS, as shown in Figure 5.7A and B. While the flake shows a sharp edge, EDS mapping on the flake shows gallium, indium, and phosphorus, which should come from the top junction. Thus, the corrosion of the PEC device ends up with the delamination of the top junction.

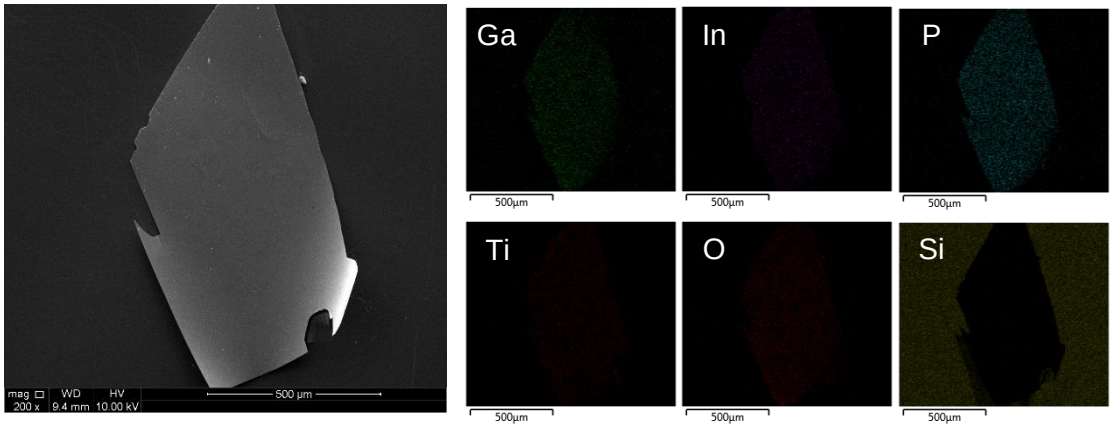

Figure 5.7: EDS mapping on a flake detached from surface by corrosion. It shows high signals from Ga, In and P, which should be from the top junction.

TiO_2 covered surface before and after a stability test is further characterized by XPS. Before the stability test, the surface shows titanium, oxygen and platinum, which are from the protection layer and catalyst as expected. After the stability test, the surface shows not only the afore-mentioned materials but also shows gallium, arsenic and tiny phosphorus signal (indium, which is also composing the solar cell, signal is not observable). The relatively smaller phosphorus signal compared to the arsenic signal is in accordance with the previous explanation on the corrosion mechanism. Because GaAs middle junction is more vulnerable to acid compared to GaInP top junction, a larger amount of GaAs is dissolved and adsorbed onto TiO_2.

To prevent the corrosion process, it would be essential to remove any pin-holes in the TiO_2 protection layer. There have been studies on removing the pin-hole in TiO_2 protection layer to acquire higher stability. Dowon et al. compared TiO_2 protection layer deposited by DC magnetron sputtering and high-power impulse magnetron sputtering (HiPMS). TiO_2 protection layer deposited by HiPMS shows a higher mass-density and lower number of pin-holes than that deposited by DC magnetron sputtering. By reducing pin-holes by HiPMS, silicon photocathode in 1 M KOH showed improved stability. Kornblum et al. deposited single-crystalline TiO_2 by pulsed laser deposition over a single-crystalline GaAs solar cell.[83] Because of the high crystallinity, the TiO_2 protection layer does not have any pin-holes and the GaAs device also showed improved stability. In this study, the thickness of the TiO_2 protection layer is increased to remove pin-hole and improved the stability of PEC devices significantly. The stability test with the thick TiO_2 protection layer is presented in the following section.

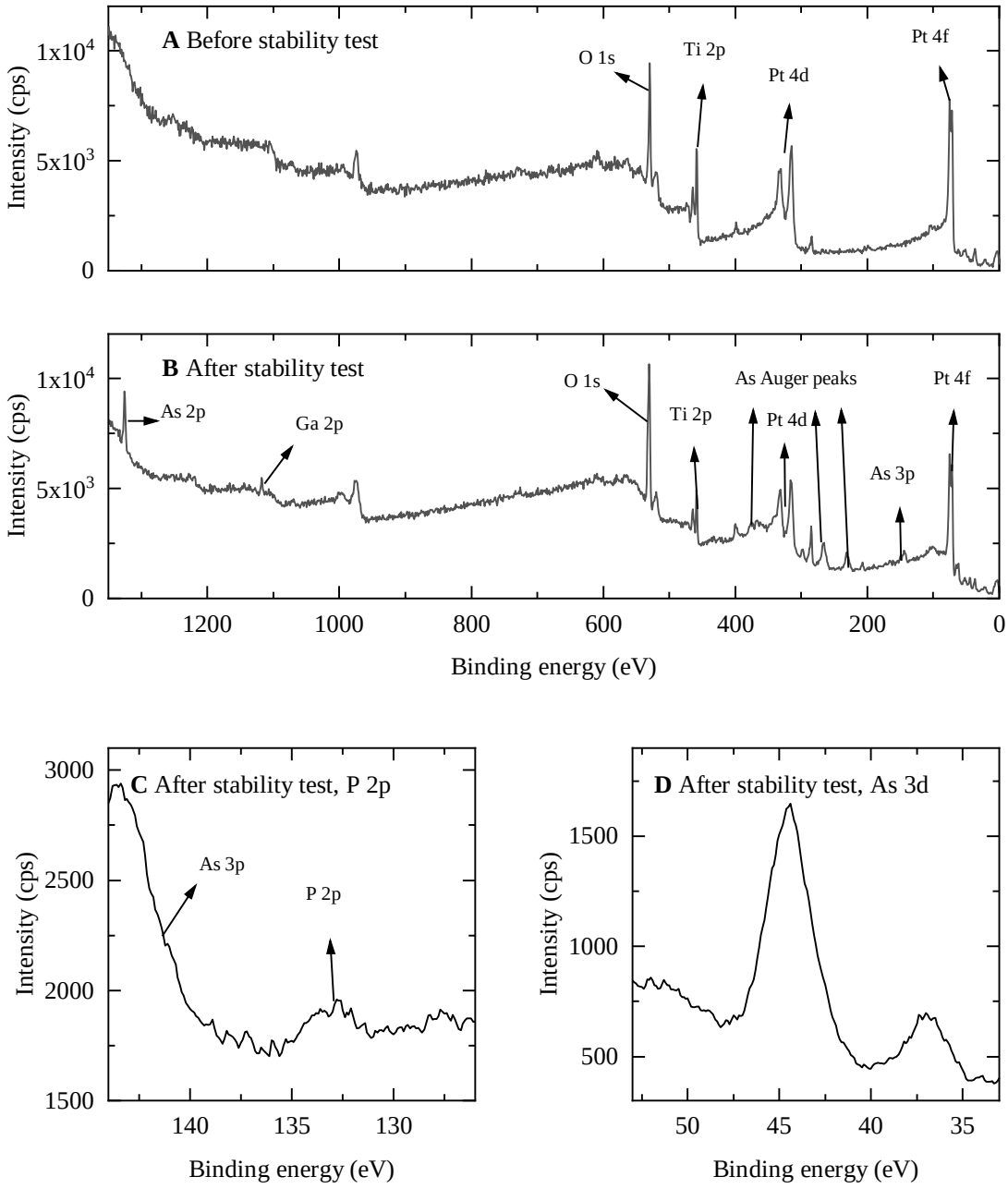

Figure 5.8: XPS on TiO_2 layer (A) before and (B, C and D) after the stability test. The XPS measurement shows higher arsenic signal from the middle junction dissolution, while showing only a minute amount of phosphorous from the top junction dissolution.

While the front side of the PEC device is protected by the TiO_2 protection layer, the backside of the wireless device, which is a germanium substrate covered with 20 nm Au contact layer, should also be protected. Because the backside of the wireless device does not have to be transparent, it is relatively easier to prepare the protection layer for the backside. 2 μm of metallic Ti or 300 nm of TiO_2 are tested as the protection layer for the backside, which are covered with 20 nm of IrO_2 as OER catalyst. Figure 5.9 compares the surface of the backside protected by two different protection layers (please notice that the scale bars for two SEM images are significantly different). The backside protected by 2 μm of metallic Ti (Figure 5.9A) did not show any significant corrosion at least until the front side corrodes, possibly because any pin-holes in the protection layer are removed. Dark spots on the surface in the SEM image 5.9A) potentially be carbon-contaminants and easily burnt by the electron beam in SEM. However, if the backside is protected by a much thinner 300 nm of TiO_2 protection layer, the backside shows many corrosion sites, which are visibly large by eyes, almost immediately (in 5 $\sim$ 10 minutes) after starting the stability test.

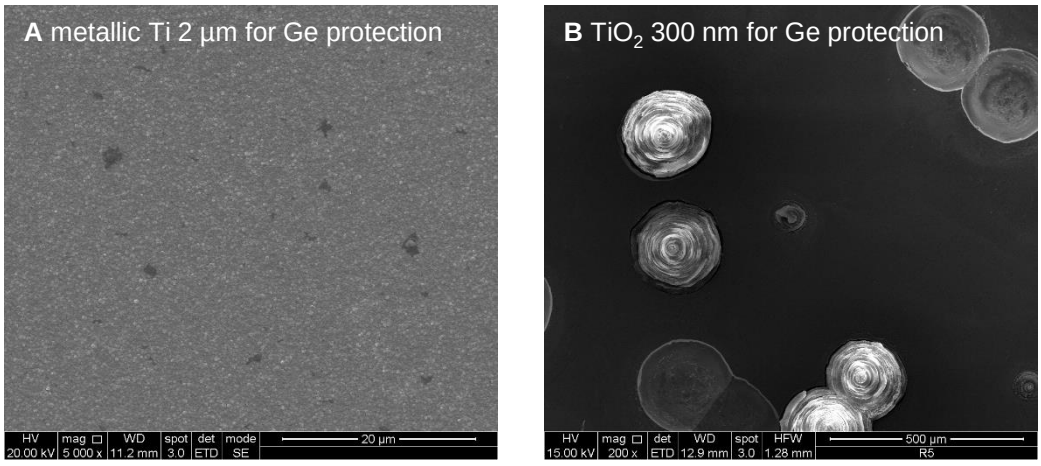

Figure 5.9: The backside of wireless devices (Ge substrate) after stability test with different protection layers. (A) Metallic Ti with 2 μm thickness successfully protected the backside. (B) TiO_2 layer with 300 nm failed to protect the device.

5.3.2 Corrosion in alkaline electrolyte

The stability of the front side of the PEC device in an alkaline condition is also observed. PEC devices are tested in 0.1 M KOH with a platinum catalyst in Ar saturated electrolyte or with a copper catalyst in CO saturated electrolyte (to assess the potential possibility of CO reduction by the PEC device, although it is out of the scope of this thesis). Figure 5.10A shows the cyclic voltammetry of two PEC devices with platinum and copper catalysts, respectively. Because of the large overpotential for CO reduction by a copper catalyst, cyclic voltammetry with the Cu catalyst begin to show current at much lower potential (1.8 V vs RHE) compared to the device with Pt catalyst (2.4 V vs RHE). The short-circuit current density from the device with Cu catalyst is smaller than that with Pt catalyst because Cu loading on the surface is around 5 nm, and it is large enough to absorb light. (Pt loading

is around 1 nm.) In alkaline condition, sputter-deposited NiFe film on Ti foil is used as a counter electrode, as shown in the blue graph. The cross point between the blue graph and the CV of the device is the point where the PEC devices will operate in a two-electrode setup without external energy input (0V vs NiFe). The stability test on those devices at 0 V vs NiFe is carried out over around 15 hours, as shown in Figure 5.10 (b). While the current density from the device with Pt catalyst decreases gradually, the current density from the device with Cu catalyst increases slightly for the first 3 hours and then decreases slowly. The increasing current at the first 3 hours could be from Ni or Fe contamination from the counter electrode, promoting the hydrogen evolution reaction.

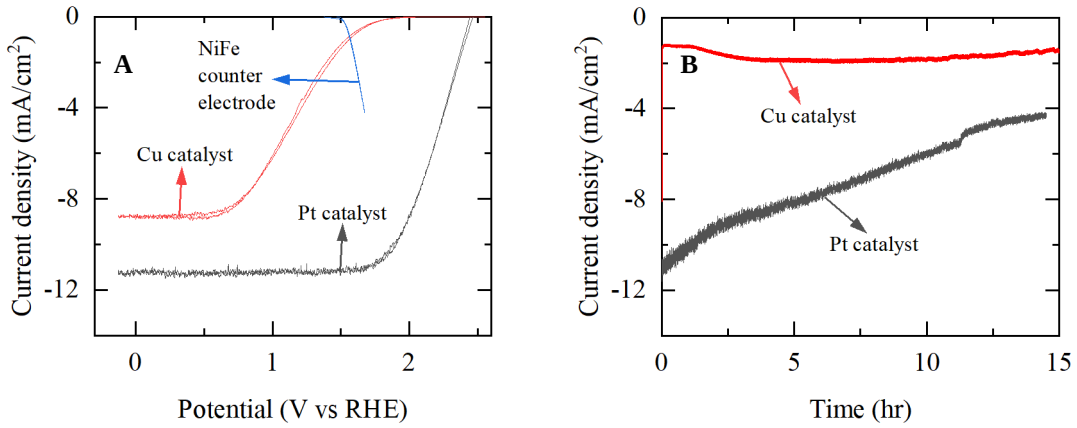

Figure 5.10: PEC device tested in 0.1 M KOH with Pt (black) catalyst in Ar saturated electrolyte, and with Cu (red) catalyst in CO saturated electrolyte. (A) Cyclic voltammetry shows a significant overpotential from CO reduction by Cu catalyst. The blue line shows the activity of the NiFe counter electrode. (B) The stability test in 0.1 M KOH with the devices.

After 15 hours of the stability test in 0.1 M KOH, the front side of the device is observed by SEM (Figure 5.11). The SEM images show that the corrosion in alkaline electrolytes leads to the delamination of the TiO_2 protection layer. Unlike the delamination of the single-crystalline top junction in acid (5.7), the delamination of poly-crystalline TiO_2 flake does not show a rectangular shape or sharp edges. Possibly because GaInP top junction is unstable in the alkaline electrolyte, unlike in acid, the top junction is dissolved, and only TiO_2 protection layer is delaminated. The cross-section of the delaminated flake shown in Figure 5.11 also shows around 200 nm of thickness, which is almost the same as the thickness of TiO_2 protection layer.

5.4 Stability improvement by thickening TiO_2 protection layer

To improve the stability of the PEC devices, pin-holes are removed by thickening the TiO_2 protection layer. In the following sections, the stability test results with the thick TiO_2 protection layer (1 > μm) will be presented. In addition, further improvement in the stability of UV-illumination will be shown.

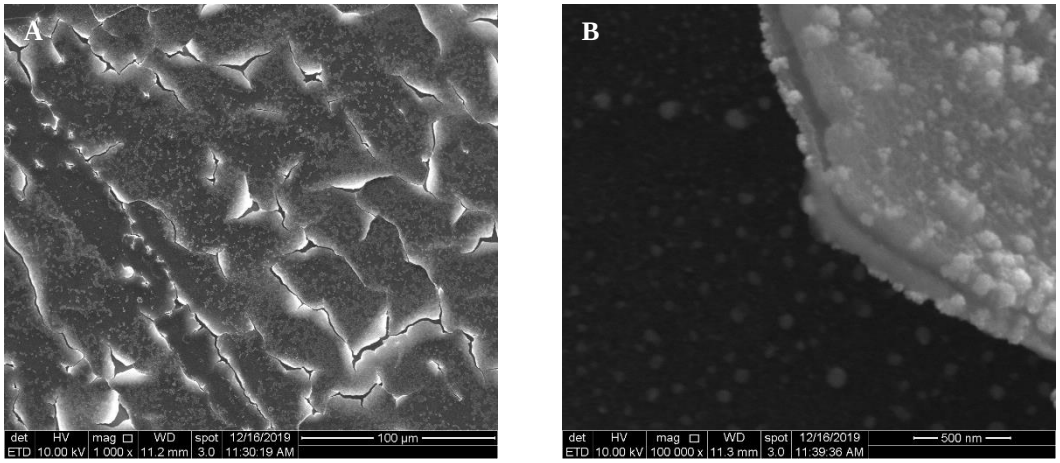

Figure 5.11: The surface of PEC device with Cu catalyst tested in CO saturated 0.1 M KOH for 15 hours.

5.4.1 Device performance with thick TiO_2 protection layers

Although it has been shown that TiO_2 with several nanometer $\sim$ hundreds nanometer of thickness conducts electrons successfully [41], such a thick TiO_2 layer could be resistive and hampers device performance. Thus, the activity of the devices is characterized by CV to see if the thick protection layer reduces the performance of the PEC device. The thick TiO_2 layer protection layer is deposited by sputtering at two different temperatures, room temperature and 400 °C. The CV from the devices with the thick protection layer is compared with a PEC device with a thin protection layer in Figure 5.12. When considering that the fill factor of the devices with a thick protection layer is not significantly reduced, thus the conduction over the thick TiO_2 protection layer is acceptable.

However, the current density decreases drastically when the thick protection layer is deposited at 400 °C. This reduction in the current density could be explained by the surface roughness of the protection layer. Figure 5.13 compares the surface and the cross-section of PEC devices with thick protection layer deposited at room temperature (Figure 5.13A and C) and 400 °C (Figure 5.13B and D). When TiO_2 protection layer is deposited at high temperature, it shows anatase crystallinity, which forms a pyramidical shape on the surface. Compared to a flat surface, the pyramidical structures cause scattering reflection that could not be absorbed by the PEC device.

The reflection measurement also shows the scattering effect by the pyramidical structures. Figure 5.14 shows the specular or total (specular+scattering) reflection from PEC devices. Compared to the reflection from thinner TiO_2 protection layers (Figure 4.7), the reflection from the thick protection layers are having a larger number of maximums and minimums in the spectrum because the number of constructive/destructive interference mode increases. When comparing the specular reflection from the devices with protection layers deposited at room temperature (blue) and 400 °C (red), the 400 °C device is showing a relatively smaller difference between the maximum and minimum, and it could be from a diffusive scattering of light by pyramidical structure. Because the spectrometer

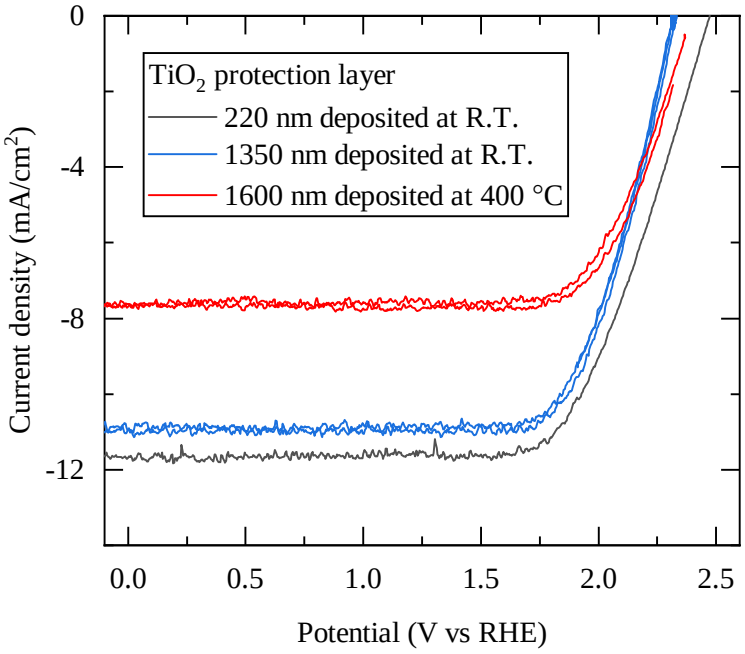

Figure 5.12: The activity of PEC devices with thick TiO_2 protection layers (> 1000 nm) are measured by CV and compared with that from the thinner protection layer (220 nm).

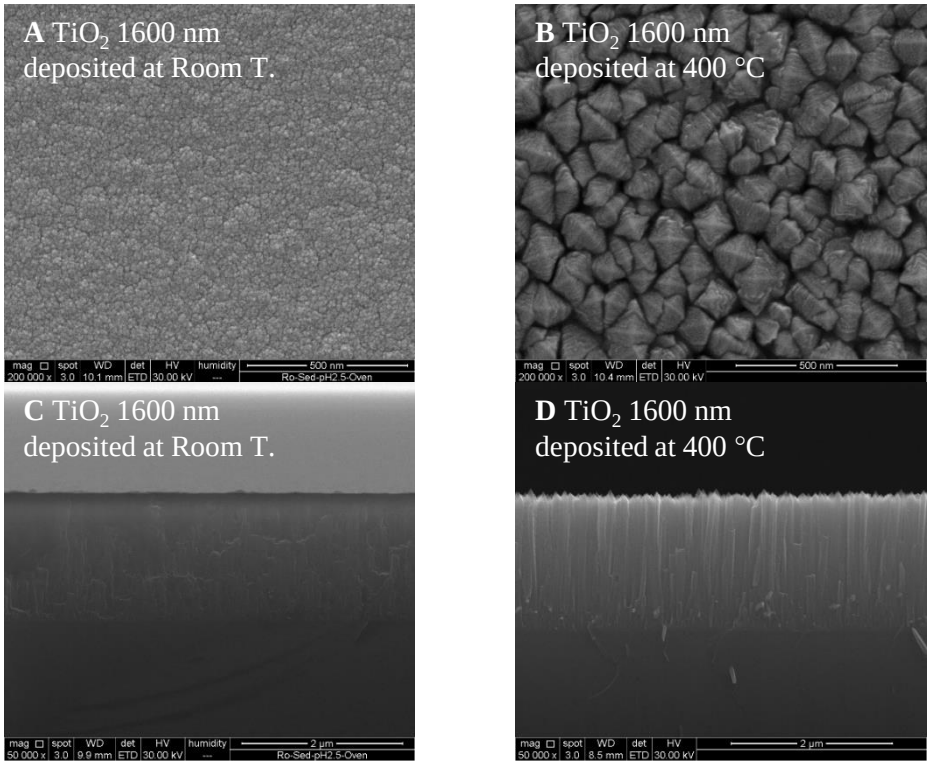

Figure 5.13: SEM images on the thick TiO_2 layers deposited at room temperature (A and C) and 400 °C (B and D)

used for the reflectance measurement can only measure specular reflection, a scattered reflection of light is excluded from the measurement. To measure the total reflection (specular + scattering) from the device, an integrating sphere is combined with a spectrometer. The total reflection from the 400 °C device has higher reflection over the broad range of spectrum, as shown in the orange line in Figure 5.14. Thus, it seems that higher reflection from the pyramidical structure results in the lower current density from the PEC device. To avoid the diffusive scattering, only room temperature deposited devices are tested for the stability test.

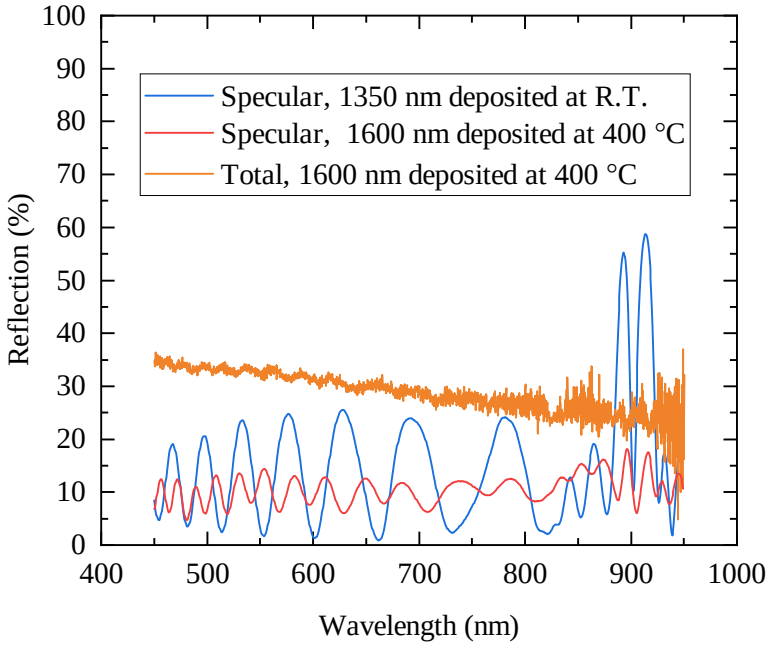

Figure 5.14: The reflection measured from PEC devices with thick protection layers.

5.4.2 Counting the number of pin-holes depending on TiO_2 layer thickness

It is expected that the corrosion of PEC devices starts from the pin-holes in a protection layer (Please see section 5.3). Therefore, it is critically important to reduce the number of pin-holes. To count the number of pin-holes in TiO_2 protection layers depending on its thickness, three different thicknesses of the protection layer is deposited on a silicon wafer in (100) direction by sputtering at room temperature. Then the silicon wafers with TiO_2 layer are immersed in 0.1 M KOH for one day. Because silicon has a slower etch rate in (111) direction by KOH, it leaves the pyramidical shape of corrosion spots under the pin-holes, as shown in Figure 5.15A, and the characteristic shape makes the pin-holes easily differentiated from other minor features, such as particulate contaminants. Figure 5.15B, C and D show the distribution of pin-holes over 50, 250 and 1100 nm of TiO_2 covered silicon wafer, respectively. It seems clear that the number of pin-holes decreases as the protection layer thickness increases. Although the local crystallinity inside of the TiO_2

layer could depend on the substrate where the layer starts to grow so that the actual number of pin-holes on a PEC device could be different, it seems clear that the number of pin-holes can be reduced by thickening the protection layer.

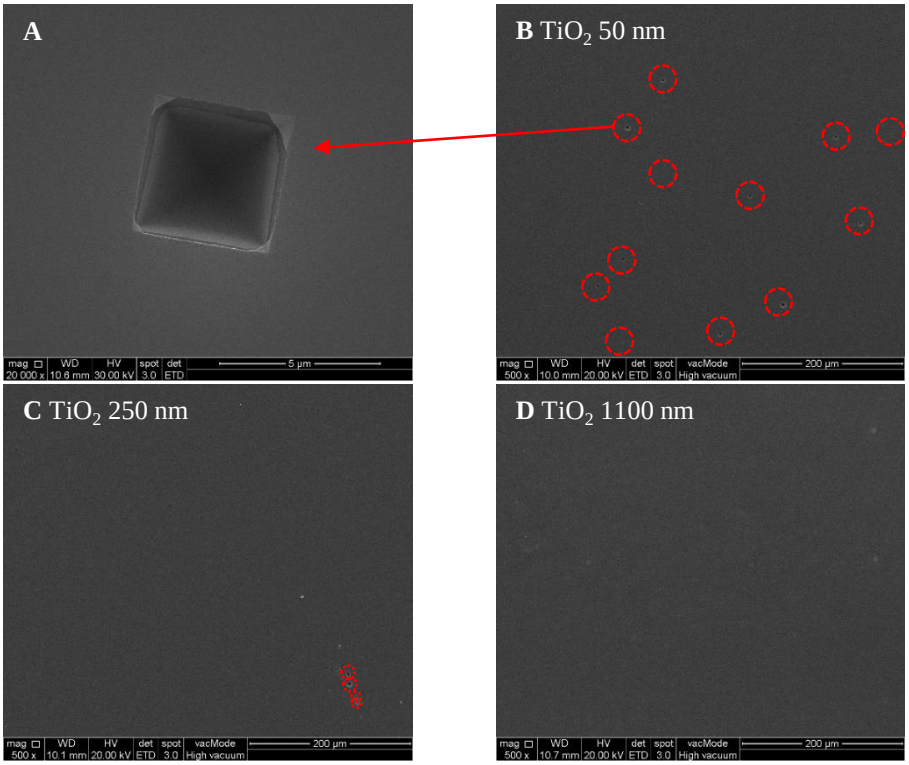

Figure 5.15: The number of pinholes over the TiO_2 layers with different thicknesses deposited on silicon wafers are counted by immersing the wafers in 0.1 M KOH for 1 day.

The number of pin-holes is counted at randomly chosen five places in SEM, and the average and standard deviation of the numbers are plotted in Figure 5.16. After immersing the silicon wafers with 50 nm and 250 nm of TiO_2 protection layer in 0.1 M KOH for one day, the density of pin-holes found over the surfaces are 86 ± 66 and 23 ± 15 counts/cm^2, respectively. In the case of a silicon wafer with 1100 nm of TiO_2 protection layer, any pin-hole is not observed by SEM over 2 cm $\times$ 2cm of the area after immersing in 0.1 M KOH for even three days. It shows that the thickening TiO_2 protection layer can effectively reduce the number of pin-holes, and it could be beneficial for protecting PEC devices. Based on the statistics, the possibility of not having any pin-hole in a PEC device is calculated with assumptions that 0.2 cm^2 of reaction area and the pin-holes are evenly distributed over the surface. The probability of not having a pin-hole in a PEC device is shown as the red data points in Figure 5.16. The axis scale is the log of probability, thus, for example, 0 represents that the surface is free from pin-holes and -2 represents that there is 1 % of probability of having a protection layer without any pin-holes. The error bars in the probability graph are calculated from the error bars in the number of pin-holes using the same method used for the average value. The mean values show that 50, 250 and 1100 nm of the TiO_2 protection layer will provide a pin-hole free device with 10^{-6} %, 1 % and 100

% of probability. This statistic implies that most of the sputter deposited TiO_2 protection layers in room temperature would be likely to have a random number of pin-holes, leading to a large variance in their stability test.

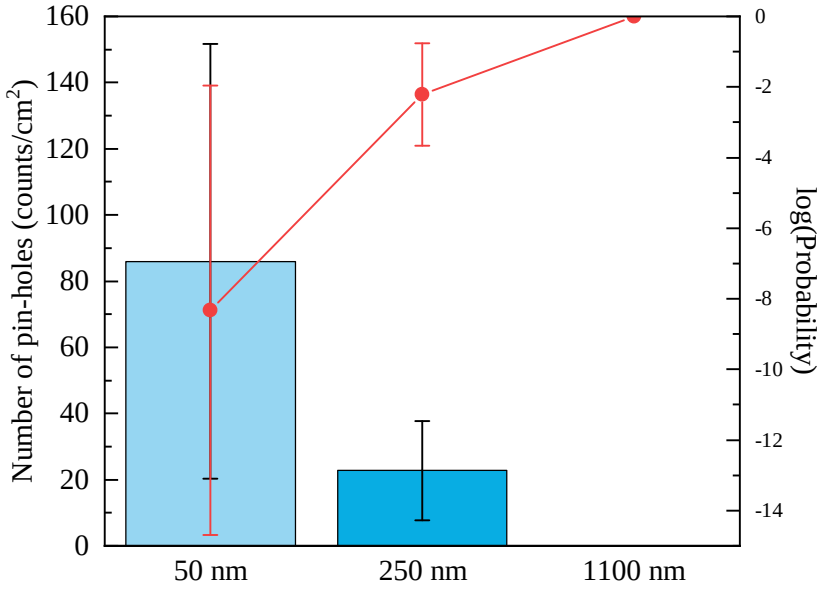

Figure 5.16: Statistics on the number of pin-holes. The bar plots show the number of pin-holes counted by SEM images. The error bars are acquired from randomly chosen five places in SEM. The red plots shows the probability of having a pin-hole free device.

5.4.3 The stability of PEC devices depending on the thickness of the protection layer

The stability of PEC device with 1350 nm TiO_2 protection layer (deposited by ALD 150 nm + sputter 1200 nm) is tested by chronoamperometry and compared with the tests (which are randomly among many stability tests) with the thinner protection layers (deposited by ALD or sputter) in Figure 5.17. The thickness of the thinner protection layers ranges from 100 nm to 360 nm and shows a substantial variance in its stability (from 1 to 40 hours), but there is not any clear dependence on the thickness (Figure 5.17A). For example, while the most stable data (green) is from a device with 100 nm of TiO_2, a device with 360 nm of TiO_2 shows 8 hours of operation time (red). However, when the thickness of the protection layer is increased to 1350 nm, all of the devices are running around 50 hours, and the variance between the devices is much smaller. Such improved and regular stability test results would be related to the removal of pin-holes by thickening the protection layer shown in Figure 5.15. A random number of pin-holes in the thin protection layers results in a considerable variance in the stability test. On the other hand, pin-hole free devices with the thick protection layer regularly fail at $\sim$ 50 hours operation,

and it implies that the device failure mechanism would be different from the devices with the thin protection layers.

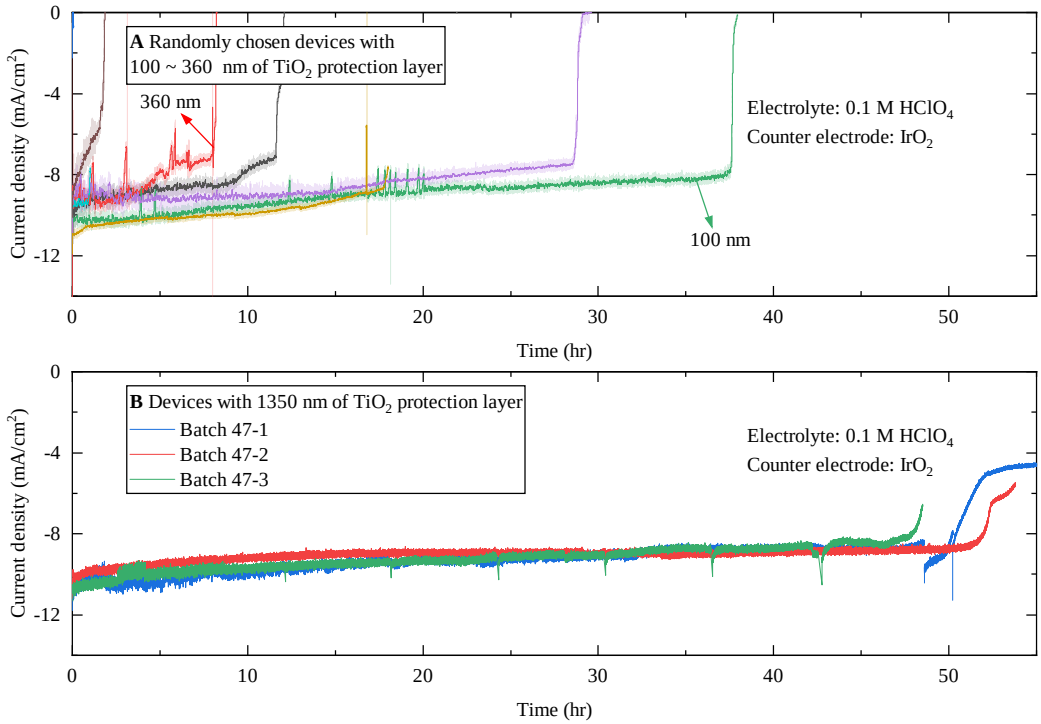

Figure 5.17: Stability test on PEC devices with (A) a relatively thinner protection layer (100 $\sim$ 360 nm) and (B) a thick protection layer (1350 nm).

To figure out the corrosion mechanism of PEC device with the thick protection layer (deposited by ALD 150 nm + sputter 1200 nm), the surface of the PEC devices are observed by SEM after operation for $\sim$ 53 hours (denoted as Batch 47-2 in Figure 5.17 (B)) and $\sim$ 70 hours (denoted as Batch 47-1 in Figure 5.17 (B)) and shown in Figure 5.18. After $\sim$53 hours of operation, when the devices begin to lose its activity, the surface of the PEC device shows many cracks all over the surface. It could probably be from proton intercalation into TiO_2 protection layer. Over the long operation, platinum catalysts over TiO_2 protection layer could be contaminated and lose their activity. Then protons that cannot evolve to hydrogen could intercalate into TiO_2 protection layer. The proton-intercalated TiO_2 protection layer could be unstable due to mechanical stress from lattice parameter expansion or hydrogen evolution inside of the protection layer. Eventually, the sputter-deposited TiO_2 layer is detached from the surface after $\sim$ 70 hours of operation, and ALD deposited TiO_2 layer is opened. At this point, only a small portion of the sputtered TiO_2 layer survives (mostly along the perimeter of the reaction area). Inset in Figure 5.18B is a tilted view on the remaining sputtered layer showing the thickness of sputter-deposited TiO_2.

In the case of the sample denoted as Batch 47-3, cyclic voltammetry is carried out every 6 hours to observe its change during the stability test, as shown in Figure 5.19. Because

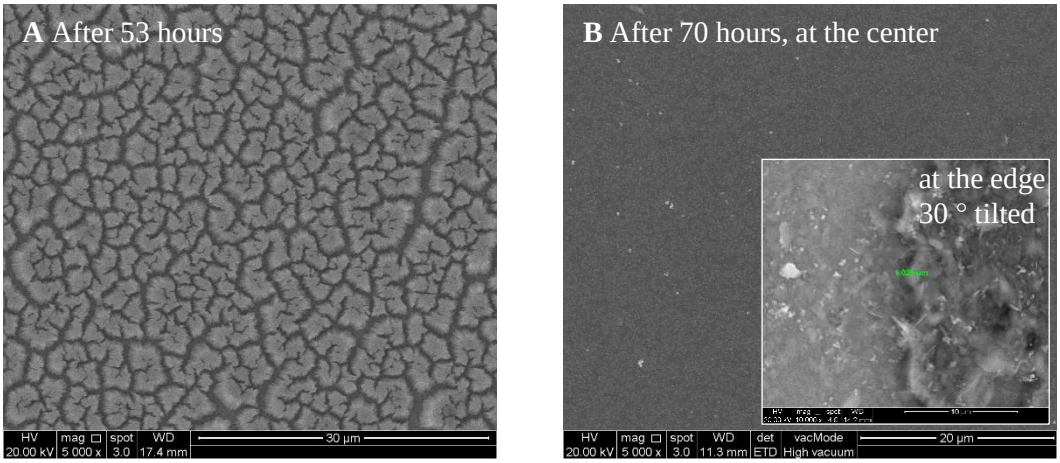

Figure 5.18: The surface of PEC devices covered with thick TiO_2 protection layer observed by SEM. (A) Crack appears on the surface after 53 hours of operation. (B) After 70 hours, sputter deposited thick TiO_2 protection layer is delaminated. Inset figure in (B) shows tilted view ($\sim$ 30 °) on the remaining part of the thick protection layer.

the stability test is carried out in 2 electrode setup, the x-axis scale is the potential versus IrO_2 counter electrode. The cyclic voltammetry shows that the photocurrent density slowly decreases over time, while the photovoltage remains more or less the same. It could potentially be from the deactivation of platinum catalyst or parasitic absorption due to contamination.

5.4.4 Further improvement by UV-light illumination

Although thickening the protection layer brings significant improvement in the stability of the device by removing pin-hole, it seems that there is another mechanism that deteriorates the performance of PEC devices with the thick protection layer. As discussed in the previous section, the deactivation mechanism could be relevant to catalyst contamination over a long operation time. Therefore, UV-light is illuminated during stability tests at open circuit potential to improve stability further. Under UV-light illumination, it is expected that high energy electron-hole pairs are generated from TiO_2 and could potentially oxidize contaminants sitting on the surface. The spectrum of UV-light for cleaning the surface is shown in Figure 5.20A. The cyclic illumination of the UV-light for cleaning and the light source for water-splitting (simulating AM 1.5G spectrum) is carried out initially. UV light is illuminated for 30 min every 12 hours of operation under the light source for 12 cycles, and then the light source is continuously illuminated (Figure 5.20B).

The stability test with the thick TiO_2 protection layer (1350 nm) is carried out with the cyclic UV-light illumination for cleaning (Figure 5.20B) and the result is shown in Figure 5.21. The current density from this specific device is smaller than other devices in this thesis because a relatively larger amount of Pt catalyst is deposited (nominally 3 nm) because it might help deactivation by Pt catalyst contamination. The PEC device operated 15.8 days, and the H_2-lifetime reached 847 ml/cm^2. To the best of my knowledge, the operation time and H_2-lifetime is the best record among PEC devices tested under 1 Sun

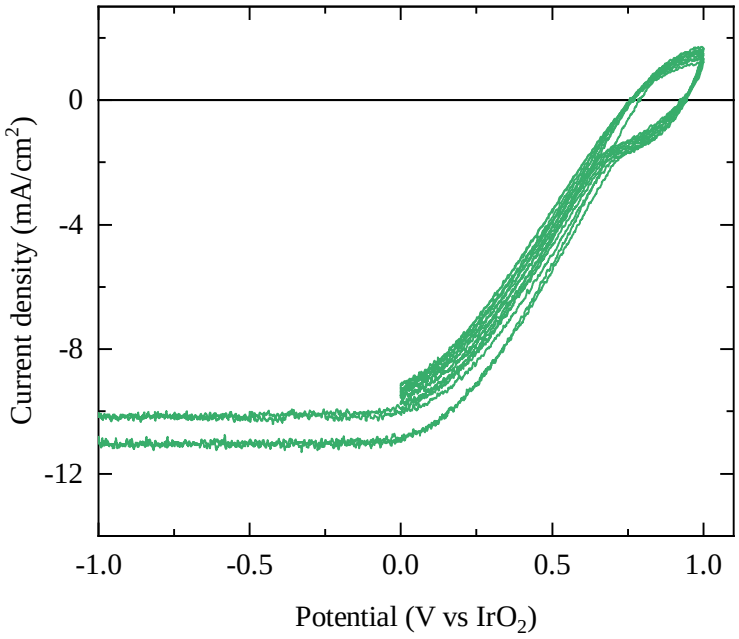

Figure 5.19: Cyclic voltammetry of Batch47-3 measured during its stability test.

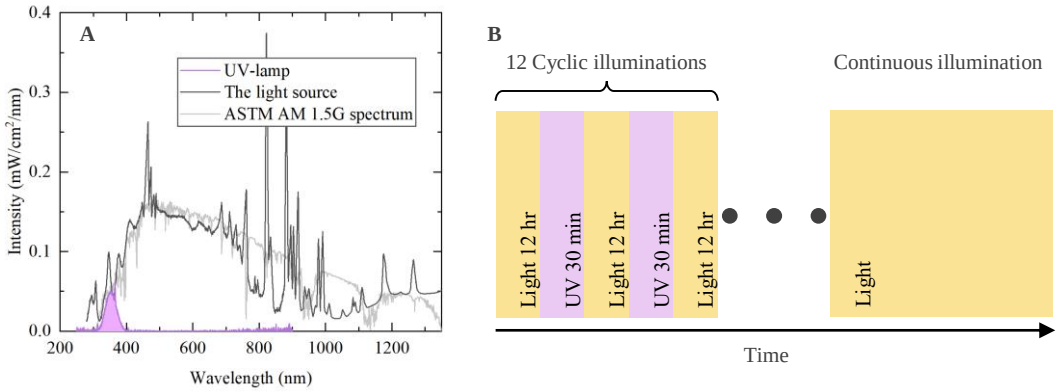

Figure 5.20: UV-light illumination for cleaning PEC device during the stability test. (A) The spectrum of the UV lamp is used for cleaning the PEC device with the thick TiO_2 protection layer. (B) 12 cyclic illumination (12 hours of the standard light source + 30 min of the UV-light) and the continuous illumination of the light source is carried out.

illumination. The inset of Figure 5.21 shows a small increment in the current density after UV-light illumination. After 378 hours of operation, the surface of the device shows the similar cracking and delamination of the sputter-deposited TiO_2 protection layer shown in Figure 5.18.

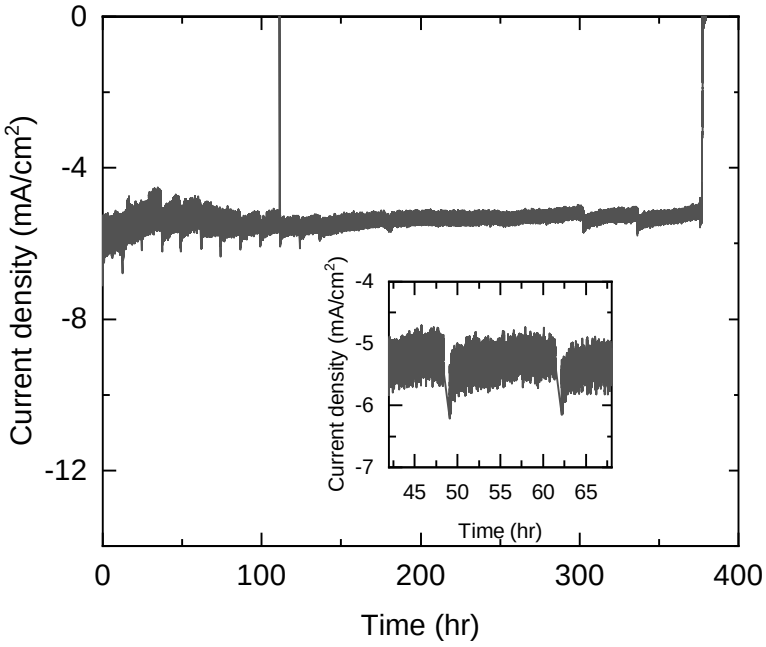

Figure 5.21: The stability test with a thick protection layer and UV cleaning.

5.5 Benchmarking the stability based on H_2-lifetime

Ben-Naim et al.[56] suggested H_2-lifetime as a figure of merit that indicates the stability of a PEC device and reviewed publications on unassisted solar water splitting device. To emphasize the importance of gas collection during the stability test, the literature review on H_2-lifetime is categorized by three different experimental methods, as shown in Figure 5.22: Charge collection from wired devices, Gas collection and Gas collection from only wireless devices. In the case of wired charge collection (Figure 5.22A), the total amount of charge passed over the lifetime of a device is collected, and the charge is converted into an equivalent amount of hydrogen assuming that all of the charges participate in the water-splitting reaction with 100 % of faraday efficiency. However, as discussed in section 5.1, charge collection may not be a rigorous way to evaluate the stability of the PEC device. Therefore, experiments which are collecting gaseous products are isolated in Figure 5.22B. The blue and red data points represent the amount of hydrogen and oxygen collected over the lifetime of the PEC device. Please note that the y-axis scale for hydrogen (left) is scaled by 0.5 compared to that for oxygen (right), therefore when hydrogen and oxygen are produced in stoichiometric ratio (2:1), red and blue data points from the same measurement are overlapping each other. Lastly, wireless device, which

would be the most interesting structure (see discussions on the section 2.3.1). The data points in Figure 5.22 are also summarized in Table A.1.

The square data points in Figure 5.22 represents the results of this thesis. Even though gaseous products are not collected, the stability test with the thick protection layer shows these plots shows shows H_2-lifetime measured in this study. The data points are

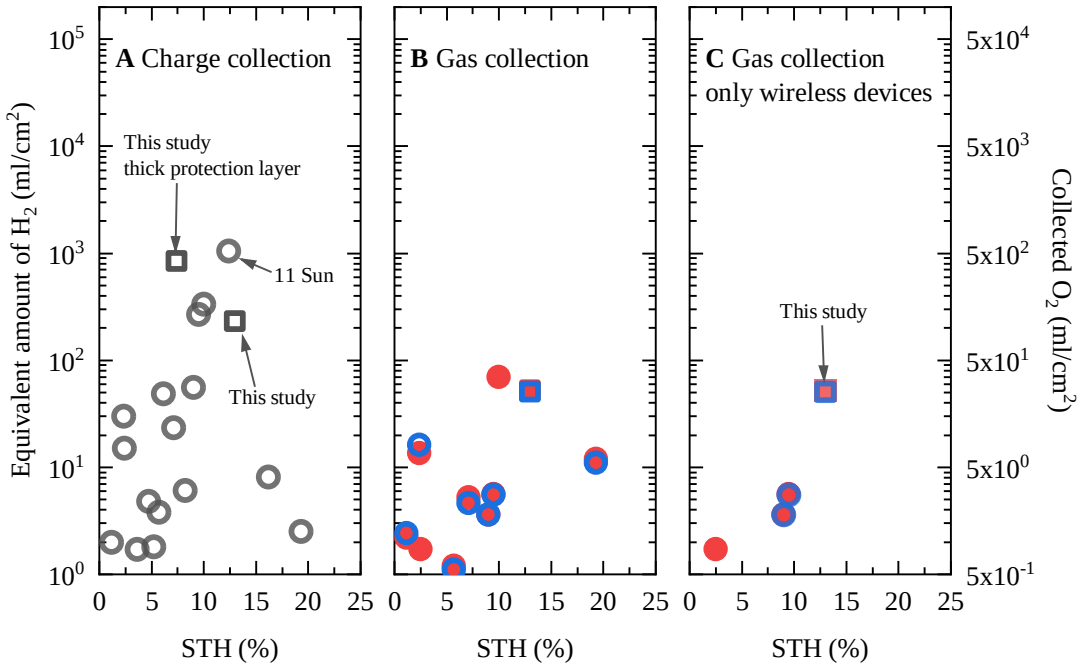

Figure 5.22: The benchmark on the stability tests on PEC devices.

CHAPTER 6

Conclusion and Outlook

In this thesis, PEC devices made of III-V triple junction solar cell protected by TiO_2 protection layer are characterized in the wired and wireless configuration. In this chapter, major results in this thesis are reviewed in the respect of the questions arisen at the end of chapter 2.

6.1 STH efficiency of PEC is still less than theoretical maximum (unlike PV+EC)

The state of art PEC devices are showing smaller STH efficiency compared to PV+EC made of the same photoabsorber and catalysts. In the case of the state-of-art PEC devices, the lower efficiency is mainly originated from optical loss by reflection because PEC lacks a good anti-reflective coating.

In this study, TiO_2 protection layer serves as monolayer anti-reflective coating. Depending on the thickness of the protection layer, the current density from each junction is characterized in actual PEC operating condition (not in dry air) by adding additional light sources to the experimental setup. The current density from each junction shows dependence on the thickness of TiO_2 layer because the monolayer of TiO_2 changes the reflection of PEC device. The optical loss by reflection depending on the various TiO_2 thicknesses are further characterized by both measurement and calculation to clarify the loss mechanism of the specific PEC device. More importantly, this investigation also shows that the spectrum range where the monolayer TiO_2 can minimize the reflection is not wide enough to cover entire spectrum range for the III-V solar cell used in this study. When considering that tandem solar cells absorb a broad range of spectrum to maximize efficiency, PEC devices protected by a monolayer of TiO_2, which is widely used as a protection layer, would not be able to reach the theoretical maximum STH efficiency.

Therefore, developing a protection layer which can minimize the reflection over a broad range of spectrum would be the essential part of future studies in PEC. With reference to conventional solar cells, one of the most promising approach would be using multi-layer anti-reflective coating. In the case of dry conventional III-V solar cell, multi-layer struc-

tures, such as MgF_2/SiO_2 or other combination of materials, bring significant improvement in their performance by reducing the reflection loss over a broad range. In the case of PEC, a design requirements for multilayer anti-reflective coating is more demanding compared to a dry solar cell, because the anti-reflective coating has to be stable in electrolyte and conduct charge carriers. While TiO_2 satisfies the requirements, at least one more material whose refractive index is different from TiO_2 is necessary for preparing the multilayer anti-reflective coating for a PEC device. Potentially, n-type large band gap materials such as niobium oxide or tungsten oxide could satisfy the requirements, or doping TiO_2 with dopants could modify the refractive index of TiO_2. Future study for improving the activity of PEC device would require similar kind of approach.

6.2 PEC devices have a poor stability in electrolyte

Poor stability of PEC devices in electrolyte has been considered as the most critical problem in PEC. Although silicon based PEC devices shows reasonably good stability in acid because of native SiO_2 oxide layer (inbetween protection layer and Si photoabsorber), other solar cell materials such as III-V elements or perovoskite are not able to operate sufficiently long time. The poor stability of PEC devices are from imperfect protection layers which are usually having pin-holes and allows contact between a semiconductor and electrolyte. This thesis tries to deliver two important message on the stability issue in PEC.

The first message is that the stability of PEC devices should be tested rigorously by collecting both hydrogen and oxygen products. The stability of PEC devices are often measured by only chronoamperometry, however, the current density may not be always from the water-splitting reaction, but also other miscelleneous reactions like the corrosion of device or underpotential deposition. One of the experiment carried out with both charge collection and gas collection shows that these two measurement may not be always the same. Therefore, we collect hydrogen and oxygen during the stability test to show more pertinent way to do a stability test.

The second message is that pin-holes in the TiO_2 protection layer, which is causing the poor stability of PEC devices, can be removed by thickening the protection layer thickness without deteriorating a device performance. Thin TiO_2 protection layers whose thickness is thinner than 400 nm shows a large variance in the stability of PEC devices because of a random number of pin-holes distributed over the surface of PEC devices. However, after thickening the protection layer more than 1100 nm, the stability of PEC devices shows a significant enhancement to show more than 50 hours of operation without a significant corrosion in 0.1 M $HClO_4$. Furthermore, the stability of PEC devices becomes regular, and this implies that the problem originated from randomly distributed pin-holes are resolved. After resolving the pin-hole problem by thickening the protection layer, it is found that the next problem that is limiting the stability is the stability of the thick TiO_2, which is cracking after a long-therm experiment. The following study on the thick protection layer shows that the cracking issue could be resoved by UV-light illumination on the PEC device.

References

1. Unitd Nations Framework Convention on Climate Change. *Adoption of the Paris Agreement* Paris, 2015.
2. IEA. *CO_2 emissions from fuel combustion 2019* Paris, 2019.
3. IEA. *Electricity Information 2019* Paris, 2019.
4. EIA. *Monthly Energy Review, March 2020* Washington, DC, 2020.
5. Acree, W. E. J. & Chickos, J. S. *NIST Chemistry WebBook, NIST Standard Reference Database Number 69* Gaithersburg MD, 2020.
6. IEA. *The future of hydrogen* Paris, 2019.
7. IEA, A.-T. Survey on the Number of Fuel Cell Vehicles, Hydrogen Refueling Stations and Targets. *Advanced Fuel Cells IEA Technology Collaboration Programme,* 1–7 (2019).
8. IPHE. *Initiatives, Programs, and Policies*
9. ITF. *ITF Transport Outlook 2019* Paris, 2019.
10. IEA. *Renewable heat policies* Paris, 2018.
11. IEA. *Technology Roadmap - Hydrogen and Fuel Cells* Paris, 2015.
12. IEA. *Technology Roadmap - Energy Storage* Paris, 2014.
13. Deloitte. *Energy storage: Tracking the technologies that will transform the power sector* 2015.
14. DNV-GL. *Energy transition Outlook 2019* 2019.
15. Deloitte. *Australian and Global Hydrogen Demand Growth Scenario Analysis COAG Energy Council – National Hydrogen Strategy Taskforce* 2019.
16. ACIL Allen Consulting. Opportunities for Australia from Hydrogen Exports, 1–114 (2018).
17. Rostrup-Nielsen, J. R. *Catalytic Steam Reforming* (eds Anderson, J. R. & Boudart, M.) 1–117 (Springer, Berlin, 1984).
18. Basile, A., Liguori, S. & Iulianelli, A. *Membrane reactors for methane steam reforming (MSR)* **2,** 31–59 (Elsevier Ltd, 2015).
19. Iulianelli, A. *et al. Water gas shift membrane reactors* 3–29 (Elsevier Ltd, 2015).
20. Wang, H., Dong, X. & Lin, Y. S. *Membrane reactors for hydrogen production from coal* 145–186 (Elsevier Ltd, 2015).
21. Lee, D.-Y., Elgowainy, A. A. & Dai, Q. *Life Cycle Greenhouse Gas Emissions of Byproduct Hydrogen from Chlor-Alkali Plants* tech. rep. (Argonne National Laboratory (ANL), Argonne, IL (United States), Dec. 2017).
22. Lakshmanan, S. & Murugesan, T. The chlor-alkali process: Work in Progress. *Clean Technologies and Environmental Policy* **16,** 225–234 (Feb. 2014).

23. Buttler, A. & Spliethoff, H. Current status of water electrolysis for energy storage, grid balancing and sector coupling via power-to-gas and power-to-liquids: A review. *Renewable and Sustainable Energy Reviews* **82,** 2440–2454 (Feb. 2018).
24. IRENA. *Hydrogen: a Renewable Energy Perspective* **September** (2019).
25. IEA. *Tracking Energy Integration* tech. rep. (IEA, Paris, 2019).
26. Ayers, K. Gigawatt-scale renewable hydrogen via water splitting as a case study for collaboration: The need to connect fundamental and applied research to accelerate solutions. *MRS Energy and Sustainability* **4,** E11 (Sept. 2017).
27. Carmo, M., Fritz, D. L., Mergel, J. & Stolten, D. A comprehensive review on PEM water electrolysis. *International Journal of Hydrogen Energy* **38,** 4901–4934 (Apr. 2013).
28. Dincer, I. & Joshi, A. S. *Solar Based Hydrogen Production Systems* 141 S. (Springer New York, New York, NY, 2013).
29. Jia, J. *et al.* Solar water splitting by photovoltaic-electrolysis with a solar-to-hydrogen efficiency over 30%. *Nature Communications* **7,** 13237 (Dec. 2016).
30. Dispenza, G. *et al.* Development of a solar powered hydrogen fueling station in smart cities applications. *International Journal of Hydrogen Energy* **42,** 27884–27893 (Nov. 2017).
31. Nørskov, J. K., Bligaard, T., Rossmeisl, J. & Christensen, C. H. Towards the computational design of solid catalysts. *Nature Chemistry* **1,** 37–46 (2009).
32. Seh, Z. W. *et al.* Combining theory and experiment in electrocatalysis: Insights into materials design. *Science* **355,** eaad4998 (Jan. 2017).
33. Montoya, J. H. *et al.* Materials for solar fuels and chemicals. *Nature Materials* **16,** 70–81 (Jan. 2017).
34. Scott, S. B. Isotope-Labeling Studies in Electrocatalysis for Renewable Energy Conversion. *Ph.D. thesis* (2019).
35. Bernardi, M. & Grossman, J. C. Computer calculations across time and length scales in photovoltaic solar cells. *Energy and Environmental Science* **9,** 2197–2218 (2016).
36. Shockley, W. & Queisser, H. J. Detailed Balance Limit of Efficiency of p⁻n Junction Solar Cells. *Journal of Applied Physics* **32,** 510–519 (1961).
37. Rühle, S. Tabulated values of the Shockley–Queisser limit for single junction solar cells. *Solar Energy* **130,** 139–147 (June 2016).
38. Woodhouse, M., Smith, B., Ramdas, A. & Margolis, R. *Crystalline Silicon Photovoltaic Module Manufacturing Costs and Sustainable Pricing : 1H 2018 Benchmark and Cost Reduction Road Map* tech. rep. February (National Renewable Energy Laboratory, Golden, CO, 2019).
39. Bae, D., Seger, B., Vesborg, P. C. K., Hansen, O. & Chorkendorff, I. Strategies for stable water splitting via protected photoelectrodes. *Chemical Society Reviews* **46,** 1933–1954 (2017).

40. Hu, S. *et al.* Thin-Film Materials for the Protection of Semiconducting Photoelectrodes in Solar-Fuel Generators. *Journal of Physical Chemistry C* **119,** 24201–24228 (2015).
41. Seger, B. *et al.* Silicon protected with atomic layer deposited TiO_2: Conducting versus tunnelling through TiO_2. *Journal of Materials Chemistry A* **1,** 15089–15094 (2013).
42. Hu, S. *et al.* Amorphous TiO_2 coatings stabilize Si, GaAs, and GaP photoanodes for efficient water oxidation. *Science* **344,** 1005–1009 (2014).
43. Qiu, J. *et al.* Microscopic Study of Atomic Layer Deposition of TiO_2 on GaAs and Its Photocatalytic Application. *Chemistry of Materials* **27,** 7977–7981 (2015).
44. Mei, B. *et al.* Crystalline TiO_2: A Generic and Effective Electron-Conducting Protection Layer for Photoanodes and -cathodes. *Journal of Physical Chemistry C* **119,** 15019–15027 (2015).
45. Yu, Y. *et al.* Enhanced photoelectrochemical efficiency and stability using a conformal TiO_2 film on a black silicon photoanode. *Nature Energy* **2** (2017).
46. Bae, D. *et al.* Carrier-selective p- and n-contacts for efficient and stable photocatalytic water reduction. *Catalysis Today* **290,** 59–64 (2017).
47. Bae, D., Seger, B., Hansen, O., Vesborg, P. C. & Chorkendorff, I. Durability Testing of Photoelectrochemical Hydrogen Production under Day/Night Light Cycled Conditions. *ChemElectroChem* **6,** 106–109 (2019).
48. Bae, D. *et al.* Protection of Si photocathode using TiO_2 deposited by high power impulse magnetron sputtering for H_2 evolution in alkaline media. *Solar Energy Materials and Solar Cells* **144,** 758–765 (Jan. 2016).
49. Yao, X. *et al.* Scale-Up of $BiVO_4$ Photoanode for Water Splitting in a Photoelectrochemical Cell: Issues and Challenges. *Energy Technology* **6,** 100–109 (Jan. 2018).
50. Dilger, S., Trottmann, M. & Pokrant, S. Scaling Up Electrodes for Photoelectrochemical Water Splitting: Fabrication Process and Performance of 40 cm^2 $LaTiO_2N$ Photoanodes. *ChemSusChem* **12,** 1931–1938 (2019).
51. Turan, B. *et al.* Upscaling of integrated photoelectrochemical water-splitting devices to large areas. *Nature Communications* **7,** 1–9 (2016).
52. Haussener, S. *et al.* Modeling, simulation, and design criteria for photoelectrochemical water-splitting systems. *Energy and Environmental Science* **5,** 9922–9935 (2012).
53. Shaner, M. R., Atwater, H. A., Lewis, N. S. & McFarland, E. W. A comparative technoeconomic analysis of renewable hydrogen production using solar energy. *Energy and Environmental Science* **9,** 2354–2371 (2016).
54. Pinaud, B. A. *et al.* Technical and economic feasibility of centralized facilities for solar hydrogen production via photocatalysis and photoelectrochemistry. *Energy and Environmental Science* **6,** 1983–2002 (2013).
55. *https://www.energy.gov/eere/fuelcells/doe-technical-targets-hydrogen-production- photoelectroch water-splitting*

56. Ben-Naim, M. *et al.* Addressing the Stability Gap in Photoelectrochemistry: Molybdenum Disulfide Protective Catalysts for Tandem III-V Unassisted Solar Water Splitting. *ACS Energy Letters* **5,** 2631–2640 (Aug. 2020).
57. Strobl, G. F. X. *et al. ABOUT AZUR'S "3G30-advanced" SPACE SOLAR CELL AND NEXT GENERATION PRODUCT WITH 35% EFFICIENCY* tech. rep. (AZUR SPACE Solar Power GmbH, 2012).
58. Lieberman, A. M. & Lichtenberg, A. J. *Principles of Plasma Discharges and Materials Processing* 2nd ed. (John Wiley & Sons, Inc., Hoboken, New Jersey, 2005).
59. Behrisch, R. & Eckstein, W. *Topics in applied physics, volume 110, Sputtering by Particle Bombardment* (Springer, Berlin, Heidelberg, 2007).
60. George, S. M. Atomic layer deposition: An overview. *Chemical Reviews* **110,** 111–131 (2010).
61. Singh, J. & Wolfe, D. E. Nano and macro-structured component fabrication by electron beam-physical vapor deposition (EB-PVD). *Journal of Materials Science* **40,** 1–26 (2005).
62. Madou, M. J. *Fundamentals of microfabrication : the science of miniaturization* 2nd ed. (CRC Press, Boca Raton, FL, 2002).
63. Herman, M. A., Richter, W. & Sitter, H. *Epitaxy: Physical Principles and Technical Implementation* (eds Hull, R., Parisi, J., Osgood, R. M. & Warlimont, H.) (Springer, Berlin, Heidelberg, 2004).
64. American Welding Society. *Brazing Manual* 3rd ed., 309 (American Welding Society, 1976).
65. Sahari, S. K. *et al.* Native oxidation growth on Ge(111) and (100) surfaces. *Japanese Journal of Applied Physics* **50** (2011).
66. ASTM International. *Standard Tables for Reference Solar Spectral Irradiances: Direct Normal and Hemispherical on 37° Tilted Surface* tech. rep. (West Conshohocken, PA, 2012).
67. Wolf, E. *Principles of Optics* 7 Ed. (Cambridge University Press, Cambridge, 2003).
68. Pulker, H. K., Paesold, G. & Ritter, E. Refractive indices of TiO_2 films produced by reactive evaporation of various titanium–oxygen phases. *Applied Optics* **15,** 2986 (1976).
69. Schubert, M. *et al.* Optical constants of $Ga_xIn_{1-x}P$ lattice matched to GaAs. *Journal of Applied Physics* **77,** 3416 (1995).
70. Rakić, A. D. & Majewski, M. L. Modeling the optical dielectric function of GaAs and AlAs: Extension of Adachi's model. *Journal of Applied Physics* **80,** 5909–5914 (1996).
71. Hale, G. M. & Querry, M. R. Optical Constants of Water in the 200 nm to 200 μm Wavelength Region. *Applied Optics* **12,** 555 (1973).
72. Brickwedde, L. H. Properties of aqueous solutions of perchloric acid. *Journal of Research of the National Bureau of Standards* **42,** 309 (1949).

73. Napoli, L., Franco, J., Fasoli, H. & Sanguinetti, A. Conductivity of Nafion 117 membrane used in polymer electrolyte fuel cells. *International Journal of Hydrogen Energy* **39,** 8656–8660 (2014).
74. Cheng, W. H. *et al.* Monolithic Photoelectrochemical Device for Direct Water Splitting with 19% Efficiency. *ACS Energy Letters* **3,** 1795–1800 (2018).
75. Döscher, H., Geisz, J. F., Deutsch, T. G. & Turner, J. A. Sunlight absorption in water-efficiency and design implications for photoelectrochemical devices. *Energy and Environmental Science* **7,** 2951–2956 (2014).
76. Langford, V. S., McKinley, A. J. & Quickenden, T. I. Temperature dependence of the visible-near-infrared absorption spectrum of liquid water. *Journal of Physical Chemistry A* **105,** 8916–8921 (2001).
77. Praprotnik, M., Janezic, D. & Mavri, J. Temperature dependence of water vibrational spectrum: A molecular dynamics simulation study. *Journal of Physical Chemistry A* **108,** 11056–11062 (2004).
78. Hale, G. M. & Querry, M. R. Optical Constants of Water in the 200nm to 200μm Wavelength Region. *Applied Optics* **12,** 555 (1973).
79. Barrigón, E., Espinet-González, P., Contreras, Y. & Rey-Stolle, I. Implications of low breakdown voltage of component subcells on external quantum efficiency measurements of multijunction solar cells. *Progress in Photovoltaics: Research and Applications* **23,** 1597–1607 (Nov. 2015).
80. Babaro, J. P., West, K. G. & Hamadani, B. H. Spectral response measurements of multijunction solar cells with low shunt resistance and breakdown voltages. *Energy Science and Engineering* **4,** 372–382 (2016).
81. Barrigón, E., Espinet-González, P., Contreras, Y. & Rey-Stolle, I. Why can't I measure the external quantum efficiency of the Ge subcell of my multijunction solar cell? *AIP Conference Proceedings* **1679,** 050002 (2015).
82. Meusel, M. *et al.* Spectral Response Measurements of Monolithic GaInP/Ga(In)As/Ge Triple-Junction Solar Cells: Measurement Artifacts and their Explanation. *Progress in Photovoltaics: Research and Applications* **11,** 499–514 (2003).
83. Kornblum, L. *et al.* Solar hydrogen production using epitaxial $SrTiO_3$ on a GaAs photovoltaic. *Energy and Environmental Science* **10,** 377–382 (2017).
84. Tan, J. *et al.* Fullerene as a Photoelectron Transfer Promoter Enabling Stable TiO_2-Protected Sb_2Se_3 Photocathodes for Photo-Electrochemical Water Splitting. *Advanced Energy Materials* **9,** 1–12 (2019).
85. Seger, B. *et al.* Using TiO_2 as a conductive protective layer for photocathodic H_2evolution. *Journal of the American Chemical Society* **135,** 1057–1064 (2013).
86. Liang, J. *et al.* A thin-film silicon based photocathode with a hydrogen doped TiO_2 protection layer for solar hydrogen evolution. *Journal of Materials Chemistry A* **4,** 16841–16848 (2016).
87. Laursen, A. B. *et al.* MoS_2 - An integrated protective and active layer on n^+p^-Si for solar H_2 evolution. *Physical Chemistry Chemical Physics* **15,** 20000–20004 (2013).

88. Kast, M. G., Enman, L. J., Gurnon, N. J., Nadarajah, A. & Boettcher, S. W. Solution-deposited F:SnO_2/TiO_2 as a base-stable protective layer and antireflective coating for microtextured buried-junction H_2-evolving Si photocathodes. *ACS Applied Materials and Interfaces* **6,** 22830–22837 (2014).
89. Ji, L. *et al.* A silicon-based photocathode for water reduction with an epitaxial $SrTiO_3$ protection layer and a nanostructured catalyst. *Nature Nanotechnology* **10,** 84–90 (2015).
90. Fan, R. *et al.* Stable and efficient multi-crystalline n^+p silicon photocathode for H_2 production with pyramid-like surface nanostructure and thin Al2O3 protective layer. *Applied Physics Letters* **106,** 2–6 (2015).
91. Britto, R. J. *et al.* Molybdenum Disulfide as a Protection Layer and Catalyst for Gallium Indium Phosphide Solar Water Splitting Photocathodes. *Journal of Physical Chemistry Letters* **7,** 2044–2049 (2016).
92. Benck, J. D. *et al.* Designing active and stable silicon photocathodes for solar hydrogen production using molybdenum sulfide nanomaterials. *Advanced Energy Materials* **4,** 1–8 (2014).
93. Chen, Y. W. *et al.* Atomic layer-deposited tunnel oxide stabilizes silicon photoanodes for water oxidation. *Nature Materials* **10,** 539–544 (2011).
94. Choi, M. J. *et al.* Long-term durable silicon photocathode protected by a thin Al_2O_3/SiO_x layer for photoelectrochemical hydrogen evolution. *Journal of Materials Chemistry A* **2,** 2928–2933 (2014).
95. Gu, J. *et al.* Water reduction by a p-$GaInP_2$ photoelectrode stabilized by an amorphous TiO_2 coating and a molecular cobalt catalyst. *Nature Materials* **15,** 456–460 (2016).
96. Kainthla, R. C., Zelenay, B. & Bockris, J. Protection of n-Si Photoanode against Photocorrosion in Photoelectrochemical Cell for Water Electrolysis. *Journal of The Electrochemical Society* **133,** 248 (1986).
97. Zhang, L. *et al.* Durable hydrogen evolution from water driven by sunlight using (Ag,Cu)$GaSe_2$ photocathodes modified with CdS and $CuGa_3Se_5$. *Chemical Science* **6,** 894–901 (2015).
98. Zhang, Z. *et al.* Carbon-layer-protected cuprous oxide nanowire arrays for efficient water reduction. *ACS Nano* **7,** 1709–1717 (2013).
99. Zheng, J. *et al.* Crystalline TiO_2 protective layer with graded oxygen defects for efficient and stable silicon-based photocathode. *Nature Communications* **9,** 1–10 (2018).
100. Azevedo, J. *et al.* Tin oxide as stable protective layer for composite cuprous oxide water-splitting photocathodes. *Nano Energy* **24,** 10–16 (2016).
101. Bae, D. *et al.* Protection of Si photocathode using TiO_2 deposited by high power impulse magnetron sputtering for H_2 evolution in alkaline media. *Solar Energy Materials and Solar Cells* **144,** 758–765 (2016).

102. Reece, S. Y. *et al.* Wireless Solar Water Splitting Using Silicon-Based Semiconductors and Earth-Abundant Catalysts. *Science* **334,** 645–648 (Nov. 2011).
103. Verlage, E. *et al.* A monolithically integrated, intrinsically safe, 10% efficient, solar-driven water-splitting system based on active, stable earth-abundant electrocatalysts in conjunction with tandem III-V light absorbers protected by amorphous TiO2 films. *Energy and Environmental Science* **8,** 3166–3172 (2015).
104. Varadhan, P., Fu, H.-C., Kao, Y.-C., Horng, R.-H. & He, J.-H. An efficient and stable photoelectrochemical system with 9% solar-to-hydrogen conversion efficiency via InGaP/GaAs double junction. *Nature Communications* **10,** 5282 (Dec. 2019).
105. Young, J. L. *et al.* Direct solar-to-hydrogen conversion via inverted metamorphic multi-junction semiconductor architectures. *Nature Energy* **2,** 1–8 (2017).
106. Kainthla, R. C. Significant Efficiency Increase in Self-Driven Photoelectrochemical Cell for Water Photoelectrolysis. *Journal of The Electrochemical Society* **134,** 841 (1987).
107. Khaselev, O. & Turner, J. A. A monolithic photovoltaic-photoelectrochemical device for hydrogen production via water splitting. *Science* **280,** 425–427 (1998).
108. Kelly, N. A. & Gibson, T. L. Design and characterization of a robust photoelectrochemical device to generate hydrogen using solar water splitting. *International Journal of Hydrogen Energy* **31,** 1658–1673 (2006).
109. Brillet, J. *et al.* Highly efficient water splitting by a dual-absorber tandem cell. *Nature Photonics* **6,** 824–828 (2012).
110. Abdi, F. F. *et al.* Efficient solar water splitting by enhanced charge separation in a bismuth vanadate-silicon tandem photoelectrode. *Nature Communications* **4,** 1–7 (2013).
111. Han, L. *et al.* Efficient Water-Splitting Device Based on a Bismuth Vanadate Photoanode and Thin-Film Silicon Solar Cells. *ChemSusChem* **7,** 2832–2838 (2014).
112. Shi, X. *et al.* Unassisted photoelectrochemical water splitting beyond 5.7% solar-to-hydrogen conversion efficiency by a wireless monolithic photoanode/dye-sensitised solar cell tandem device. *Nano Energy* **13,** 182–191 (2015).
113. Gurudayal *et al.* Perovskite-Hematite Tandem Cells for Efficient Overall Solar Driven Water Splitting. *Nano Letters* **15,** 3833–3839 (2015).
114. Sun, K. *et al.* A Stabilized, Intrinsically Safe, 10% Efficient, Solar-Driven Water-Splitting Cell Incorporating Earth-Abundant Electrocatalysts with Steady-State pH Gradients and Product Separation Enabled by a Bipolar Membrane. *Advanced Energy Materials* **6,** 1–7 (2016).
115. Shi, X. *et al.* Unassisted photoelectrochemical water splitting exceeding 7% solar-to-hydrogen conversion efficiency using photon recycling. *Nature Communications* **7** (2016).

APPENDIX A

Table of stability benchmark data

Year	STH (%)	H_2 (mL/cm^2) charge collection	H_2 (mL/cm^2) gas collection	O_2 (mL/cm^2) gas collection	Author	Ref.
1987	8.2	6.1			Kainthla	[106]
1998	12.4	1044.6			Khaselev	[107]
2015	2.3	29.9			Kelly	[108]
2011	4.7	4.8			Reece	[102]
2011	2.5			0.85	Reece	[102]
2012	1.17	2	2.4	1.1	Brillet	[109]
2013	3.6	1.7			Abdi	[110]
2014	5.2	1.8			Han	[111]
2015	9.5	267.4	5.5	2.8	Verlage	[103]
2015	5.7	3.8	1.1	0.6	Shi	[112]
2015	2.4	15	16.2	6.8	Gurudayal	[113]
2016	10	334.3		35	Sun	[114]
2016	7.1	23.4	4.6	2.6	Shi	[115]
2017	16.2	8.1			Young	[105]
2018	19.3	2.5	11	6	Cheng	[74]
2019	9	56	3.6	1.8	Varadhan	[104]
2020	6.1	49			Ben-Naim	[56]

Table A.1: The data points shown in Figure 5.22.

APPENDIX B

Appended publication

Paper I

Wireless photoelectrochemical water splitting using triple junction solar cell protected by TiO_2

Choongman Moon, Brian Seger, Peter C. K. Vesborg, Ole Hansen and Ib Chorkendorff

Cell Reports Physical Science, accepted

Wireless photoelectrochemical water splitting using triple junction solar cell protected by TiO_2

Choongman Moon[1], *Brian Seger*[1], *Peter Christian Kjærgaard Vesborg*[1], *Ole Hansen*[2], *Ib Chorkendorff*[1,3]

Summary

Photoelectrochemical (PEC) water splitting devices replace electrical contacts in a solid-state solar cell with solid/liquid junction to improve the solar-to-hydrogen conversion efficiency and reduce system cost. Wireless configuration can fully utilize the advantage of the PEC by removing all electrical contacts, however, wired configuration with the electrical contact on its backside has been widely studied to facilitate device characterization. In this study, the wireless PEC water splitting device made of a commercially available III-V triple-junction solar cell protected by transparent TiO_2 is demonstrated with high efficiency and stability. The wireless device produces both H_2 and O_2 products in a stoichiometric ratio in 13 % of solar-to-hydrogen conversion efficiency over ~ 12 hours, and the total amount of H_2 product during its lifetime reaches 51 ml/cm^2, which is the highest value reported from wireless PEC devices.

Keywords

Photoelectrochemistry, Water electrolysis, Hydrogen production, Catalysts, Multi-junction

---

[1] *Department of Physics, Technical University of Denmark, 2800 Lyngby, Denmark*

[2] *DTU Nanolab, Technical University of Denmark, 2800 Lyngby, Denmark*

[3] *Lead Contact: ibchork@fysik.dtu.dk*

solar cell, TiO_2 protection layer, Stability test for PEC devices.

Introduction

Photoelectrochemical (PEC) water splitting has been studied over decades as a potential pathway to emission-free hydrogen production.[1,2] The PEC device is made up of a water electrolyzer integrated onto the surface of a solar cell, and photocurrent generated from the solar cell participates in the water splitting reaction on the surface immediately. There have been discussions and techno-economic analyses comparing PEC with electrically wiring separate water electrolyzer and solar cell[3–5], suggesting that PEC might open the possibility of efficiency improvement and cost reduction by the nature of its device structure. Because the water splitting reaction takes place directly on the solar cell over the large surface area, the low current density flows over a very short distance and it results in a low ohmic loss and improved efficiency. Furthermore, PEC does not require power electronics and other intermediary components to combine a solar cell and a water electrolyzer, which would be beneficial for lowering system cost. Shaner et al. conducted a techno-economic analysis on PEC[5] and pointed out that PEC could find economic feasibility, especially when using III-V solar cells with solar concentrators.[6]

PEC devices have mostly been characterized by measuring the photocurrent in a wired configuration in most of the PEC studies. In the wired configuration, one side of the solar cell is connected to an electrical wire or transparent conductive oxide (TCO) while the other side is exposed to an electrolyte. Because of the experimental convenience of current measurement, this wired configuration has become the typical method to investigate the performance. Nevertheless, the advantage of PEC can only be fully realized in a wireless configuration which

exposes both sides of the solar cell. The wireless configuration can shorten the current flowing distance dramatically because the photocurrent needs to flow only over the thickness of the solar cell. Furthermore, the wireless configuration can potentially reduce a system cost by making a stand-alone device without any external components and wiring.[7–9] In spite of the advantages of the wireless configuration, it has not been pursued widely because of difficulties in characterizing the wireless device. The performance of the wireless device can only be measured by capturing gaseous products in an electrochemical cell with a membrane and tubing without crossover or leakage of the products. The electrochemical cell also needs an elaborate design to minimize the ohmic loss from the proton transport. Moreover, it is more challenging to stabilize a wireless device because both sides of the solar cell are exposed to an electrolyte. Reece et al. realized PEC water splitting in the wireless configuration using a silicon-based triple-junction solar cell with 2.5 % solar-to-hydrogen (STH) conversion efficiency.[7]

There have been many efforts to improve the stability of PEC in the wired configuration because of the aforementioned experimental convenience[10–31], but the stability is often evaluated without analyzing the gaseous product.[11,13–17,19,21,24,25,27] The stability is thus only assessed by the evolution of the current density over a certain period assuming that the faradaic efficiency is 100 %. However, it is pertinent to be cautious with these results because the current density might be due to unexpected reactions[32], such as corrosion of solar cells rather than water electrolysis, especially for the anodic half-reaction. Therefore, directly capturing both H_2 and O_2 over the lifetime of the PEC device (H_2-lifetime) is a more reliable approach to examining stability. According to Ben-Naim et al.[13], the H_2-lifetime of PEC devices has to reach at least 100 L/cm^2 to achieve economic feasibility. However, currently there is still about two orders of magnitude difference between the current state of the art PEC and this goal.

In this work, we investigated wireless solar water splitting using a III-V triple-junction solar

cell. The cell is made of GaInP/GaAs/Ge junctions with varying bandgaps (1.8/1.4/0.7 eV) to absorb photons with different energies. This triple-junction solar cell fully utilizes the entire solar spectrum including the infrared region and is able to supply sufficient photovoltage for unassisted solar water splitting. We investigated the PEC devices in both wired and wireless configurations to present the following features: 1) We demonstrate a highly active PEC water splitting device in the wireless configuration by using the III-V triple-junction solar cell.[7] 2) We also test the PEC device in the wired configuration for further characterization. We investigated the effect of the water layer thickness and the TiO_2 protection layer thickness on the performance of PEC devices. 3) The wireless PEC devices show reasonably good stability in acid by protecting the front side with a transparent TiO_2 layer[33,34] and backside with a thick Ti film. When testing the stability of the wireless device, both H_2 and O_2 products are collected to assure that the cathode and anode are occupied by hydrogen (HER) and oxygen evolution reactions (OER), not by other miscellaneous reactions. This PEC device demonstrates 13 % of STH efficiency and shows the highest durability among the wireless PEC devices by achieving an H_2-lifetime of 51 ml/cm^2. Furthermore, we then discuss the corrosion mechanism of this specific device and potential approaches to enhance stability.

Results

The configuration of the PEC devices

The experimental set up used for testing the wireless device is depicted in Figure 1A. The solar cell used in this study is purchased from AZUR SPACE Solar Power GmbH. The compression cell is designed to expose the front side and backside of the solar cell to an acidic electrolyte for HER and OER, respectively. The proton transport distance around the solar cell

is minimized to lower the ohmic loss, and a Nafion membrane separates the gaseous products. Due to the sensitive nature of the triple-junction solar cell, both sides of the solar cell require a protection layer for stable operation in an acidic environment, and they also need electrocatalysts for an efficient water splitting. Over the optical front side of the solar cell, a thin layer of metallic Ti (3 nm) is sputtered as an adhesion layer and followed by the deposition of TiO_2 protection layer with various thicknesses as shown in Figure 1B.[33,34] Pt nanoparticles with 0.5 nm of nominal thickness is deposited on the TiO_2 protection layer as a HER catalyst. The opposing Ge backside requires a highly robust protection layer because the anodic potential needed for OER (~ 1.8 V vs RHE) creates a highly corrosive environment. To resolve this, we covered the Ge backside with 10 nm of Au as an electrical contact and a 2 μm thick Ti layer as a protection layer as shown in Figure 1C. On top of the protection layer, 10 nm of IrO_2 is deposited as an OER catalyst. A 10 nm layer allows for a continuous TiO_2-IrO_2 interface without the presence of the electrolyte. This approach results in an ohmic contact rather than a Schottky-barrier or an electrolyte induced depletion layer developing in the TiO_2. This layer is on the back non-irradiated side, thus allowing the Ti/TiO_2/IrO_2 to be as thick as necessary without needing to consider any issues relating to optical absorption.

The wired samples have the same structure with the exception that a Cu wire is attached to the Au layer using Ag paste instead of the 2 μm thick Ti and IrO_2 layer. The entire sample is covered by epoxy except for an opening area in the middle of the front side (~ 0.2 cm^2). Further details about the preparation are described in the Experimental Procedures section.

The thickness of the TiO_2 protection layer and water layer affect the activity of the PEC devices

The photocurrent from the triple-junction solar cell is limited by the junction with the lowest current density, therefore, it is important to match the photocurrent from each junction to be similar. In the PEC design, the Ge bottom junction is based off of infrared light absorption, and the light is filtered not only by the two cells in front of the Ge cell but also by the water layer in front of the stack. According to the previous theoretical study[35], the water layer has preferential absorption in the infrared light, thus it could deteriorate the activity of the Ge bottom junction and mismatch the photocurrent from each junction. To analyze if infrared absorption by water can result in the Ge bottom cell to be the current limiting cell in the triple-junction stack, we varied the thickness of the water layer in front of the PEC device and monitored performance. The water layer thickness is controlled to be 2, 4 or 8 ± 0.5 mm, and J-V curves are measured under Xenon lamp with AM 1.5G filter imitating ASTM 1.5G spectrum (see Figure S1A) as shown in Figure 2A. The J-V curve shows a maximum fill factor of 89 % when the water layer thickness is around 2 ± 0.5 mm. However, the fill factor decreases to 82 % and 71 % as the water layer thickness increases to 4 ± 0.5 mm and 8 ± 0.5 mm, respectively. The change of J-V curve is dominated by two different factors[36–38], 1) the current density limitation by the Ge bottom junction due to the reduced infrared irradiance, and 2) the diode behavior of Ge bottom junction in the breakdown region. At the higher potential range (~ 1.5 V vs RHE), the increased water layer thickness reduces the infrared light intensity by absorption and the current density from Ge bottom junction decreases. 4 ± 0.5 mm or 8 ± 0.5 mm of the water layer is able to decrease the current density. However, the current density increases again at the lower potential range (~ 0 V vs RHE). The Ge bottom junction is a p-n diode under electrical bias, and the total electrical bias applied on the Ge bottom junction is the sum of external bias from a potentiostat and the photovoltages from the top and middle junction in this PEC experiment. The direction of the external bias and photo voltages are forward and

reverse to the p-n junction, respectively. When the external bias is small (~ 0 V vs RHE), the total electrical bias on the Ge diode is in the reverse direction and surpasses the breakdown voltage of Ge diode. In this case, the Ge bottom junction does not limit the current density, thus the top or middle junction will be limiting the current density. In order to test the hypothesis, we illuminated with an additional infrared light by using a tungsten halogen lamp filtered by a silicon wafer. The bandgap of Si (1.1 eV) allows additional intensity only for the Ge bottom junction (since $h\nu < 1.1$ eV). When supplying this additional infrared intensity to the device with 8 ± 0.5 mm of the water layer, the fill factor recovers and this confirms that Ge bottom junction is limiting the current density at the higher potential range (~ 1.5 V vs RHE) in this case.

The photocurrent density of multi-junction solar cell is always limited by the junctions with the lowest current density. Therefore, determining the current limiting junction, and if possible, figuring out the current density from each junction would be valuable information for optimizing a PEC device as it has been done for conventional multi-junction solar cells.[39,40] As shown in Figure 2A, increasing the current density from the Ge bottom junction by supplying the additional intensity in the infrared range cannot make the total current density larger than 11.3 mA/cm^2, which means that the top or middle junction is limiting the current density to this value. To determine the current limiting junction, we added an additional light source for either top or middle junction to the experimental setup. The additional light source's purpose is to supply photons for one of the junctions exclusively, and the current density should increase when the photons for the current limiting junction is supplied from the additional light source. We use an additional Xenon lamp with optical filters to illuminate only the top junction (blue light, 400 ~ 500 nm) and the middle junction (red light, 645 ~ 900 nm) (see Figure S1B). We measured the photocurrent density of the wired PEC devices with various TiO_2 thicknesses

(see Figure S2), and two devices with 165 nm and 220 nm of TiO_2 are shown as representative examples in the grey graph Figures 2B and C. The blue and red graphs in Figure 2B and C show the photocurrent density when turning on and off the additional blue and red light, respectively. Both PEC devices with 165 nm and 220 nm of TiO_2 are showing improved current density when supplying more photons for the GaInP top junction, and this indicates that the top junction is the current limiting junction. The current density under the additional blue light is not changed in the range of blue light intensity used in this study (see Figure S3 for details). This result implies that the intensity of the additional blue light is large enough to fully saturate the GaInP top junction so that the top junction is not the current limiting junction under the blue light anymore. Furthermore, the blue light intensity is not too high to invoke a detectable amount of photoluminescence coupling effect.[41]

Under the blue light illumination where the top junction is not limiting, the middle or bottom junction should be the current limiting junction. However, we can exclude the bottom junction and thus know that the middle junction is the current limiting junction based on the fill factor. As shown in Figure 2A, the current limiting bottom junction can decrease the current density only at ~ 1.5 V vs RHE, while the current density at the lower potential range remains the same. However, when considering that the current density under the blue light (the blue graphs in Figure 2B and C) shows the same current density at 0.5 V vs RHE and 1.5 V vs RHE, the cyclic voltammetry measurement shows a clear difference from the PEC device with the current limiting bottom junction. Therefore, the current density under the blue light should show the current density from the middle junction. It is noteworthy to observe that the current density from the middle junction clearly differs for the two thicknesses of the TiO_2 layer. The middle junction current density from the PEC device with 165 nm and 220 nm of TiO_2 are 11.8 mA/cm^2 and 13.2 mA/cm^2, respectively. To explain the thickness dependence, the reflectance

of PEC devices with various TiO_2 thickness is measured in the visible light range in air (see Figure S4), and two representative devices with 165 nm and 220 nm of TiO_2 are shown in Figure 2D. As the TiO_2 thickness changes, the reflectance of PEC devices also changes, and will affect the photocurrent density from each junction.[42] Because the device with 165 nm of TiO_2 has a more significant reflection in the wavelength range for the middle junction (650 ~ 900 nm) compared to the device with 220 nm of TiO_2, it has a lower current density from the middle junction.

To quantify the effect of TiO_2 thickness on the reflectance and the current density, the expected photocurrent density from each junction is calculated by taking into consideration the spectral intensity of the light source provided by the supplier, absorption by the water layer[43], optical properties of materials[44–46] and internal quantum efficiency derived from the measured external quantum efficiency and reflectance. The thickness of the water layer, which significantly affects the current density from the bottom junction, is assumed to be 2 mm. Further details regarding the current density calculation are described in the supplementary information (see Note S1). The purple, green and yellow lines in Figure 2E represent the calculated current densities from the top, middle and bottom junction, respectively. The periodic changes of the calculated current density over the TiO_2 thickness are from the optical interference inside of the TiO_2 film. When the thickness of the TiO_2 layer satisfies Equation 1, destructive interference will occur for the reflecting wave and the TiO_2 protection layer will work as an antireflective coating[47]:

$$d = \left(\frac{1}{4} + \frac{1}{2}m\right)\frac{\lambda}{n} \quad (1)$$

where d, m, λ and n represent TiO_2 thickness, any integer number, the wavelength of light in vacuum and the refractive index of TiO_2, respectively. This equation shows that the periodic

change of the expected current density over TiO_2 thickness depends on the wavelength corresponding to each junction. Because the wavelength of light absorbed from each junction increases in the order of top, middle and bottom junction, the periodicity also increase in the same order as shown in the solid lines in Figure 2E.

The calculated current density from each junction is compared to the experimental measurement. According to the calculation results shown in Figure 2E (solid lines), the GaInP top junction is expected to limit the current density for all TiO_2 thicknesses according to the calculation result because the junction with the lowest current density will limit the current density of entire PEC devices. We measured photocurrent density from PEC devices with various TiO_2 thicknesses (see Figure 2B, C and Figure S2) and confirmed the current limiting junction by using the additional light sources. As expected from the calculation, all PEC devices with the various TiO_2 thicknesses are showing improved current density under the blue light, which means that the top junction is limiting the current density. The measured current density from all PEC devices are shown in Figure 2E. The purple data points are measured without the additional blue light, while the green data points are measured with the blue light. Because the PEC devices show improved current density when adding the additional blue light, which is exciting only the top junction, the top junction is the current limiting junction for all devices. Therefore, as explained with Figure 2B and C, the purple data points without the blue light represent the current density from the top junction. Also, because the cyclic voltammetry with the additional blue light does not show the characteristic behavior of the bottom junction limiting device (shown in Figure 2A), the green data points represent the current density from the middle junction. All data points with error bars are acquired by measuring three independent PEC devices with the corresponding TiO_2 thickness. The measured and calculated current densities from each junction are in accordance with each other. It shows that the current

density from each junction in a multi-junction solar cell can be measured with additional light sources, which would be useful information for optimizing a PEC device.

The current density from the PEC device is limited by the top junction, and it is related to the device's design and optical losses. The triple-junction solar cell used in this study is optimized to operate under AM 0 spectrum with 17.0 mA/cm^2 of current density, however, this study uses the light source simulating AM 1.5G spectrum. The difference between AM 0 and AM 1.5G spectrum results in the current limiting top junction generating 13.6 mA/cm^2. There seem to be parasitic losses, which reduces the current density by less than 1 mA/cm^2, possibly from optical absorption by Pt catalyst, TiO_2 protection layer and metallic Ti adhesion layers. The device without any reflection would generate 12.6 mA/cm^2, but the loss by reflection results in 10.0 ~ 12.1 mA/cm^2 of current density from the top junction, as shown in Figure 2E.

The stability of the PEC devices is tested by capturing gaseous products over its lifetime

The stability of PEC devices is often evaluated by conducting chronoamperometry over a certain period. Figure 3A shows the H_2-lifetime from selected works[8,22,42,48–57] (circle) as well as this study (rectangle) measured by the total amount of charge passed. (see Table S1 for details) The unit of the charge passed (Coulombs) is converted to an equivalent amount of hydrogen for a more relatable figure of merit. The most stable device from this study has 277 nm of the TiO_2 protection layer and produced 231 ml/cm^2 supposing that all of the charges are participating in the water splitting reaction as depicted in the inset of Figure 3A. However, a large amount of total passed charge does not necessarily mean that the photoelectrode is producing hydrogen and oxygen. As pointed out by the previous study[32], the current density may originate from dissolution of semiconductors or other non water

splitting reactions. Therefore, we isolated the data points which collected the gas product among the references in Figure 3A and showed these more thorough experiments in Figure 3B. The volume of collected H_2 and O_2 is depicted as the blue and red data points, respectively, with the H_2 data point corresponding to the left y-axis scale and the O_2 evolution data points corresponding to the right y-axis scale. We emphasize that the H_2 axis is scaled by a factor of 1/2 compared to the O_2 scale, thus if the H_2:O_2 ratio is the theoretical value of 2, the H_2 and O_2 data points should be on top of each other. This scaling allows to easily see whether a given device was truly splitting water or the extent to which a corrosion reaction or something else was involved. The square data point represents the wireless PEC device with 355 nm of TiO_2 from this study (see supplemental video). The STH efficiency of the device is 13 % based on the amount of gas collected during the first 1 hour of the operation (inset of Figure 3C). The activity of the wireless device is almost the same as that of the wired device in this lab-scale experiment with a small current. The advantage of a wireless device by reducing ohmic loss from electron conduction would be more substantial at a larger-scale device with a larger current. The H_2-lifetime reaches 51 ml H_2/cm^2, and the ratio between H_2 and O_2 is 2:1 in the range of significant figures of eudiometers (graduation size: 50 µl), which shows that HER and OER are dominant reactions. Figure 3C collects data points from wireless devices only. As we mentioned before, the wireless configuration would be the simplest configuration possible for PEC and, therefore, attractive for a practical application. To the best of our knowledge, this is the highest value measuring isolated hydrogen and oxygen gas among the wireless devices evaluated in an acidic environment.

After stability tests, we investigated the corrosion mechanism of this specific PEC device. It was discovered that wireless samples have severe corrosion only on the front side (i.e. cathode), whereas the backside (i.e. anode) does not show any observable corrosion. This is

probably because a 2 μm Ti film is sufficiently thick to prevent the formation of any pin-holes which might otherwise lead to local corrosion. On the other hand, the corrosion on the front side was clearly observed through SEM and EDS. In the initial stages of corrosion, the PEC devices usually show dark spots in SEM, as shown in Figure 4A. Those spots are typically around 0.1 ~ 1 μm size and have lower indium and phosphorus signals and higher arsenic signals in EDS (Figure 4C). The EDS data implies that the GaInP top junction corrodes partially in the spots, leaving the GaAs middle junction exposed. This corrosion could be related to the decrease in current density and photovoltage (see Figure S5 for details) by losing some part of the top junction. In the later stage of corrosion (Figure 4B, D, E, F, and G), the acidic electrolyte reaches and begins to dissolve the GaAs middle junction. In addition, cracks appear surrounding the initial corrosion spot, possibly because of the faster etch rate of GaAs compared to that of GaInP. X-ray photoelectron spectroscopy (XPS) measurements before and after the stability test show the deposition of dissolved materials (see Figure S6). After the stability test, the arsenic peak is much larger than the phosphorus peak, and it also supports the different etch rates between the GaInP top junction and GaAs middle junction. Figure 4H and I depict the suggested corrosion process. In Figure 4H, the initial corrosion takes place due to a pin-hole in the protection layer. As the corrosion gets large, the acidic electrolyte contacts the GaAs middle junction which is more vulnerable to acid than GaInP and wide areas underneath the top junction are dissolved. It causes cracks along the crystalline orientation of the top junction surrounding the initial corrosion spot, and the cracks eventually lead to delamination.

Discussion

Further improvement of the PEC device would be possible by having less reflection in the broad range of wavelength for all junctions. The TiO_2 protection layer used in this study works as a monolayer antireflective coating, which is not suitable for reducing the reflection over a broad spectral range. Anti-reflection in a broad range could be achieved by using a bilayer or multilayer structure made of two materials with different refractive indexes just as the antireflective coating used for conventional solar cells. A certain combination of transparent, conductive and acid-stable materials could be used for the purpose. Such materials could be prepared by, for example, adding dopants to or changing the crystallinity of TiO_2. A careful control on the thickness of multilayer made of such materials can lower the reflectance of the protection layer.

An ideal protection layer for the cathodic side of a PEC device should be stable, transparent, conductive and impermeable to electrolyte.[58] Sputtered or ALD TiO_2 is a large bandgap n-type material whose conduction band is aligned closely with the hydrogen redox potential.[29,59] These properties make TiO_2 suitable for the electron-conducting protection layer for photocathodes. However, TiO_2 prepared by sputter or ALD is not entirely impermeable to an electrolyte because of pin-holes in the protection layer. We presume that the pin-holes are created by either the grain boundary of TiO_2 or small dust particles sitting on the surface before TiO_2 deposition.

There are potential strategies suggested to improve the stability of PEC devices. For example, pin-holes in the protection layer could be reduced or eliminated by improving film quality. Our previous study showed that high power impulse magnetron sputtering (HiPIMS) can deposit TiO_2 thin film with higher mass density compared to a DC magnetron sputtering, which reduces the size and number of pin-holes in TiO_2 protection layers. This improves the stability of silicon photocathodes tested in KOH significantly. Similarly, epitaxial deposition of the protection layer could improve stability by removing pin-holes and preventing any

contact with electrolyte.[21,26]

Experimental Procedures

1) Resource availability

Lead Contact

Further information and requests for resources and materials should be directed to and will be fulfilled by the Lead Contact, Ib Chorkendorff (ibchork@fysik.dtu.dk).

Materials Availability

This study did not generate new unique materials.

Data and Code Availability

The experimental data and calculation code generated in this study are available from the Lead Contact upon request.

2) PEC device preparation

We prepared the PEC devices in an ISO Class 5 cleanroom to reduce contamination during the preparation. The solar cell used in this study is purchased from AZUR SPACE Solar Power GmbH. As-purchased wafers were cleaned by sonication in ethanol and water for 2 minutes each, rinsing in 1 M HCl for 2 minutes and water for 5 minutes. The backside of the solar cell (p-Ge substrate) is cleaned by Ar sputtering once more and covered with 10 nm of Au in a sputter chamber to provide an electrical contact. Au is chosen as the contact layer because Au will form an ohmic contact with p-type Ge by Fermi level pinning nearby to the valence band

edge of Ge[60–62], and would not be oxidized during sample preparation. After the Au deposition, 2 μm of Ti is deposited on top of the Au layer using an e-beam evaporator. Before the deposition on the front side, the wafer is treated in a mixture of citric acid solution (50 wt%) and hydrogen peroxide (30 %) in 5 : 1 ratio for 3 minutes.[63] The front side of the solar cell is covered by 3 nm of metallic Ti and the controlled thickness of TiO_2 deposited at 250 °C using ALD. The wafer is diced using a diamond saw. In order to prevent damage to the solar cell junctions, the cutting starts from the backside of the wafer (Ge substrate), and the depth of cutting is 80 μm, which is around half of the total thickness of the wafer (150 μm). The tessellated wafer is cleaved into small pieces (1 cm^2). Before doing PEC experiments, 0.5 nm of Pt and 10 nm of IrO_2 are deposited on the front and backside of the sample as HER and OER catalysts, respectively.

The preparation procedure for a wired sample is the same as the wireless sample until Au deposition. After Au deposition, the wafer is diced into small pieces (1 cm^2). Then the Ti, TiO_2 and Pt layers are deposited successively using a sputter deposition with a shadow mask to prevent deposition of materials on the edge-side of the wafer. The backside covered by the Au layer is connected to a Cu wire using Ag paste. The Cu wire and the wafer is encapsulated in a glass tube and epoxy (Loctite Hysol 1C) with an opening area in the front side (~ 0.2 cm^2). The Cu wire leads to a counter electrode, which is prepared by soaking an Au mesh into 1 mM $IrCl_3$ and annealed in air at 400 °C.

3) Characterization

The light source used in this study is a Xenon lamp with AM 1.5G filter (Oriel). The spectral intensity of the light source is measured using a spectrophotometer (Ocean Optics Inc,

USB4000-UV-vis). We calibrated the light intensity integrated over the detectable wavelength range to be the same as the standard AM 1.5G spectrum in the same range (68.4 mW/cm^2 in 300 ~ 900 nm, see Figure S1A). The reflectance and thickness of the TiO_2 films are measured by ellipsometry, and the surface morphology is observed using scanning electron microscopy (SEM) and energy dispersive x-ray spectroscopy (EDS).

The wired devices are investigated in a three-electrode setup. The electrolyte is 0.1 M $HClO_4$, (pH 1) the OER counter electrode is IrO_2 deposited on a gold mesh, and the reference electrode is Hg/Hg_2SO_4. The stability of the wired samples is examined by chronoamperometry at 0 V vs IrO_2. The performance of the wireless samples is measured in a compression cell filled with 1 M $HClO_4$. (pH 0) The design of the compression cell is depicted in Figure 1A. The compression cell is a two-compartment cell separated by Nafion 117 membrane. The electrolyte in H_2 and O_2 compartments is saturated by H_2 and O_2, respectively. The surface area of the PEC device opened to the electrolyte is 0.2 cm^2, and the thickness of the water layer is kept to around 1 mm to minimize the loss by infrared absorption. The ohmic resistance inside of the cell is measured to be 48 ohms (see Figure S7A), and it will lead to 90 ~ 100 mV of ohmic voltage drop. Each compartment has a connection to a eudiometer (graduation size: 50 μl, total volume: 25 ml) for capturing gas products. Before testing samples in the compression cell, the sample surface is cleaned with oxygen plasma in a vacuum chamber and kept under UV light in air to remove organic contamination. The cleaning process makes surface hydrophilic and facilitates bubble removal through the shallow water layer. We also carried out a leak test to determine the loss by leakage or crossover of the product by using a thin eudiometer (graduation size: 10 μl, total volume: 1 ml). The expected amount of products from 0.2 cm^2 of the active area is around 1 ml of H_2 and 0.5 ml of O_2 over 1 hour, and this leakage is found to be less than 1 % of the expected amount of products (~ 10 and ~ 5 μl/hr for H_2 and

O_2 compartment each).

Acknowledgement

The Center for Surface Physics and Catalysis is funded by the Villum Foundation V-SUSTAIN Grant 9455.

Author contribution

C.M. carried out device preparation, characterization and calculation. B.S., P.C.K.V., O.H. and I.C. conceived the concept and co-wrote the paper. All authors contributed to the discussion and interpretation of the results.

Declaration of interest

The authors declare no competing interests.

References

1. Walter, M.G., Warren, E.L., McKone, J.R., Boettcher, S.W., Mi, Q., Santori, E.A., and Lewis, N.S. (2010). Solar water splitting cells. Chem. Rev. *110*, 6446–6473.

2. Bae, D., Seger, B., Vesborg, P.C.K., Hansen, O., and Chorkendorff, I. (2017). Strategies for stable water splitting via protected photoelectrodes. Chem. Soc. Rev. *46*, 1933–1954.

3. Ardo, S., Fernandez Rivas, D., Modestino, M.A., Schulze Greiving, V., Abdi, F.F., Alarcon Llado, E., Artero, V., Ayers, K., Battaglia, C., Becker, J.P., et al. (2018). Pathways to electrochemical solar-hydrogen technologies. Energy Environ. Sci. *11*, 2768–2783.

4. Pinaud, B.A., Benck, J.D., Seitz, L.C., Forman, A.J., Chen, Z., Deutsch, T.G., James,

B.D., Baum, K.N., Baum, G.N., Ardo, S., et al. (2013). Technical and economic feasibility of centralized facilities for solar hydrogen production via photocatalysis and photoelectrochemistry. Energy Environ. Sci. *6*, 1983–2002.

5. Shaner, M.R., Atwater, H.A., Lewis, N.S., and McFarland, E.W. (2016). A comparative technoeconomic analysis of renewable hydrogen production using solar energy. Energy Environ. Sci. *9*, 2354–2371.

6. Dumortier, M., and Haussener, S. (2015). Design guidelines for concentrated photo-electrochemical water splitting devices based on energy and greenhouse gas yield ratios. Energy Environ. Sci. *8*, 3069–3082.

7. Reece, S.Y., Hamel, J.A., Sung, K., Jarvi, T.D., Esswein, A.J., Pijpers, J.J.H., and Nocera, D.G. (2011). Wireless solar water splitting using silicon-based semiconductors and earth-abundant catalysts. Science *334*, 645–648.

8. Verlage, E., Hu, S., Liu, R., Jones, R.J.R., Sun, K., Xiang, C., Lewis, N.S., and Atwater, H.A. (2015). A monolithically integrated, intrinsically safe, 10% efficient, solar-driven water-splitting system based on active, stable earth-abundant electrocatalysts in conjunction with tandem III-V light absorbers protected by amorphous TiO_2 films. Energy Environ. Sci. *8*, 3166–3172.

9. Varadhan, P., Fu, H.C., Kao, Y.C., Horng, R.H., and He, J.H. (2019). An efficient and stable photoelectrochemical system with 9% solar-to-hydrogen conversion efficiency via InGaP/GaAs double junction. Nat. Commun. *10*, 1–9.

10. Azevedo, J., Tilley, S.D., Schreier, M., Stefik, M., Sousa, C., Araújo, J.P., Mendes, A., Grätzel, M., and Mayer, M.T. (2016). Tin oxide as stable protective layer for composite cuprous oxide water-splitting photocathodes. Nano Energy *24*, 10–16.

11. Bae, D., Shayestehaminzadeh, S., Thorsteinsson, E.B., Pedersen, T., Hansen, O., Seger, B., Vesborg, P.C.K., Ólafsson, S., and Chorkendorff, I. (2016). Protection of Si photocathode using TiO_2 deposited by high power impulse magnetron sputtering for H_2 evolution in alkaline media. Sol. Energy Mater. Sol. Cells *144*, 758–765.

12. Benck, J.D., Lee, S.C., Fong, K.D., Kibsgaard, J., Sinclair, R., and Jaramillo, T.F. (2014). Designing active and stable silicon photocathodes for solar hydrogen production using molybdenum sulfide nanomaterials. Adv. Energy Mater. *4*, 1–8.

13. Ben-Naim, M., Britto, R.J., Aldridge, C.W., Mow, R., Steiner, M.A., Nielander, A.C., King, L.A., Friedman, D.J., Deutsch, T.G., Young, J.L., et al. (2020). Addressing the Stability Gap in Photoelectrochemistry: Molybdenum Disulfide Protective Catalysts for Tandem III–V Unassisted Solar Water Splitting. ACS Energy Lett. *5*, 2631–2640.

14. Britto, R.J., Benck, J.D., Young, J.L., Hahn, C., Deutsch, T.G., and Jaramillo, T.F. (2016). Molybdenum Disulfide as a Protection Layer and Catalyst for Gallium Indium Phosphide Solar Water Splitting Photocathodes. J. Phys. Chem. Lett. *7*, 2044–2049.

15. Chen, Y.W., Prange, J.D., Dühnen, S., Park, Y., Gunji, M., Chidsey, C.E.D., and McIntyre, P.C. (2011). Atomic layer-deposited tunnel oxide stabilizes silicon photoanodes for water oxidation. Nat. Mater. *10*, 539–544.

16. Choi, M.J., Jung, J.Y., Park, M.J., Song, J.W., Lee, J.H., and Bang, J.H. (2014). Long-term durable silicon photocathode protected by a thin Al_2O_3/SiO_x layer for photoelectrochemical hydrogen evolution. J. Mater. Chem. A *2*, 2928–2933.

17. Fan, R., Dong, W., Fang, L., Zheng, F., Su, X., Zou, S., Huang, J., Wang, X., and Shen, M. (2015). Stable and efficient multi-crystalline n+p silicon photocathode for H_2 production with pyramid-like surface nanostructure and thin Al_2O_3 protective layer.

Appl. Phys. Lett. *106*, 2–6.

18. Liang, J., Tan, H., Liu, M., Liu, B., Wang, N., Zhang, Q., Zhao, Y., Smets, A.H.M., Zeman, M., and Zhang, X. (2016). A thin-film silicon based photocathode with a hydrogen doped TiO_2 protection layer for solar hydrogen evolution. J. Mater. Chem. A *4*, 16841–16848.

19. Gu, J., Yan, Y., Young, J.L., Steirer, K.X., Neale, N.R., and Turner, J.A. (2016). Water reduction by a p-$GaInP_2$ photoelectrode stabilized by an amorphous TiO_2 coating and a molecular cobalt catalyst. Nat. Mater. *15*, 456–460.

20. Hu, S., Shaner, M.R., Beardslee, J.A., Lichterman, M., Brunschwig, B.S., and Lewis, N.S. (2014). Amorphous TiO$_2$ coatings stabilize Si, GaAs, and GaP photoanodes for efficient water oxidation. Science *344*, 1005–1009.

21. Ji, L., Mcdaniel, M.D., Wang, S., Posadas, A.B., Li, X., Huang, H., Lee, J.C., Demkov, A.A., Bard, A.J., Ekerdt, J.G., et al. (2015). A silicon-based photocathode for water reduction with an epitaxial $SrTiO_3$ protection layer and a nanostructured catalyst. Nat. Nanotechnol. *10*, 84–90.

22. Kainthla, R.C. (1987). Significant Efficiency Increase in Self-Driven Photoelectrochemical Cell for Water Photoelectrolysis. J. Electrochem. Soc. *134*, 841.

23. Kainthla, R.C. (1986). Protection of n-Si Photoanode against Photocorrosion in Photoelectrochemical Cell for Water Electrolysis. J. Electrochem. Soc. *133*, 248.

24. Kast, M.G., Enman, L.J., Gurnon, N.J., Nadarajah, A., and Boettcher, S.W. (2014). Solution-deposited F:SnO_2/TiO_2 as a base-stable protective layer and antireflective coating for microtextured buried-junction H_2-evolving Si photocathodes. ACS Appl.

Mater. Interfaces *6*, 22830–22837.

25. Zhang, Z., Dua, R., Zhang, L., Zhu, H., Zhang, H., and Wang, P. (2013). Carbon-layer-protected cuprous oxide nanowire arrays for efficient water reduction. ACS Nano *7*, 1709–1717.

26. Kornblum, L., Fenning, D.P., Faucher, J., Hwang, J., Boni, A., Han, M.G., Morales-Acosta, M.D., Zhu, Y., Altman, E.I., Lee, M.L., et al. (2017). Solar hydrogen production using epitaxial SrTiO3 on a GaAs photovoltaic. Energy Environ. Sci. *10*, 377–382.

27. Zheng, J., Lyu, Y., Wang, R., Xie, C., Zhou, H., Jiang, S.P., and Wang, S. (2018). Crystalline TiO_2 protective layer with graded oxygen defects for efficient and stable silicon-based photocathode. Nat. Commun. *9*, 1–10.

28. Laursen, A.B., Pedersen, T., Malacrida, P., Seger, B., Hansen, O., Vesborg, P.C.K., and Chorkendorff, I. (2013). MoS_2 - An integrated protective and active layer on n^+p-Si for solar H_2 evolution. Phys. Chem. Chem. Phys. *15*, 20000–20004.

29. Seger, B., Pedersen, T., Laursen, A.B., Vesborg, P.C.K., Hansen, O., and Chorkendorff, I. (2013). Using TiO_2 as a conductive protective layer for photocathodic H_2 evolution. J. Am. Chem. Soc. *135*, 1057–1064.

30. Tan, J., Yang, W., Oh, Y., Lee, H., Park, J., Boppella, R., Kim, J., and Moon, J. (2019). Fullerene as a Photoelectron Transfer Promoter Enabling Stable TiO_2-Protected Sb_2Se_3 Photocathodes for Photo-Electrochemical Water Splitting. Adv. Energy Mater. *9*, 1–12.

31. Zhang, L., Minegishi, T., Nakabayashi, M., Suzuki, Y., Seki, K., Shibata, N., Kubota,

J., and Domen, K. (2015). Durable hydrogen evolution from water driven by sunlight using (Ag,Cu)$GaSe_2$ photocathodes modified with CdS and $CuGa_3Se_5$. Chem. Sci. *6*, 894–901.

32. Khan, M.A., Varadhan, P., Ramalingam, V., Fu, H.C., Idriss, H., and He, J.H. (2019). Importance of oxygen measurements during photoelectrochemical water-splitting reactions. ACS Energy Lett. *4*, 2712–2718.

33. Bae, D., Shayestehaminzadeh, S., Thorsteinsson, E.B., Pedersen, T., Hansen, O., Seger, B., Vesborg, P.C.K., Ólafsson, S., and Chorkendorff, I. (2016). Protection of Si photocathode using TiO2 deposited by high power impulse magnetron sputtering for H2 evolution in alkaline media. Sol. Energy Mater. Sol. Cells *144*, 758–765.

34. Seger, B., Pedersen, T., Laursen, A.B., Vesborg, P.C.K., Hansen, O., and Chorkendorff, I. (2013). Using TiO2 as a conductive protective layer for photocathodic H2 evolution. J. Am. Chem. Soc. *135*, 1057–1064.

35. Döscher, H., Geisz, J.F., Deutsch, T.G., and Turner, J.A. (2014). Sunlight absorption in water-efficiency and design implications for photoelectrochemical devices. Energy Environ. Sci. *7*, 2951–2956.

36. Babaro, J.P., West, K.G., and Hamadani, B.H. (2016). Spectral response measurements of multijunction solar cells with low shunt resistance and breakdown voltages. Energy Sci. Eng. *4*, 372–382.

37. Barrigón, E., Espinet-González, P., Contreras, Y., and Rey-Stolle, I. (2015). Why can't I measure the external quantum efficiency of the Ge subcell of my multijunction solar cell? AIP Conf. Proc. *1679*, 050002.

38. Barrigón, E., Espinet-González, P., Contreras, Y., and Rey-Stolle, I. (2015). Implications of low breakdown voltage of component subcells on external quantum efficiency measurements of multijunction solar cells. Prog. Photovoltaics Res. Appl. *23*, 1597–1607.

39. Kirchartz, T., Rau, U., Hermle, M., Bett, A.W., Helbig, A., and Werner, J.H. (2008). Internal voltages in GaInP/GaInAs/Ge multijunction solar cells determined by electroluminescence measurements. Appl. Phys. Lett. *92*, 90–93.

40. Roensch, S., Hoheisel, R., Dimroth, F., and Bett, A.W. (2011). Subcell I-V characteristic analysis of GaInP/GaInAs/Ge solar cells using electroluminescence measurements. Appl. Phys. Lett. *98*.

41. Lim, S.H., Li, J.-J., Steenbergen, E.H., and Zhang, Y.-H. (2013). Luminescence coupling effects on multijunction solar cell external quantum efficiency measurement. Prog. Photovoltaics Res. Appl. *21*, 344–350.

42. Cheng, W.H., Richter, M.H., May, M.M., Ohlmann, J., Lackner, D., Dimroth, F., Hannappel, T., Atwater, H.A., and Lewerenz, H.J. (2018). Monolithic Photoelectrochemical Device for Direct Water Splitting with 19% Efficiency. ACS Energy Lett. *3*, 1795–1800.

43. Hale, G.M., and Querry, M.R. (1973). Optical Constants of Water in the 200 nm to 200 μm Wavelength Region. Appl. Opt. *12*, 555.

44. Pulker, H.K., Paesold, G., and Ritter, E. (1976). Refractive indices of TiO_2 films produced by reactive evaporation of various titanium–oxygen phases. Appl. Opt. *15*, 2986.

45. Rakić, A.D., and Majewski, M.L. (1996). Modeling the optical dielectric function of GaAs and AlAs: Extension of Adachi's model. J. Appl. Phys. *80*, 5909–5914.

46. Schubert, M., Gottschalch, V., Herzinger, C.M., Yao, H., G., S.P., and Woolam, J.A. (1995). Optical constants of $Ga_xIn_{1-x}P$ lattice matched to GaAs. J. Appl. Phys. *77*, 3416.

47. Born, M., and Wolf, E. (1999). Principles of Optics 7 Ed. (Cambridge University Press).

48. Brillet, J., Yum, J.H., Cornuz, M., Hisatomi, T., Solarska, R., Augustynski, J., Graetzel, M., and Sivula, K. (2012). Highly efficient water splitting by a dual-absorber tandem cell. Nat. Photonics *6*, 824–828.

49. Abdi, F.F., Han, L., Smets, A.H.M., Zeman, M., Dam, B., and Van De Krol, R. (2013). Efficient solar water splitting by enhanced charge separation in a bismuth vanadate-silicon tandem photoelectrode. Nat. Commun. *4*, 1–7.

50. Han, L., Abdi, F.F., Van De Krol, R., Liu, R., Huang, Z., Lewerenz, H.J., Dam, B., Zeman, M., and Smets, A.H.M. (2014). Efficient Water-Splitting Device Based on a Bismuth Vanadate Photoanode and Thin-Film Silicon Solar Cells. ChemSusChem *7*, 2832–2838.

51. Gurudayal, Sabba, D., Kumar, M.H., Wong, L.H., Barber, J., Grätzel, M., and Mathews, N. (2015). Perovskite-Hematite Tandem Cells for Efficient Overall Solar Driven Water Splitting. Nano Lett. *15*, 3833–3839.

52. Sun, K., Liu, R., Chen, Y., Verlage, E., Lewis, N.S., and Xiang, C. (2016). A Stabilized, Intrinsically Safe, 10% Efficient, Solar-Driven Water-Splitting Cell

Incorporating Earth-Abundant Electrocatalysts with Steady-State pH Gradients and Product Separation Enabled by a Bipolar Membrane. Adv. Energy Mater. *6*, 1–7.

53. Shi, X., Zhang, K., Shin, K., Ma, M., Kwon, J., Choi, I.T., Kim, J.K., Kim, H.K., Wang, D.H., and Park, J.H. (2015). Unassisted photoelectrochemical water splitting beyond 5.7% solar-to-hydrogen conversion efficiency by a wireless monolithic photoanode/dye-sensitised solar cell tandem device. Nano Energy *13*, 182–191.

54. Young, J.L., Steiner, M.A., Döscher, H., France, R.M., Turner, J.A., and Deutsch, T.G. (2017). Direct solar-to-hydrogen conversion via inverted metamorphic multi-junction semiconductor architectures. Nat. Energy *2*, 1–13.

55. Khaselev, O., and Turner, J.A. (1998). A monolithic photovoltaic-photoelectrochemical device for hydrogen production via water splitting. Science *280*, 425–427.

56. Kelly, N.A., and Gibson, T.L. (2006). Design and characterization of a robust photoelectrochemical device to generate hydrogen using solar water splitting. Int. J. Hydrogen Energy *31*, 1658–1673.

57. Shi, X., Jeong, H., Oh, S.J., Ma, M., Zhang, K., Kwon, J., Choi, I.T., Choi, I.Y., Kim, H.K., Kim, J.K., et al. (2016). Unassisted photoelectrochemical water splitting exceeding 7% solar-to-hydrogen conversion efficiency using photon recycling. Nat. Commun. *7*.

58. Hu, S., Lewis, N.S., Ager, J.W., Yang, J., McKone, J.R., and Strandwitz, N.C. (2015). Thin-Film Materials for the Protection of Semiconducting Photoelectrodes in Solar-Fuel Generators. J. Phys. Chem. C *119*, 24201–24228.

59. Bae, D., Pedersen, T., Seger, B., Iandolo, B., Hansen, O., Vesborg, P.C.K., and Chorkendorff, I. (2017). Carrier-selective p- and n-contacts for efficient and stable photocatalytic water reduction. Catal. Today *290*, 59–64.

60. Pavan Kishore, V., Paramahans, P., Sadana, S., Ganguly, U., and Lodha, S. (2012). Nanocrystal-based Ohmic contacts on n and p-type germanium. Appl. Phys. Lett. *100*.

61. Yu, H., Schaekers, M., Schram, T., Aderhold, W., Mayur, A.J., Mitard, J., Witters, L., Barla, K., Collaert, N., Horiguchi, N., et al. (2016). Low-resistance titanium contacts and thermally unstable nickel germanide contacts on p-type germanium. IEEE Electron Device Lett. *37*, 482–485.

62. Nishimura, T., Kita, K., and Toriumi, A. (2007). Evidence for strong Fermi-level pinning due to metal-induced gap states at metal/germanium interface. Appl. Phys. Lett. *91*, 12–15.

63. Kang, D., Young, J.L., Lim, H., Klein, W.E., Chen, H., Xi, Y., Gai, B., Deutsch, T.G., and Yoon, J. (2017). Printed assemblies of GaAs photoelectrodes with decoupled optical and reactive interfaces for unassisted solar water splitting. Nat. Energy *2*, 1–9.

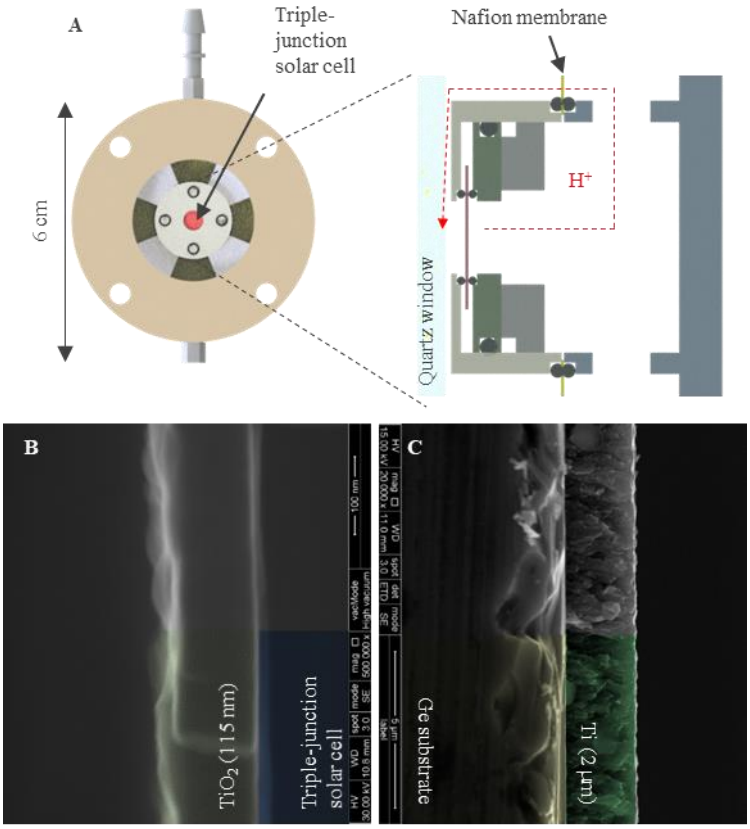

Figure 1 Experimental setup for testing wireless PEC (A) Compression cell used for testing wireless devices. The red object in the middle represents the PEC device. Protons travel from the backside to the front side of the device around the solar cell (along the red dotted line). The design of the compression cell can be further improved by shortening the proton transfer distance. (B) TiO_2 protection layer for the optical front side, and (C) metallic Ti protection layer for the Ge backside of the triple-junction solar cell.

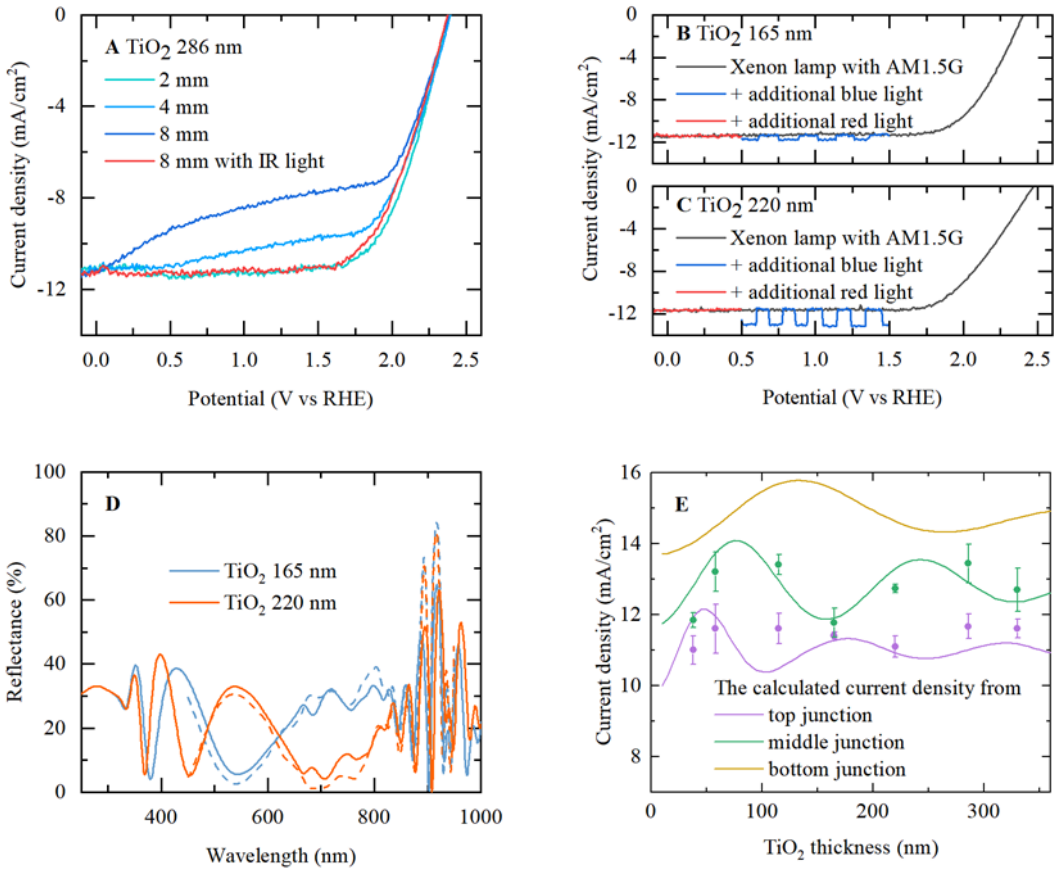

Figure 2 The thickness of TiO2 protection layer and water layer affect the activity of the PEC devices (A) The photocurrent density measured with 2, 4 or 8 mm of water layer in front of the PEC device. The loss by the infrared absorption is recovered by supplying additional infrared light. Photocurrent density from the triple-junction PEC devices with (B) 165 and (C) 220 nm of TiO_2 thickness (black lines). A chopped source of extra photons for the top junction (blue) and the middle junction (red) are supplied to determine the current limiting junction. See also Figure S2. (D) The wavelength dependent reflection of the PEC device for two selected TiO_2 thicknesses. The solid lines are calculated and the dashed lines are measured reflectance. See also Figure S4. (E) Measured current density without (purple data points) and with (green data points) the blue light is compared to the calculated current density from each junction. The error bars represents the standard deviation from measurements on three devices with the same

TiO_2 thickness.

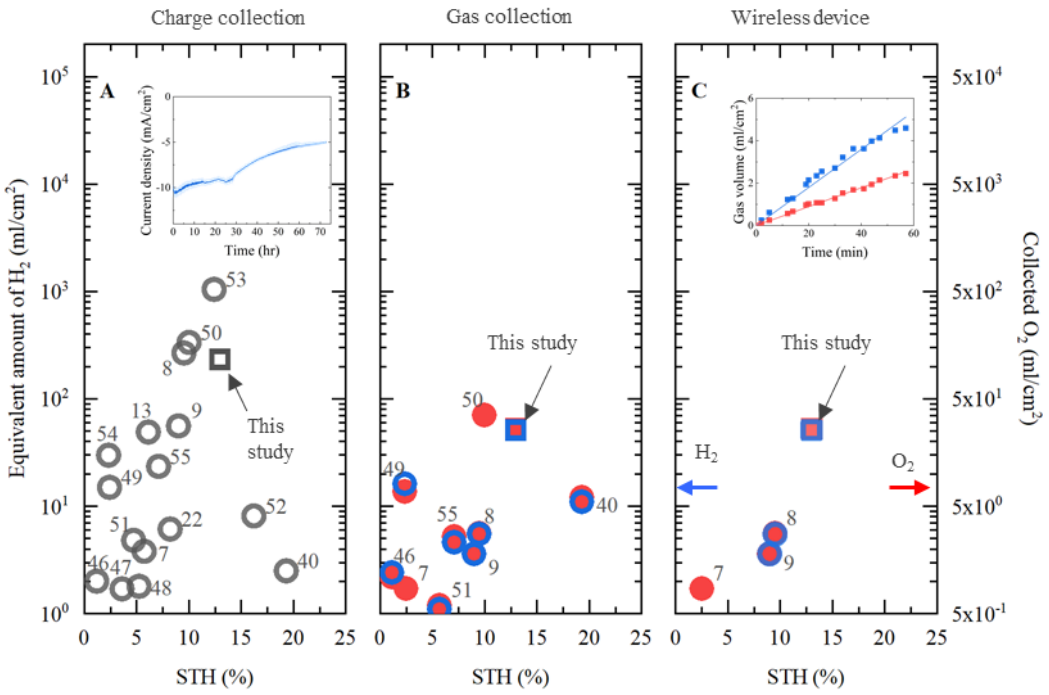

Figure 3 The stability of the PEC devices is tested by capturing gaseous products over its lifetime Total amount of H_2 produced over the lifetime of PEC devices from selected papers (circle) and this study (rectangle) are charted depending on the measurement methods. (A) H_2-lifetime production "measured" by charge passed in the unit of the equivalent amount of H_2. The wired device from this study reached 231 ml/cm^2 and the inset figure shows the chronoamperometry data from the device. (B) H_2-lifetime production measured by gas collection. Blue and red data points represent the amount of collected H_2 (left y-axis) and O_2 (right y-axis). Note that the H_2 axis is scaled by a factor of 1/2 compared to the O_2 axis to make H_2 and O_2 datapoints in the stoichiometric ratio (2:1) overlap each other. (C) H_2-lifetime measured from wireless devices only. The inset figure shows gas collection during the first hour of this study used to calculate STH efficiency. See also Table S1.

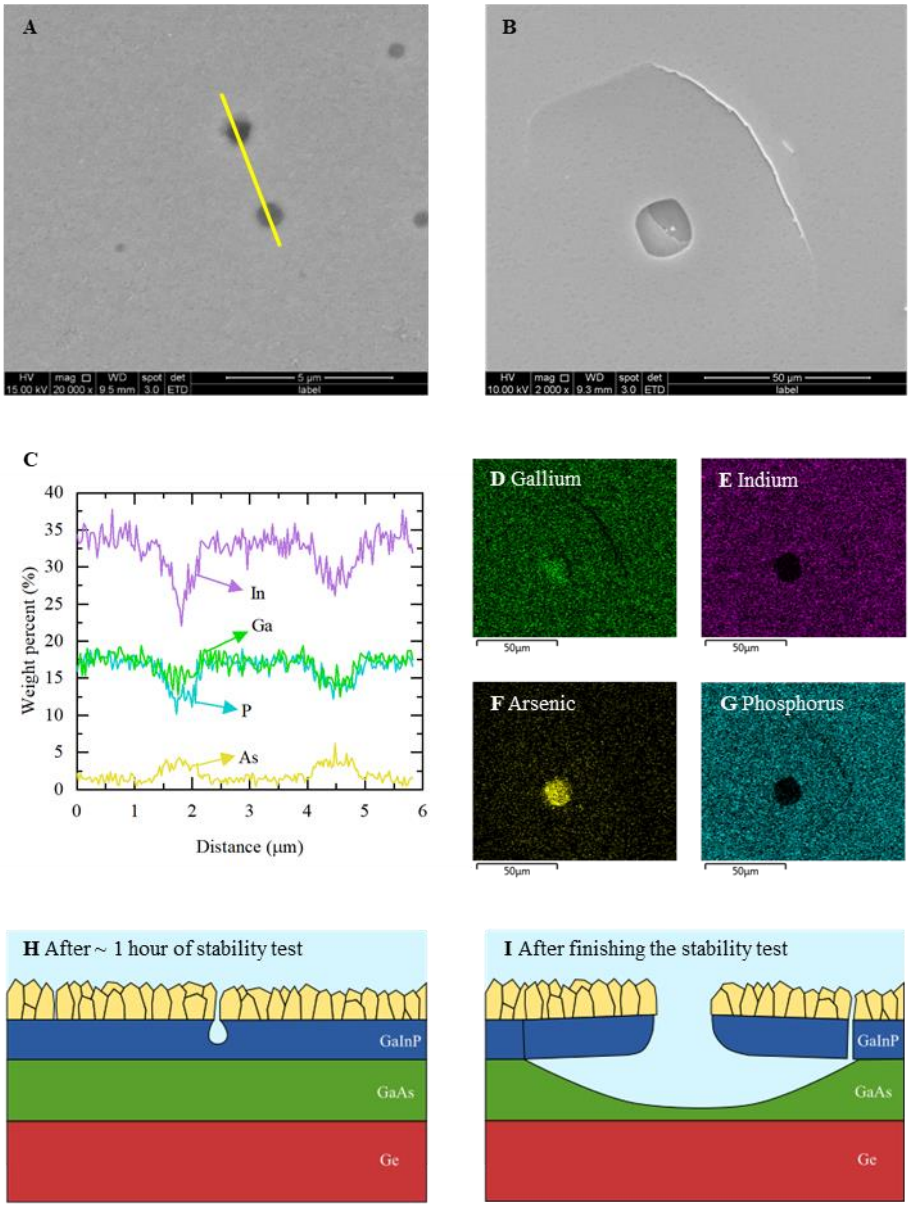

Figure 4 The surface morphology of the PEC devices is observed after the reaction using SEM and EDS In the initial stage of corrosion (A,C), dark spots appear in the SEM image (Scale bar: 5 μm). Those spots have a lower composition of top junction materials (In and P) and higher composition of middle junction materials (As). In the later stage of corrosion (B, D, E, F and G), the cracks surrounding the corrosion spot appears as shown in the SEM image (Scale bar: 50 μm). (H) and (I) show schematic diagrams of the corrosion process. Because of a pin-hole in the protection layer, GaInP top junction begins to corrodes in the initial stage.

When the corrosion in the top junction reaches GaAs middle junction, the corrosion grows rapidly along the middle junction and it eventually leads to the delamination of the top junction.

Table S1 Table of H_2-lifetime from unassisted water-splitting devices in Figure 3 The data points shown in Figure 3 are tabulated.

Supplemental video

Gas collection from a wireless PEC device Left panel: H_2 bubble produced over the front side of the PEC device. Right panel: H_2 and O_2 collection by eudiometer.

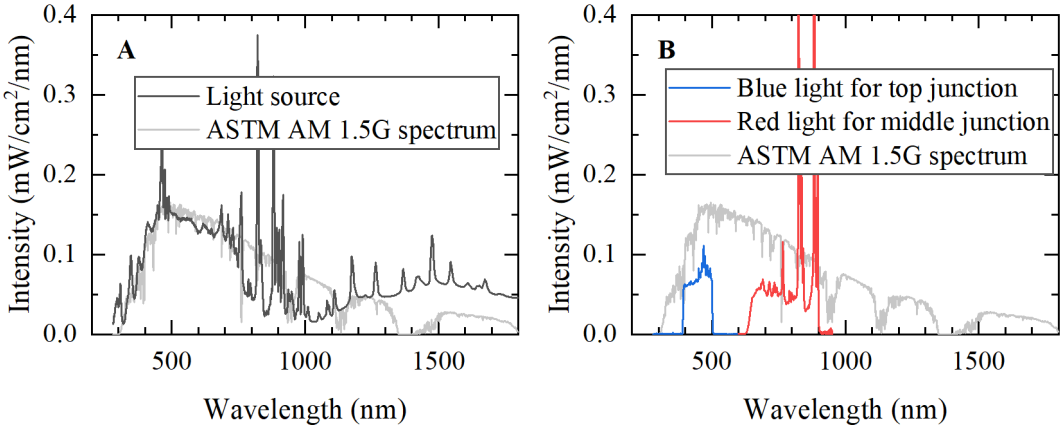

Figure S1. The intensity of the light sources used in this study. (A) The intensity of the light source provided by the supplier and AM 1.5G filter transmittance (black) and the standard AM 1.5G spectrum (grey). (B) The additional blue light (blue) and the additional red light (red) used for exciting top and middle junction, respectively.

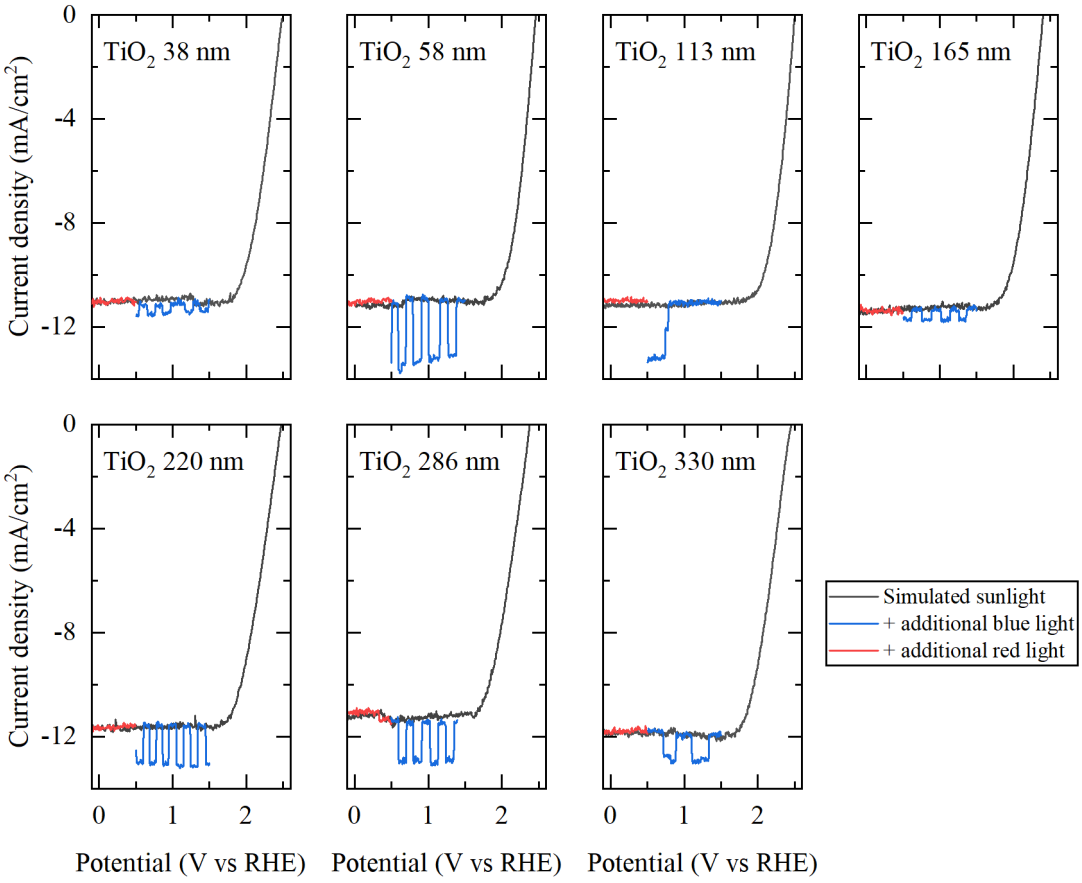

Figure S2 Cyclic voltammetry of PEC devices with various TiO_2 thicknesses, Related to Figure 2B and C. The current density of PEC devices with seven different TiO_2 thicknesses are measured without any additional light sources (black), with the additional blue light (blue) and the additional red light (red), respectively.

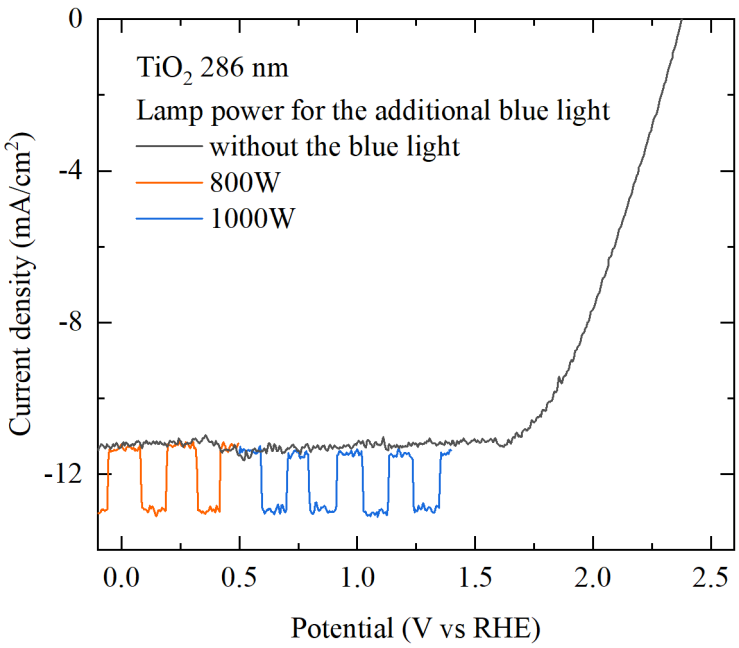

Figure S3 Cyclic voltammetry of a PEC device with two different blue light intensities. The current density without the additional blue light (black) shows the current density from the top junction. Small changes in the current density (at ~ 0.3 and 1.6 V vs RHE) are from bubbles on the device surface. The intensity of the blue light is changed by controlling the light source power input to be 800 W (orange) and 1000 W (blue). However, the current density under the additional blue light is not changed. It shows that, in this range of the blue light intensity, the top junction is fully saturated, and another junction in the triple-junction solar cell is limiting the current density. If the blue light intensity were too weak, the top junction is not fully saturated, and the current density would show dependence on the blue light intensity. If the blue light intensity were too strong, it would provoke a significant photoluminescence coupling effect, which would also be showing the intensity dependence. Either too weak or too strong, the current density would depend on the blue light intensity and not represent the current density from another junction.

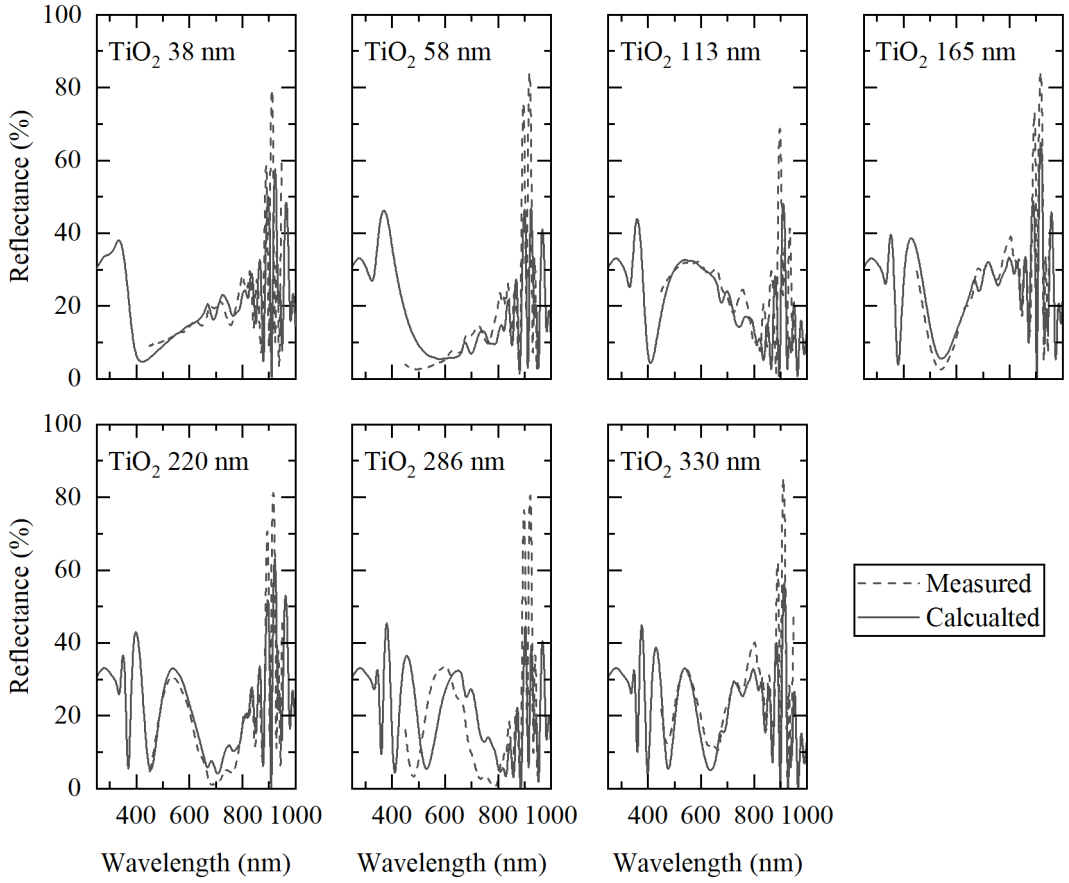

Figure S4 Reflectance of PEC devices with various TiO_2 thicknesses, Related to Figure 2D. The reflectance of PEC devices with seven different TiO_2 thicknesses are calculated (solid) and measured (dashed).

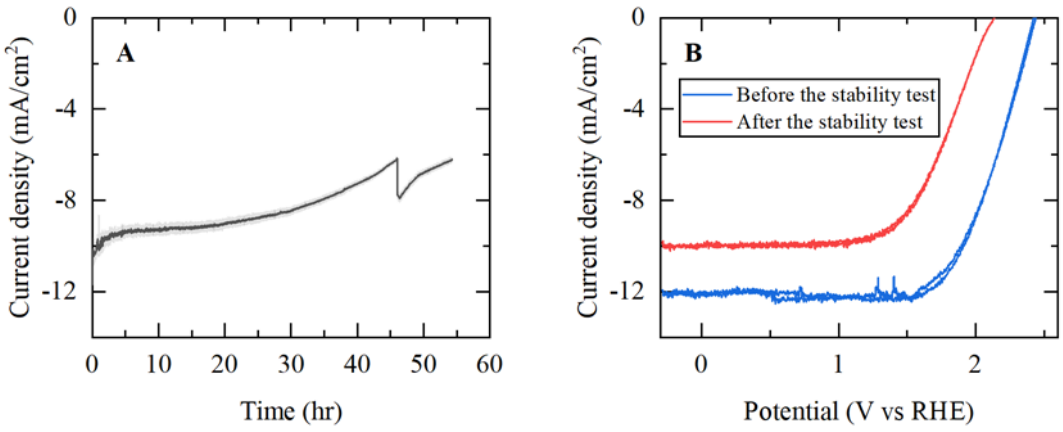

Figure S5 Photovoltage and current density before and after the stability test. (A) Stability test by charge collection. The failure at 40 ~ 45 hr is from the evaporation and refill of the electrolyte. (B) J-V measurement before and after the chronoamperometry at 0 V vs IrO_2 for ~ 55 hours.

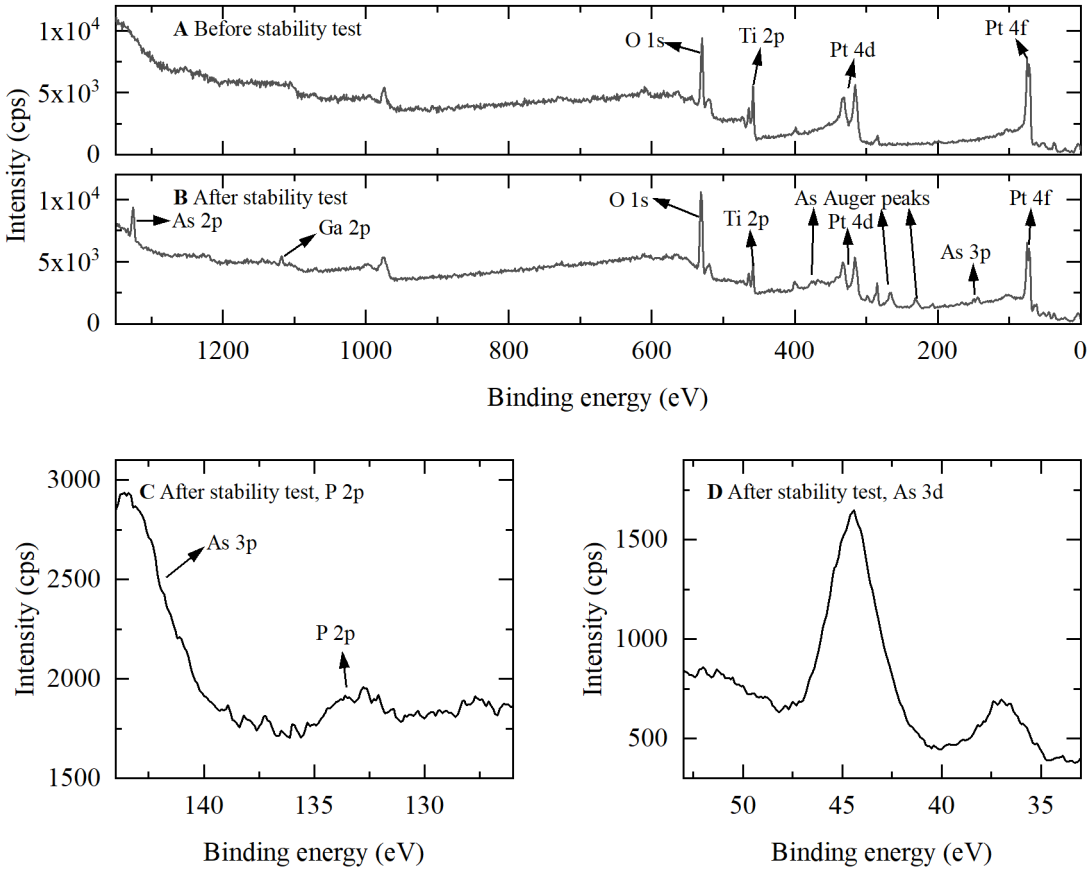

Figure S6 X-ray photoelectron spectroscopy before and after the stability test. Survey scan (A) before and (B) after the stability test shows a significant amount of arsenic from the dissolved GaAs middle junction is redeposited over the stability test. The difference between XPS intensities from phosphorus (C) and arsenic (D) indicates that the GaInP top junction and GaAs middle junction have significantly different etch rates in 1 M $HClO_4$.

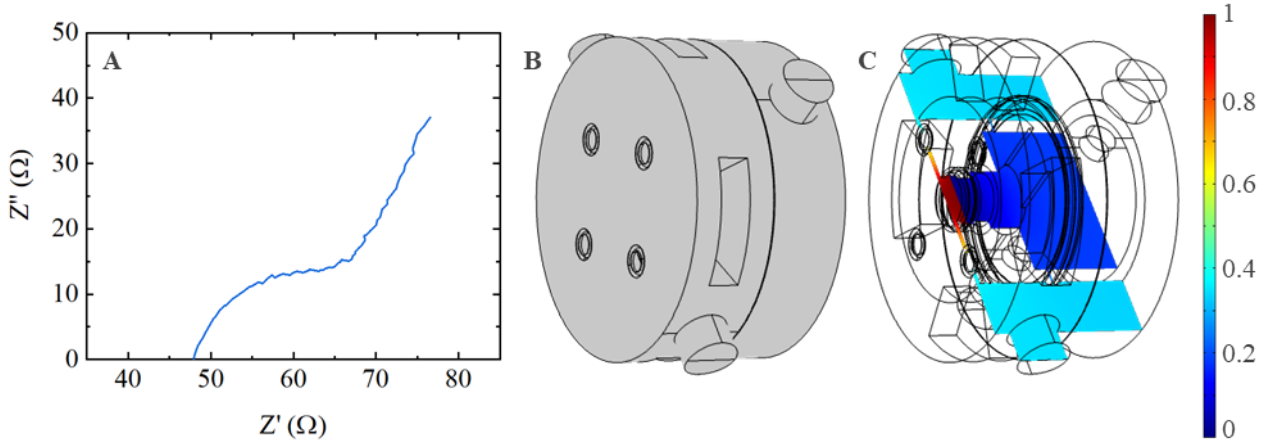

Figure S7 Ohmic resistance in the compression cell. (A) The ohmic loss inside of the compression cell is measured by electrochemical impedance spectroscopy (EIS). Instead of the solar cell wafer, Ti foil is inserted with a Cu wire connected on its backside. The position of the working electrode is defined by blocking the backside of Ti foil with an acid-stable polymer to make only the front side of the front side contact the electrolyte, and the Cu wire is completely covered with a PFA tube. The counter electrode is a Pt wire wrapped in a PEEK tube, but the end of the wire is exposed to the electrolyte near the backside of Ti foil. In this way, the proton is transferred along the path that it should follow in the PEC experiment. The measurement shows that the ohmic resistance in the cell filled with 1 M $HClO_4$ is 48 Ω, and it will result in 90 ~ 100 mV of ohmic voltage drop. A compression cell with an improved design should be able to avoid the ohmic voltage drop. The measurement is further supported by a finite element method (FEM) simulation using commercial software (COMSOL Multiphysics®). (B) The electrostatic equation is solved with the volume of electrolyte inside the cell. The electrical conductivity of the electrolyte and Nafion membrane are chosen to be 42 S/m/M and 10 S/m based on the references[1,2]. (C) The simulated ohmic resistance in the cell is 37 Ω, which is similar to the measured value, and a significant portion of the ohmic resistance comes from the shallow aqueous layer in front of the PEC device.

Supplemental Note S1. Calculation of the reflectance and the current density from each junction

The calculation of the reflectance is carried out using the transfer matrix method.[3] The structure of the PEC device is modeled as a stack of GaInP, GaAs and Ge films. It is assumed that the Ge bottom junction is infinitely long that there is no reflection after the boundary between the middle and bottom junction. The refractive indexes of air and water are chosen to be 1 and 1.33, and the other optical properties of TiO_2, GaInP, GaAs are also adopted from references[4–6].

The expected current density from each junction is calculated using the spectrum provided by the supplier multiplied by the transmittance of AM 1.5G filter (*I*), reflectance (*R*), the internal quantum efficiency (IQE) and absorption by water (a) over the water layer thickness (t) as below.

$$J_i = \int e^{-at} \times I(\lambda) \times \big(1 - R(\lambda)\big) \times \mathrm{IQE}_i(\lambda)\ d\lambda$$

Here, subscript i indicates each junction. The thickness of the water layer is assumed to be 2 mm. The absorption coefficient *a* is from the reference.[7] The IQE is derived from 1) external quantum efficiency (EQE) measurement and 2) calculated reflectance from a triple junction device with indium tin oxide (ITO) as a front contact. EQE is measured following the procedure introduced by Meusel et al..[8] The refractive index of the ITO film used for the reflectance calculation is measured by ellipsometry.

Year	Initial STH (%)	Charge collection (ml/cm^2)	Hydrogen collection (ml/cm^2)	Oxygen collection (ml/cm^2)	Operation time (hr)	Author	Reference
1987	8.2	6.1			1.3	Kainthla	22
1998	12.4	1044.6			20	Khaselev	53[a]
2011	4.7	4.8			2	Reece	7
2011	2.5			0.85	2	Reece	7
2012	1.17	2	2.4	1.1	8	Brillet	46
2013	3.6	1.7			1	Abdi	47
2014	5.2	1.8			1	Han	48
2015	9.5	267.4	5.5	2.8	80	Verlage	8
2015	5.7	3.8	1.1	0.6	2	Shi	51
2015	2.4	15	16.2	6.8	8	Gurudayal	49
2015	2.3	29.9			52	Kelly	54
2016	10	334.3		35	100	Sun	50
2016	7.1	23.4	4.6	2.6	10	Shi	55
2017	16.2	8.1			13	Young	52
2018	19.3	2.5	11	6	0.5	Cheng	40
2019	9	56	3.6	1.8	157	Varadhan	9
2020	6.1	49			11.8	Ben-Naim	13[b]

[a] 11 sun illumination [b] 2.6 sun illumination

Table S1 Table of H_2-lifetime from unassisted water-splitting devices in Figure 3 The data points shown in Figure 3 are tabulated.

Supplemental References

1. Brickwedde, L.H. (1949). Properties of aqueous solutions of perchloric acid. J. Res. Natl. Bur. Stand. (1934). *42*, 309.

2. Napoli, L., Franco, J., Fasoli, H., and Sanguinetti, A. (2014). Conductivity of Nafion® 117 membrane used in polymer electrolyte fuel cells. Int. J. Hydrogen Energy *39*, 8656–8660.

3. Copson, E.T., Born, M., and Wolf, E. (1961). Principles of Optics 7 Ed. (Cambridge University Press).

4. Pulker, H.K., Paesold, G., and Ritter, E. (1976). Refractive indices of TiO_2 films produced by reactive evaporation of various titanium–oxygen phases. Appl. Opt. *15*, 2986.

5. Rakić, A.D., and Majewski, M.L. (1996). Modeling the optical dielectric function of GaAs and AlAs: Extension of Adachi's model. J. Appl. Phys. *80*, 5909–5914.

6. Schubert, M., Gottschalch, V., Herzinger, C.M., Yao, H., G., S.P., and Woolam, J.A. (1995). Optical constants of $Ga_xIn_{1-x}P$ lattice matched to GaAs. J. Appl. Phys. *77*, 3416.

7. Hale, G.M., and Querry, M.R. (1973). Optical Constants of Water in the 200 nm to 200 μm Wavelength Region. Appl. Opt. *12*, 555.

8. Meusel, M., Baur, C., Létay, G., Bett, A.W., Warta, W., and Fernandez, E. (2003). Spectral response measurements of monolithic GaInP/Ga(In)As/Ge triple-junction solar cells: Measurement artifacts and their explanation. Prog. Photovoltaics Res. Appl. *11*, 499–514.

Technical
University of
Denmark

Fysikvej, Building 311
2800 Kgs. Lyngby
Tlf. 4525 1700

www.fysik.dtu.dk